EXPERIMENTAL AND THEORETICAL CONSIDERATIONS OF ATTENUATION AND VELOCITY INTERACTIONS WITH PHYSICAL PARAMETERS IN SANDS

Dissertation
zur Erlangung des Doktorgrades
der Mathematisch-Naturwissenschaftlichen Fakultät
der Christian-Albrechts-Universität
zu Kiel
Vorgelegt von
Manika Prasad
Kiel
1988

Referent:.....Prof. R. Meissner
Koreferent:.....Prof. J. Zschau
Tag der mündlichen Prüfung:..9.Nov., 1988
Zum Druck genehmigt:.....9.Nov., 1988

.....
Dekan

1. Abstract

Sand and silt samples are tested in the laboratory with a view of studying and correlating their geologic and seismic properties. The P- and S-wave velocities and attenuations, measured at a frequency around 100 kHz in a Pulse Transmission experiment,are compared with the grain sizes and shapes, porosities, permeabilities, and rigidity coefficients of these samples. Additionally, the velocities and attenuations are modelled to understand the effects of physical properties on the seismic characteristics.

These physical properties are seen to be closely related to the seismic signals and could be employed to predict the type of response they would give to seismic excitation or vice versa. The following significant features are seen:

- Rigidity coefficient and P-wave velocity correlate at low pressures. This correlation diminishes with increasing pressures.
- Coarseness of grains enhances the velocity and attenuation of P-waves and the attenuation of S-waves, but the S-wave velocity is unaffected by grain size.
- Angularity of grains causes a decrease in velocity, attenuation and rigidity coefficient.
- Dry grains show high shear losses, whereas saturated grains have predominant bulk losses of seismic energy.

The results are then modelled to gain insight into the mechanisms deforming a seismic pulse on its passage through the sediment. Both, dry and saturated cases, are examined.

The dry samples are approximated by a contact radius model which relates the elastic moduli to a changing contact radius between adjacent spheres. The velocities calculated with this model match the measured values. The losses observed in dry sediments are due to friction at the contact

radii betwen two adjacent grains. Calculations made for different grain sizes show that even at strains about 10^{-7} such effects are to be expected in unconsolidated sediments, posing a great restraint on seismic sources and modelling of seismic data.

Different loss mechanisms are seen to be active in the saturated samples. The losses described by the Biot theory, augmented with frictional losses in the solid frame, describe the attenuation phenomenologically but are less than those observed Also the velocoities calculated here are less than those observed. It is suggested, that these higher velocities and losses observed are caused by pore pressure buildups in the pore fluid. A rough and a priori approximation shows that these differences in the measured and calculated velocities could be accounted for by this effect. If this were true, the modelling of seismic data would gain additional aspects of assessing pore pressures buildups in situ terrains.
An estimate of the difference between velocities measured at 100 kHz and those calculated with the Biot theory in the low frequency range shows, that the high frequency velocities are about 5 to 10% higher than the low frequency velocities. If the Biot theory is valid for the seismic frequencies too, this effect must be considered in comparing velocities of the different frequencies.

CONTENTS

2. Introduction

Laboratory measurements may not have the glamour of in situ investigations, but they deliver important information about interactions of different parameters, which can be singled out for observation. A modelling of this data with the possible mechanisms gives additional understanding of mechanisms of seismic wave propagation through sediments. Armed with this information, an interpretation of seismic field data becomes more reliable.

The present work aims at understanding and correlating physical parameters used to identify horizons and their seismic signature for detection. The physical parameters studied here are grain size, shape, roundness, rigidity coefficient, shear strength and permeability. The two seismic quantities velocity and specific dissipation, are more problematic to determine.

Velocity is a quite well defined parameter. It can be more or less exactly determined, and the ranges of velocities of different sediments and rocks are also known. The correlation between the specific dissipation and physical properties is more limited. This is mainly due to lack of understanding of characteristic attenuation values for different sediment types. Additionally, a number of definitions assigned to the specific dissipation lead to a myriad of values for one rock type (for example, in igneous rocks Q = 10...1000).

The main definitions of 'Q' are mentioned here for a better understanding (Zschau, 1985). The fundamental definition given by Knopoff and McDonald (1958) defines Q as the ratio of maximum strain energy stored, E_0, to that lost in one cycle, ΔE_0, during a periodic strain.

$$Q = 2\pi E_0 / \Delta E_0 \qquad (2.1)$$

However, for all practical purposes, E_0 being difficult to determine, the definition suggested by Dain (1962) is used, using the average strain energy stored, E_{av}:

$$Q_\lambda = 4\pi E_{av}/\Delta E_0 \qquad (2.2)$$

This relationship is also valid only for periodic loads. Q_λ can be related to the complex modulus of elasticity, $M=M_r+iM_i$ (O'Connell and Budiansky, 1978) and the phase shift φ between stress and strain by:

$$Q_\lambda = M_r/M_i = 1/\tan\varphi \qquad (2.3)$$

If dissipation is very small, $Q_\lambda = Q$.

Since the above definitions are valid only for periodic loads, the following relationship by Futterman (1962) for waves encountered in seismics is used:

$$Q_{seis} = 2\pi e_0/\Delta e_0 \quad , \qquad (2.4)$$

where e_0 = max. amplitude of kinetic energy density

Δe_0 = decline of e_0 along a wavelength.

Again for small dissipation, $Q_{seis} \rightarrow Q_\lambda$, but for large dissipation $Q_{seis} \rightarrow 2\pi$.

The definition of Q in eq. 2.4 for transient signals will be used in this thesis, where the subscript 'seis' is omitted.

There are various methods to study attenuation in the laboratory. Resonance methods observe the resonance frequency and the decay in amplitude displacements (Shumway, 1956, 1960 a, b; Winkler and Nur, 1979). Quasi-static methods determine directly the phase lag between an applied strain and the response (Spencer, 1981; Jedicke, 1984). Pulse Transmission experiments, used here, study the deformation of a pulse in transmission through a sediment (Toksöz et al, 1979; Muckelmann, 1985).

Some major results, by far not all, are mentioned here:

1) Attenuation decreases and velocity increases with pressure.
2) At strains below 10^{-6} frictional losses in rocks can be neglected (Winkler et al, 1979; Stewart et al, 1983; Mavko, 1979; Winkler and Nur, 1982). The pesent research shows frictional losses in unconsolidated sediments at

strains $\approx 10^{-7}$.

3) Volatiles play a very important role in degradation of a seismic wave. With only 1...2% volatiles, P-wave attenuation increases and velocity decreases significantly. S-waves remain unaffected (Murphy, 1982, 1984b; Muckelmann, 1985).
4) Small amounts of clay in sands let velocities decrease (Han et al, 1986).
5) Frame modulus is decreased due to adsorption of fluids on grain contacts (Murphy et al, 1984a,b,c and 1986).
6) Attenuation increases with decreasing grain size (Hamilton, 1972).
7) A formal confirmation of the Biot theory is lacking although Hovem and Ingram (1979) and McCann and McCann (1985) maintain to see a confirmation of the low frequency Biot theory on glass beads.
8) Attewell and Ramana (1966), from a comparison of values reported by different authors, conclude, that the specific attenuation factor Q^{-1} or the internal friction is independent of frequency, a mean value being $4.7*10^{-3}$ over the frequency range of $10^{-3} < f < 10^{7}$.
9) The experiments of Burkhardt et al (1986) indicate that at different frequencies, different absorption mechanisms prevail.

The modelling of seismic quantities go in two different ways. One method models the deformation of the frame and determines effective frame moduli. Starting with a Hertzian contact between two spheres, Mindlin (1949) studied the compliance of elastic bodies in contact under a small tangential force and torsional couple. Mindlin and Deresiewicz (1953) introduced energy dissipation due to slip under different histories of loading along with varying normal forces, monotonously increasing, decreasing and oscillating. A more complicated random packing of spheres of different radii was modelled by Brandt (1955) to obtain the effective shear modulus, and Deresiewicz (1958) and Duffy and

Mindlin (1957) modelled stress strain relations for a face-centered cubic arrangement of spheres in contact. The energy lost in contact friction (Goodman and Brown, 1962) and the effect of surface energy on grain contacts for different fluids (Johnson et al, 1971) have also been considered. Walton (1977) derived effective velocity in fluid saturated rock, only for logitudinal waves and Digby (1981) modelled a random packing of spheres cemented together to obtain bulk and shear moduli.

The second school of modelling assumes these frame moduli and considers interaction between two phases of a porous elastic medium. The basic ideas behind it are delivered by Biot (1956 a, b, 1962, 1973) and Gassmann (1951). The equations of Biot were reformulated by Stoll and Bryan (1970), Stoll (1974, 1979), and Geertsma and Smit (1961) found suitable solutions for wave velocity and attenuation from them. The effects of pore space and its shape on permeability and bulk modulus have been modelled by Seeburger and Nur (1984). O'Connell and Budiansky (1974) reasoned that the presence of cracks will decrease seismic wave velocities, and in 1977 they incorporated effects of fluid saturation in these cracks. The phenomenon of partial saturation in sands is explained by Mavko and Nur (1979), who attribute these strong attenuation effects observed in P-waves to local flow in the pores due to the difference in compressibility of gas and pore fluid. On the other hand, Muckelmann (1985) accounted these attenuation effects to the pulsation of gas bubbles excited by the seismic waves; a mechanism which is operative at high frequencies ($f \geq 1kHz$). The location of the attenuation peak is sensitive to the bubble size; smaller bubbles cause a shift of the peak to higher frequencies.

The present approach is taken to correlate the seismic and geologic parameters and to understand the mechanisms of seismic wave attenuation in sands. It should be possible to relate the attenuation and velocity of P- and S-waves to porosity, permeability, grain size, pore filling and

compaction. A knowledge about these interactions would make seismic interpretation more reliable. An attempt is made in this thesis in examining various types of sands with respect to their seismic and geologic properties. The different experiments are described in Sec. 3. In Sec. 4 the results of the seismic experiments are presented along with their correlation with the geologic parameters. In Sec. 5 dry and saturated sands are modelled with a view of understanding the attenuation mechanisms effective therein, and also to find physical properties from a seismic measurement. Sec. 6 summarizes the results of the experiments and those of the different modelling trials.

3. Description of the Experiment

The main aim of this work was to study the effects of physical parameters on seismic properties. The geologic and seismic experiments are described here; the results of the seismic experiments and their interaction with geological properties are discussed in Sec. 4.

The coarser grained samples were sieved from sands supplied by the V. Busch Quarzwerke KG in Schnaittenbach, Bayern, FRG, to obtain very well sorted, almost 'one grained' samples with uniformity coefficients less two. The pulse transmission (P.T.) experiments were carried out on a selection of these samples and on a finer grained quartz powder from the Quarzwerke GmbH, Frechen, FRG.

3.1 Physical Properties

31 samples covering a wide range of grain sizes were examined with respect to grain size, grain shape, porosity, density, permeability, rigidity coefficient and cohesive strength.

Grain Size Distribution

The grain size distribution was determined on the basis of sieving and sedimentation for coarser grains and with an X-Ray sedigraph for finer grains (< 63 μm). The steep grain sizes of all samples except the finer grained H200, F100 etc, Fig. 3.1, indicate them to be very uniform. Comparing the uniformity coefficient C of the samples, generally below two, as given in Table 3.2, with the values that 'C' can take for a wide range of samples in Table 3.1, shows that all samples can be termed as uniform, since smaller values of 'C' imply better sorting of the sediment.

$C = D_{60}/D_{10}$

D_{10}: grain size corresponding to 10% on grain size curve

D_{60}: grain size corresponding to 60% on grain size curve

C	sediment sorting
< 3	uniform
3...15	non uniform
> 15	well graded

Table 3.1: Uniformity coefficient and sediment sorting from Prinz (1982). Smaller values of C imply better sorting.

Sample	Shape	Uniformity Coefficient	Permeability (Darcy)
P1	round	1.3	58.79
P2	round	1.1	43.26
P3	round	1.2	19.98
P4	round	1.4	21.01
P5	round	1.2	13.56
P6	round	1.4	8.36
QS2	round	1.3	3.07
PQS1	round	1.3	1.87
P8	round	1.2	1.20
A1	angular	1.2	21.53
A2	angular	1.3	10.56
A3	angular	1.3	6.36
A4	angular	1.9	2.42
A5	angular	2.4	0.24
S1	powdered	1.7	0.55
H200	powdered	2.4	0.12
F600	powdered	2.8	0.01

Table 3.2: Grain size characteristics and permeability values of the rounded, angular and powdered samples

Grain Shape

This was determined under the microscope for different samples. In Fig. 3.2, photographs of the grains of three representative samples are shown.

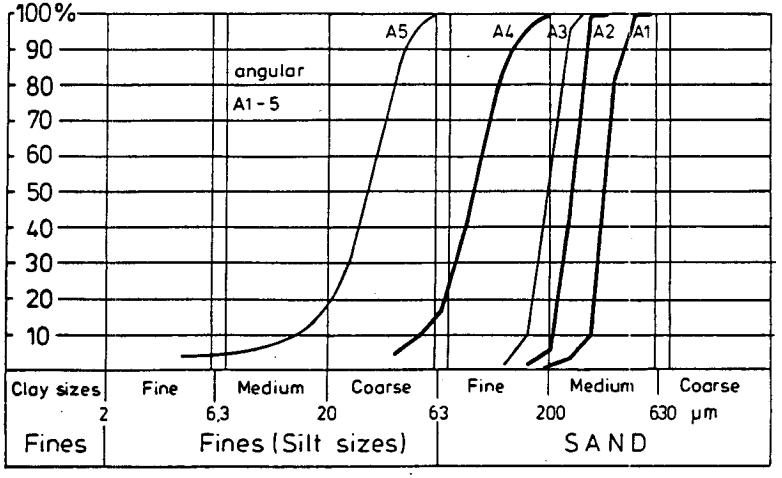

Sample	A1	A2	A3	A4	A5	S1	H200	F600
D = 10 µm	310	205	160	52	14	27	9	1.6
D = 50 µm	360	255	205	91	30	41	20	3.7
C=D60/D10	1.2	1.3	1.3	1.88	2.36	1.66	2.45	2.75

Sample	P1	P2	P3	P4	P5	P6	QS2	PQS1	P8
D = 10 µm	530	500	380	270	255	160	120	89	74
D = 50 µm	650	550	460	360	300	220	145	110	90
C=D60/D10	1.3	1.1	1.2	1.4	1.2	1.4	1.25	1.3	1.2

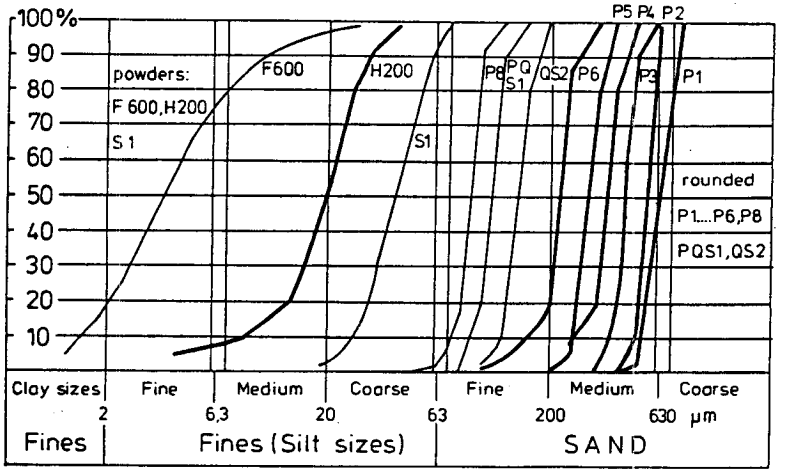

Fig. 3.1: Grain size analysis of the angular (top), rounded and powdered (bottom) samples. Bolded curves represent samples measured in the seismic experiment. The Uniformity coefficient, its median and effective grain size are given in the adjoining table.

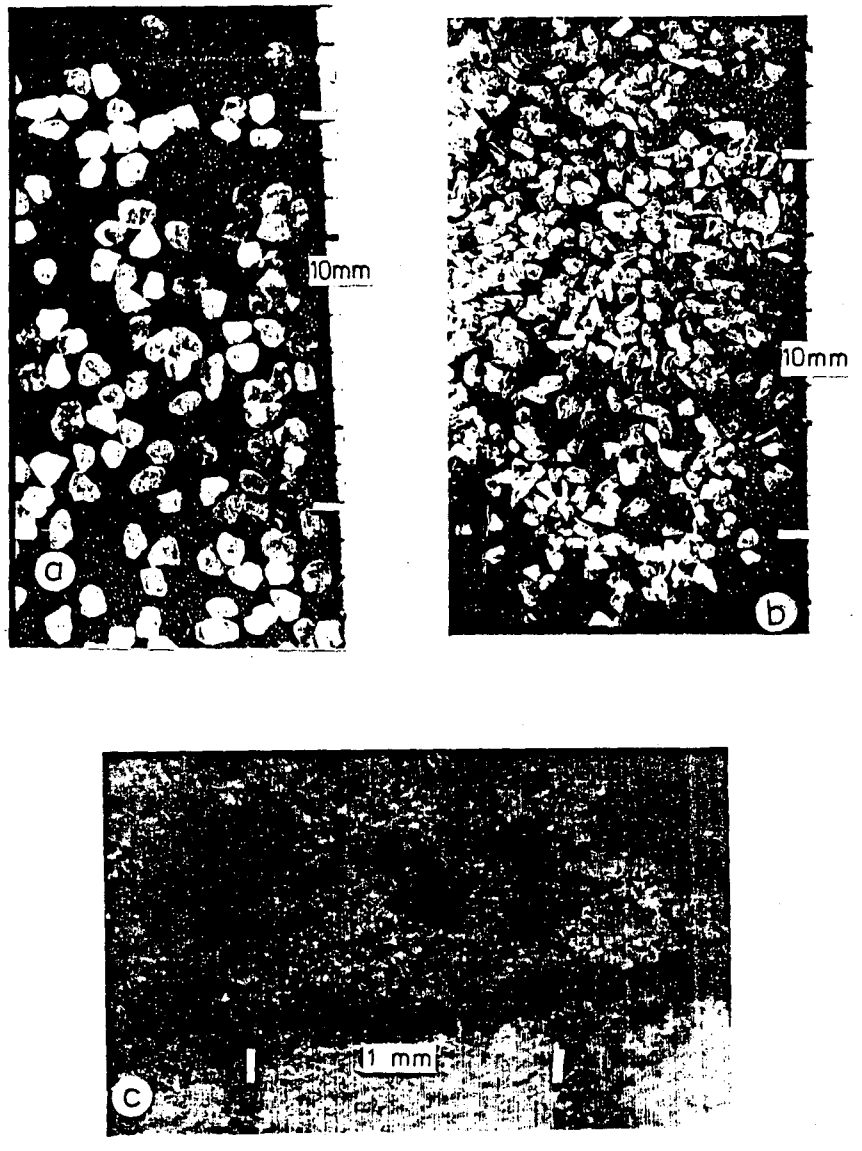

Fig. 3.2: Grain shapes of samples used; a: Sample P1, rounded, b: sample A1, angular, c: sample H200, powder. Note different scale for sample H200.

Density and Porosity

Density and porosity were calculated from the sample length during the P.T. experiment, and odeometer tests. Porosity values from both methods are plotted in Fig. 3.3 versus differential pressure. The lower porosities in the P.T. experiment are due to the weight of the pressure enclave cover (≈ 200 kg) resting on the sample during assemblage of the apparatus. The porosity values, $\Phi(Pd)$, being calculated as changes in the porosity at 0-pressure, $\Phi(0)$, the $\Phi(Pd)$ shall vary, depending on the value of $\Phi(0)$ taken. $\Phi(0)$ for the experiment was calculated from the sample length at 0-pressure after mounting the 200 kg cover.

Permeability

Permeability has a very close relationship with porosity. If the voids in a soil are interconnected, they will form small irregular conduits through which, in the presence of a pressure gradient, a pore fluid can flow. Of various methods of determining the permeability coefficient k_f in the laboratory, "the method of Beyer in evaluating the grain size frequency distribution yielded the narrowest range of dispersion and the best degree of approximation to the mean value of all the methods with relatively little efforts" (Pekdeker and Schulz, 1975). On this basis and on a personal communication with Prof. Schulz (1985), k_f of the samples was determined by the Beyer-method. Using an empirical equation, which takes into account the uniformity coefficient C from the grain size analysis :

$k_f = C * (D_{10})^2$, where (3.1)

D_{10} in mm is the grain size of fraction in which 10% by weight of the fraction is reached, and k_f is in m/s.

The permeability coefficients thus determined are given in Table 3.2, and compared with the k_f values occurring in nature in Fig. 3.4.

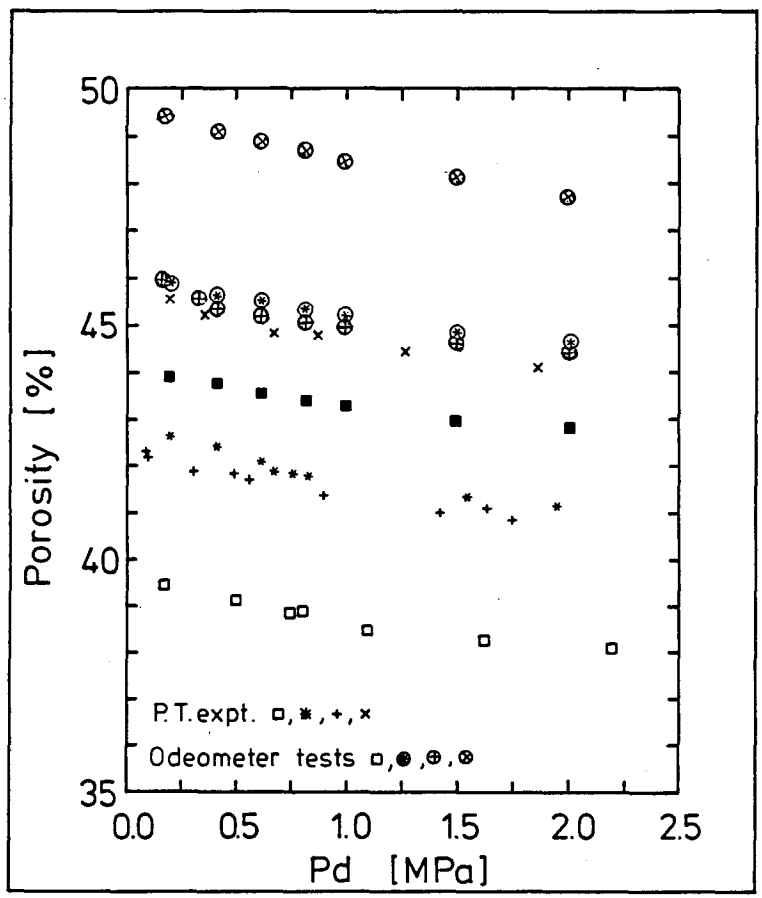

Fig. 3.3: Comparison of porosity calculated from Odeometer tests and P.T. experiment. Porosity values from Odeometer tests are higher by about 5%.

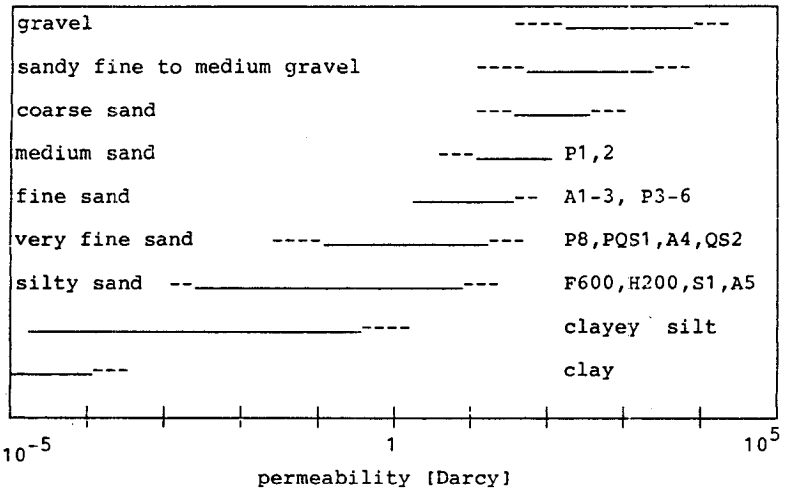

Fig. 3.4: Permeability values (__) of different samples, (--) gives also possible ranges, modified from Bentz and Martini (1969).

Another method of determining the permeability is by directly measuring the flow of a pore fluid in the sample. The filter velocity and direction of the fluid, depending on one hand on the physical characteristics, such as density and viscosity of the flowing medium, and on the other hand on the size and shape of the conduits through which it flows, is given by the Darcy-Law :

$$V_{flow} = q_v/A = k_f dP/\eta/X \quad \text{, where} \qquad (3.2)$$

V_{flow} = flow velocity of the pore fluid
q_v = flow volume of the pore fluid
η = viscosity of the pore fluid
X = length of the sample
A = area of the sample
dP = pressure gradient of the pore fluid
k_f = coefficient of permeability

k_f expresses the ease with which a pore fluid passes through a soil. Whereas porosity takes into account only the sum of all pore voids present in the system, permeability specifies their geometric structures too and is more sensitive to changes in varying sediments: higher permeabilities must be accompanied by high porosities, whereas sediments with high porosities need not necessarily have high permeabilities.

The Darcy-Law holds good only for a laminar flow. For wide fissures or clean coarse gravel with void diameters exceeding 10 mm, and for pressure gradients exceeding 5, the expression does not apply (Sowers, 1979). Alternatively, laminar and turbulent flow can be differentiated by considering the inertial forces and the Reynolds number.

The forces acting in the pores due to motion in the pore fluid can be divided into a driving force dF_p and a resisting force dF_r (Engelhardt, 1960). The vector sum of both is equal to the inertial force of the volume.

$$a*dm = dF_p + dF_r \qquad (3.3)$$

These inertial forces, a*dm, are negligible as compared to the forces of inner friction, if the flow in the medium is laminar:

$$- dF_p = dF_r \qquad (3.4)$$

Thus the Darcy Law is a special form of the Navier-Stokes differential equation of motion, where the ratio of the inertial forces to the force of inner friction, the so-called Reynolds number (Re) is very small. With:

$$\text{Inertial force} = \rho * v_{flow}^2 / l \quad \text{and} \qquad (3.5)$$

$$\text{Force of inner friction} = \eta * v_{flow} / l^2 , \qquad (3.6)$$

$$Re = (\rho v_{flow}^2 / l) / (\eta v_{flow} / l^2) \qquad (3.7)$$

$$= \rho\, v_{flow}\, l / \eta \quad , \qquad \text{where}$$

ρ = density, q = velocity, l = characteristic length,
η = viscosity, Re = Reynolds number

The characteristic length l is not easy to determine, the conduits in the sediment being very complicated. However, taking l as the mean grain diameter d, the grain Reynolds number (Re') commonly used in Hydrology is obtained :

$$Re' = \rho\, v_{flow}\, d / \eta \qquad (3.8)$$

According to Unsöld (1983), this boundary condition of the Darcy Law, which requires a laminar flow in the medium, is fulfilled for $Re' < 5$. Taking $Re' \approx 1$, we obtain limiting values for the flow velocity or the maximum flow per unit time allowed for different grain sizes. With:

$$v_{flow} = q_v / A \quad , \text{where} \qquad (3.9)$$

q_v = flow volume

A = crossectional area of sample

Tab. 3.3: Flow volumes q_v measured in the samples P1, P2, P5 and P6.

D_{50} [µm]	$q_{v(max)}$
630 P1	9.78E-6
550 P2	1.37E-5
300 P5	2.28E-5
220 P6	3.42E-5

Since the q_v values measured in the laboratory, Tab.3.3, were much below these maximum values, the permeability measurements were in the limits of the validity range of the Darcy Law. The principle behind the permeability measurements in the P.T. apparatus is given in the pore fluid circuit diagram in Fig. 3.5, also described at length in Brandt (1984).
From the pressures P_A and P_B measured before the pore fluid enters the sample and immediately after it emerges respec-

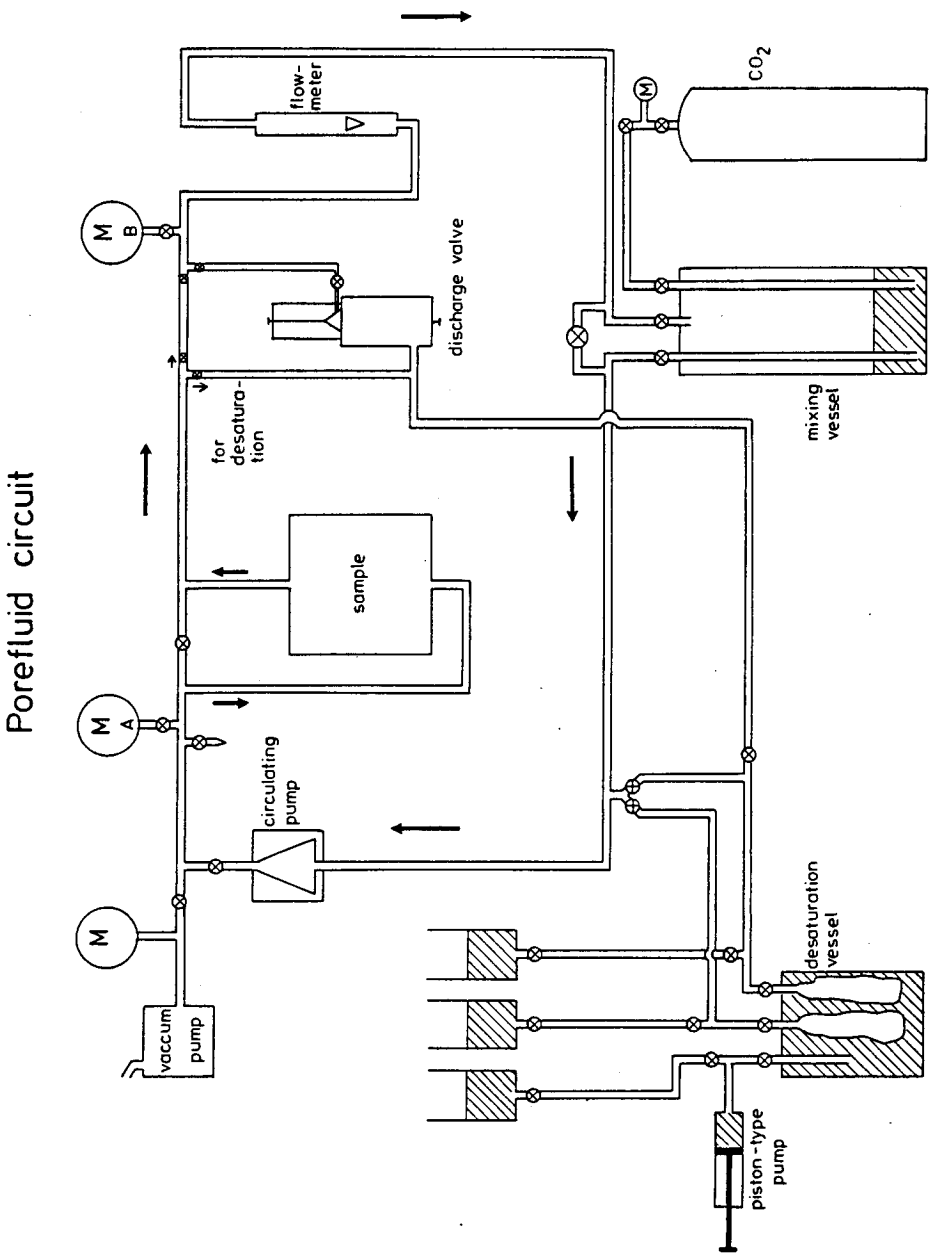

Fig. 3.5: Pore fluid circuit of the P.T. apparatus

tively, and the height to which the corundum floater rises in the flowmeter, the total volume of the pore fluid passing through the sample per hour, q_v can be calculated according to manufacturer calibrations. q_v is, among others, dependent on the permeability of the medium through which it passes. According to Darcy's Law :

$$k_f = V_{flow} * \eta * X / dP \quad , \tag{3.10}$$

where V_{flow} [m/s] : velocity of the pore fluid,
k_f [m^2] : permeability coefficient,
dP [kg/ms^2] : pressure gradient in the pore fluid,
η [kg/ms] : viscosity of the pore fluid,
X [m] : sample length.

Also:

$$V_{flow} = q_v / A = q_v/\pi/R(Pd)^2 \tag{3.11}$$

Assuming the relation between sample length and radius to remain constant ;

$$X_0^2 / R_0^2 = X(Pd)^2 / R(Pd)^2 \tag{3.12}$$

X_0, R_0 : length and radius at pressure = 0,
X(Pd), R(Pd): length and radius at pressure = Pd.

Knowing X(Pd), X_0 and R_0, R(Pd) can be calculated:

$$R(Pd)^2 = X(Pd)^2 * R_0^2 / X_0^2 \tag{3.13}$$

Substituting Eqn. 3.13 in Eqn. 3.11 we get :

$$V_{flow} = q_v * R_0^2 / \pi / X(Pd)^2 / R_0^2 \tag{3.14}$$

With equations 3.10, 11 and 14, k_f is obtained as follows:

$$k_f = q_v * \eta * X(Pd) / dP / A \qquad (3.15)$$
$$= q_v * \eta * X_0^2 / dP / \pi / X(Pd) / R_0^2$$

This value of permeability is an apparent permeability, k_f (total), containing both sample permeability, k (sample), and the apparatus resistance, k_f (app), due to the pipes, meshes, etc of the pore fluid circuit.

$$k_f \text{ (total)} = k_f \text{ (sand)} + k_f \text{ (app)} \qquad (3.16)$$

k_f (app) is found by taking a water sample jacketed by a plexiglas cylinder. In this case the total resistance to flow ($q_v*\eta/dP$) will be caused only by the apparatus, being negligible in water. Thus, with the additional subscript 'w' denoting corresponding values measured in a water sample;

$$k_f \text{ (app)} = X_{0W}^2/\pi/R_{0W}^2/X_W(Pd)*(q_{vw}*\eta/dP_W) \qquad (3.17)$$

$$k_f \text{ (sand)} = k_f \text{ (total)} - k_f \text{ (app)} \qquad (3.18)$$

$$= X_0^2/\pi/R_0^2/X(Pd)*(q_v*\eta/dP) -$$

$$- X_{0W}^2/\pi/R_{0W}^2/X_W(Pd)*(q_{vw}*\eta/dP_W)$$

Considering water to be incompressible,

$$k_f \text{ (sand)} = 1/\pi/R_0^2*(X_0^2/X(Pd)*q_v*\eta/dP - X_{0W}*q_{vw}*\eta/dP_W) \qquad (3.19)$$

Calibration of the System

Calibration of the system with water, at 20°C and a pressure gradient of 0.023 MPa, gave the flow / hour to be :

31.6 l/h or $8.78*10^{-6}$ m^3/s ,

and the resistance of the system ($dP/\eta/q_v$) as :

$2.62*10^{12}$ m^3 .

Despite of the above corrections in the permeability calculations, the values obtained from the P.T. experiment were extremely scattered (Fig. 3.6). This could be due to a desaturation container in the pore fluid circuit. This being larger in diameter than the pipes transporting the pore fluid, meant a reduction in the transport energy of the pore fluid, which in turn lead to erratic uncontrolled values of k_f being measured. The samples P1 and P5, measured without the desaturation vessel in the circuit do not show so much scatter. With this new configuration, k_f-values were again measured for the same samples (Fig. 3.6). The above calibration is done without the desaturation vessel in circuit.

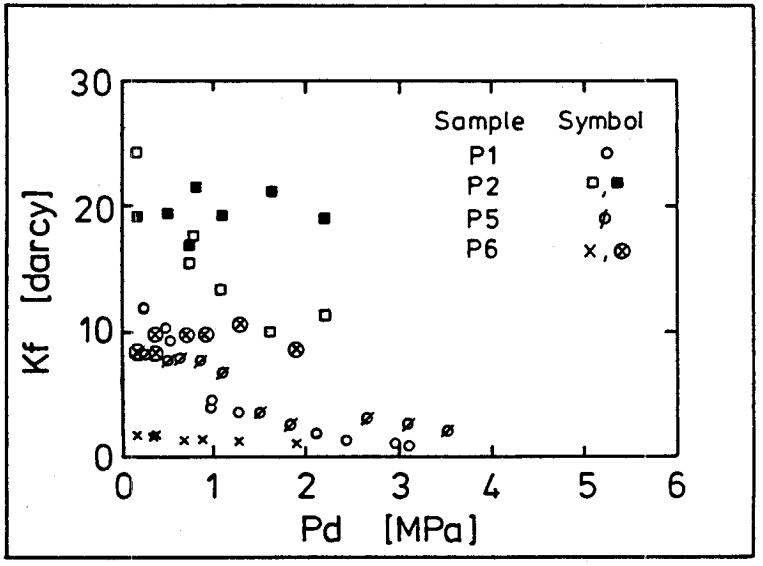

Fig. 3.6: Permeability values of P1, P2, P5, P6. The earlier measurements of k_f for samples P2 (■) and P6 (⊗) show much scatter and no decisive trend. Generally a decline in k_f with pressure is observed.

Odeometer Tests

The odeometer tests measure the compressibility of a soil and the change of void ratio with pressure. This compressibility is closely related to the Biot concept of seismic wave propagation through a saturated medium. In Biot's derivation, the medium is decoupled, with a frame and a pore fluid constituent. The frame constituent is greater than the actual solid frame, being increased by a portion of the fluid 'sticking' to the frame, the void ratio being reduced by this skin layer. The principle behind the Odeometer tests by Terzaghi is, that pressure applied to an aggregate is first borne by both pore fluid and the frame. The aggregate reacts with reduction of pore space and outflow of pore fluid until the pressure is borne by the frame alone. Depending on the permeability of the aggregate, the time taken for this adjustment is variable. Obviously, the Terzaghi case is a special case of the Biot theory, where there is no coupling between the liquid and the solid (frame) phase. However, whereas the Biot theory deals with the dynamic propagation of seismic waves, the Terzaghi theory restricts itself to the static compressibility of soils under pressure. The odeometer tests were carried out with the view to see practical proof of the theory, an empirical relationship between the two well defined dynamic and static compression moduli.

The Odeometer tests were carried out in the same pressure steps as the P.T. experiments. From the vertical strain and the applied stress, the rigidity coefficient or the modulus of deformation is calculated:

$$E_s = \delta\epsilon / \delta\sigma \qquad (3.20)$$

$$\delta\epsilon = \delta h / h_0 \qquad (3.21)$$

$$\delta\sigma = \sigma_2 - \sigma_1 \quad , \text{with} \qquad (3.22)$$

E_s = rigidity coefficient, $\delta\epsilon$ = vertical strain,
δh = change in length with pressure, h_0 = original length,
$\delta\sigma$ = change in stress applied.

The grain size dependence of E_s obtained from the tests are given in Fig. 3.7 for rounded (below) and for angular grains (above). The coarser grains have higher rigidity coefficients ie lower compressibility than finer grains. Also the angular grains possess lower values for E_s than their rounded counterparts, implicating that they are much more responsive to pressure.

Direct Shear Tests

The shearing resistance and the angle of inner friction of the samples were measured by this method. The normal stress and maximal shear stress at that step are introduced in the Coloumb-Mohr stress diagram as shown in the cartoon below, illustrating the relationship between normal and shear stress (τ and σ resp.), cohesive strength c and angle of inner friction φ.

$$\tau = c + \sigma \tan\varphi \qquad (3.23)$$

where

τ = shear stress
σ = normal stress
c = cohesive strength
φ = angle of inner friction

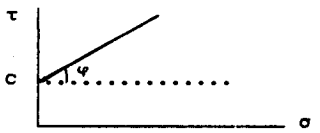

The angle of inner friction integrates all factors of resistance to grain displacements and depends mainly on the mineral, its shape, angularity and gradation. The measurements in the laboratory are presented in Fig. 3.8 for angular and rounded sands and two quartz powders and in Tab. 3.4, together with values of 'φ' from Sowers (1979). Almost all show very small values of 'c'. This is due to the capillary action causing an apparent cohesion. Also there seems to be a difference in 'φ' for rounded, angular and powdered grains. This fact shall be referred to in Sec. 5, where the seismic qualities are modelled.

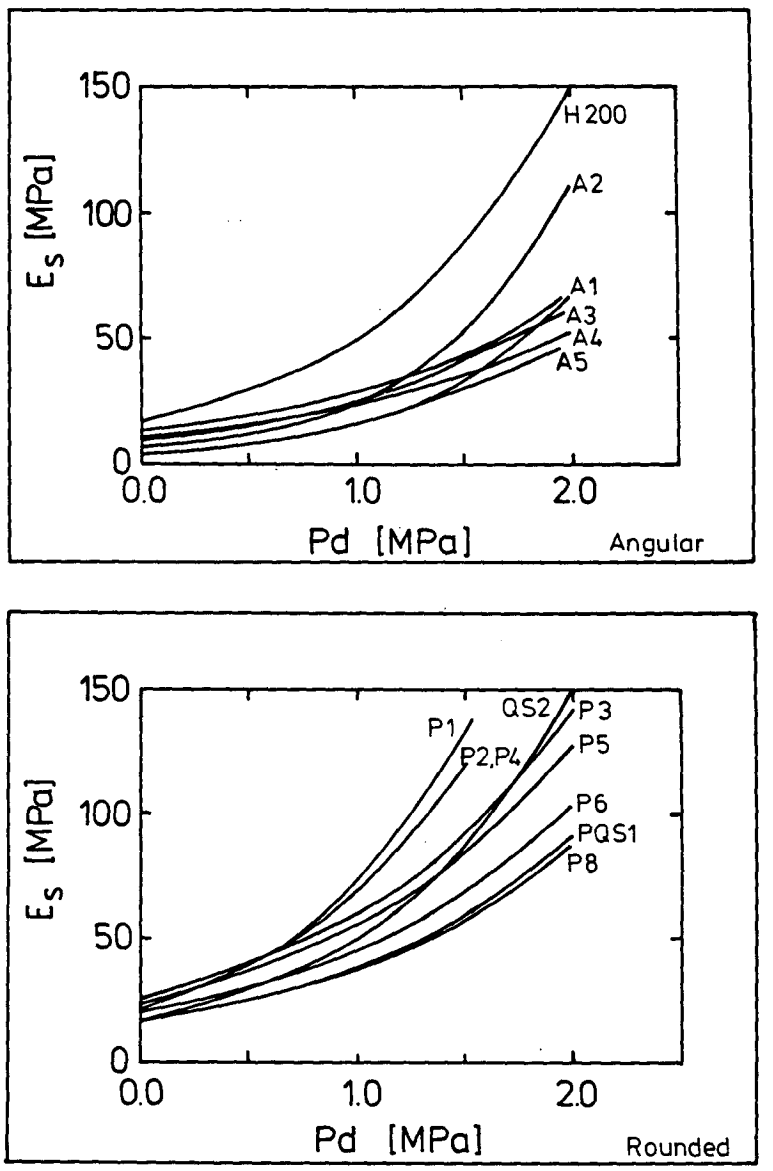

Fig. 3.7: Rigidity coefficients for rounded (bottom) and angular (top) samples. Rounded samples have higher rigidity coefficient values than the angular ones.

grain	sample	φ (average)	from Sowers 1979
round	P2	31°	29-35°
angular	A1,3	44°	35-42°
powder	F600, H200	33°	-

Tab. 3.4: Angle of inner friction for the different grain shapes. Angular grains show a higher angle.

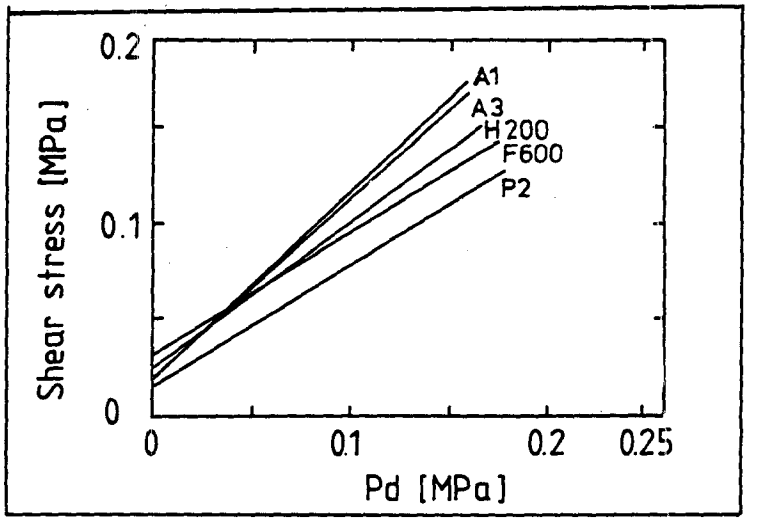

Fig. 3.8: Shear tests on rounded (P1), angular (A1, A3) and powdered (F600, H200) samples. The powders show higher (apparent) cohesive strength.

3.2 Seismic Measurements

There are various methods of studying the seismic quantities of sediments in the laboratory. Each of these methods has its own advantages and disadvantages. In Table 3.5 the four main methods are listed together with their frequency ranges and other characteristics.

Method	Freq. range	Geological Parameters	Advantage	Disadvantage	Authors/Reference
Pulse Transmission	ultrasonic P- and S-waves kHz to MHz	ϕ, ρ, permeability, density, saturation degree, temperature, preparations	very easy in implementation, simultaneous measurements of geological parameters	V(f) and Q(f) not easy to determine. Above 1MHz, strains > .001. 1/Q determ. indirect. Not in seismic frequency.	Toksöz et al (1979) Muckelmann (1985) Brandt (1984) Tarif (1986)
Pulse-echo	ultrasonic sonic to kHz to MHz	pore pressure, conf. pressure, ϕ, ρ	easy in implementation	assumes no-loss reflections at boundaries. Highly attenuating samples difficult to meas.	Winkler and Plona (1983) Hosten and Deschamps (1984)
Pendulum Resonance method bar	1-100Hz 1-20kHz	volatiles, thermal cycling and confining pressure, ϕ, ρ.	small samples and low frequency measurements. V(W) and Q(W) by changing sample length	assume reflections without losses. Employ standing waves; used in exploration are travelling waves.	Shumway (1956,1960 a,b); Gardener et al (1964); Winkler and Nur(1979); Gordon and Davis(1968) Tittmann (1978); Toksöz et al (1979) Peselnick and Outerbridge (1960)
Quasi-static	1-10Hz (-100Hz)	ϕ and ρ obtained simultaneously	V(W) and Q(W) directly measured on same sample. wide f-range with same setup. seismic frequency covered. High accuracy of measurements	very sensitive to noise and temperature. At higher frequencies, resonant oscillations of apparatus. Also measurements of permeability and saturation are problematic.	Gordon and Davis (1968) McKavanagh and Stacey (1974) Brennan and Stacey (1977) Spencer (1981) Jedicke (1984) Jackson (1986) Burkhardt et al (1986)

Table 3.5: Main laboratory methods of studying seismic properties

In this research the P.T. apparatus was used, which allowed P- and S- wave registration along with simultaneous measurements of physical parameters such as porosity, permeability, density etc at different confining pressures.

This Pulse transmission (P.T.) apparatus has been described in details earlier (Brandt, 1984; Muckelmann, 1985). The 'heart' of the apparatus, Fig. 3.9, consists of P- and S-wave transducers mounted on transmitter plates (3) on the two sides of a rubber casing holding the sample. The S-transmitter, with a nominal frequency ≈ 200 kHz is excited by a 10 volt amplitude and ca. 100 kHz frequency sinus wave. The P-transmitter, resonance frequency ≈ 50 kHz, is excited by the flank of a rectangular impulse (2). The pulse travels through the sediment / medium and is received on the other side by one S- and two P-wave transducers. The S-receiver is similar to the S-transmitter, the two P-receivers differ in their frequencies, one being more sensitive to higher frequencies (P2) than the other (P1).

The transmitter plate carrying the transducers also serves as an inlet/outlet for the pore fluid circulating through the sample. To prevent short circuiting, and wearing of the resin used to mount the transducers, they were cumbersomely isolated by a capsule adhered to the transmitter plate (Fig. 3.10), with fixed wiring for the electrical connections mounted on it.

This method had its shortcomings. First, it did not allow visual control of the transducers. Also, despite of the precautions taken, it was prone to leakage. Additionally, the resin used to glue the capsule required heat for drying and hardening. This meant heating the transducers too, which in turn mechanically wore the resin gluing the transducers to the transmitter plate.

This is solved in completely leaving out the capsule. Instead of hollowing out the carrier plate completely, see Fig. 3.11,

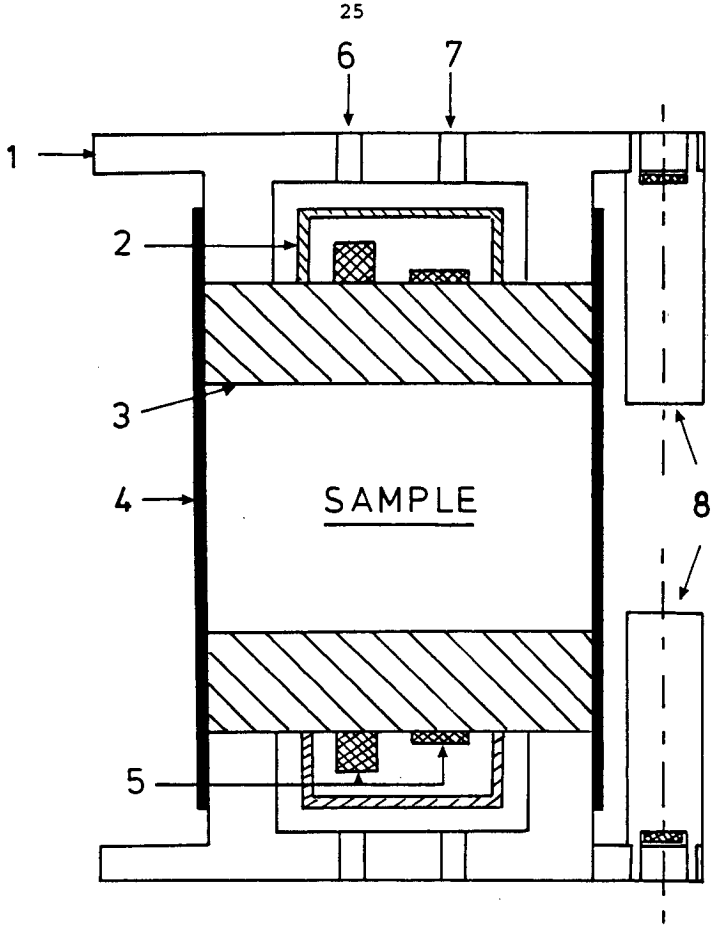

SAMPLE CONTAINER

Fig. 3.9: The sample container of the P.T. apparatus

one portion is left standing as a ring wall separating two areas: one for the pore fluid, and second for the electrical installations. Now, with this, in screwing the transmitter plate to the carrier plate, the separator ring fits in the slot of the transmitter plate with O-rings at the bottom, thus isolating effectively the transducer area from the pore fluids. The length sensors were also isolated in a similar manner using screws and O-rings.

The main inadequacy of the apparatus is, however, the gluing of the transducers to the transmitter plate. Despite data sheets information on the resin, this is not long lived. The six hour pressure steps in the unpressed samples, meant a continuous usage of about 2.5 days as opposed to about 10 hours for the pressed samples and wore the gluing much more so that after about two to three pressure cycles, it was necessary to reglue the transducers and calibrate the system again. One solution to this would be to use transducers which can be screwed to the plate instead of having being glued.

This handicap posed severe limitations on the total number of experiments that could be performed in an appropriate time limit. Of the 31 samples reported in Sec. 3.1, 11 could be examined with the P.T. apparatus, giving a total number of $\approx$ 20 experiments.

These experiments were performed in two modes.

In one, the sample was taken in its natural condition. However, between two pressure steps, enough time was left to allow the sample to settle at that pressure. This time was estimated by measuring the change in the arrival of P-waves with the time elapsed, at one pressure. The results are given in Fig. 3.12, where the change is plotted against time elapsed. Since beyond 5.5 hours no noticeable change was seen, the time alloted for settlement between two pressure was taken as six hours. The samples measured in this series

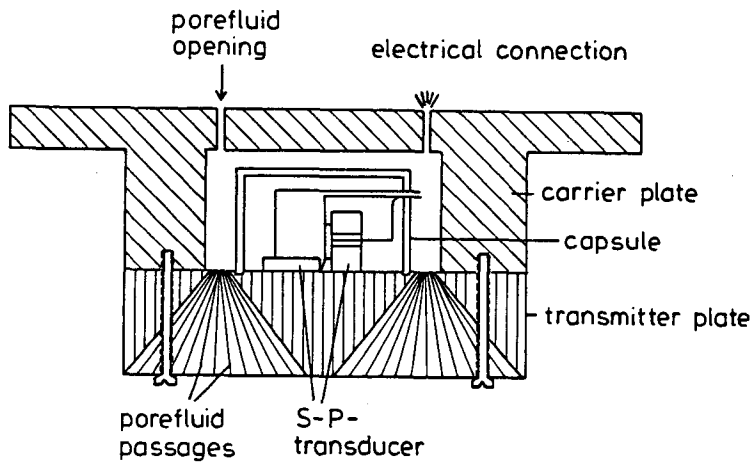

Fig. 3.10: Earlier mounting of the transducers on the carrier plate

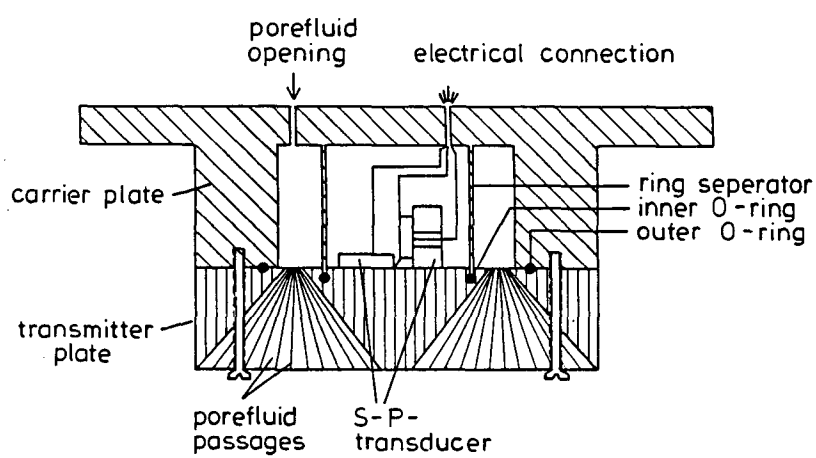

Fig. 3.11: Mounting of the transducers on carrier plate

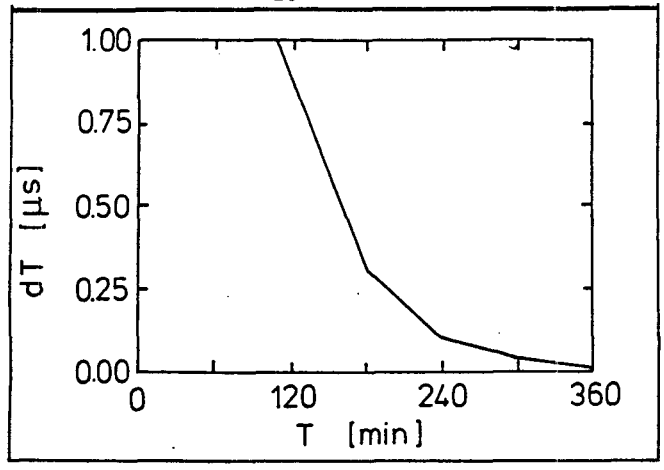

Fig. 3.12: Change in arrival time of P-waves with time elapsed. Beyond 5 hours, the travel time does not change considerably.

shall be referred to as the unpressed samples. In the second series, the sample was pressed prior to the experiment to a confining pressure of 20 MPa for about 12 hours. These measurements were also made to compare the present values with previous works on the apparatus, those being solely of the second type. The pressing of the samples suppresses pressure hysteresis, but it also changes the sample characteristics, resulting in increased velocities and densities, and decreased attenuations and porosities. Also the grain size analysis in Fig. 3.13 shows the shift in the curves towards finer grain sizes as a result of the 20 MPa pressing. The samples examined in this series shall be referred to as the pressed samples.

For data acquisition and interpretation, a Data General computer was used (Huszak, 1986), which facilitated attenuation calculations. Attenuation or the seismic Quality factor Q can be evaluated by different methods, eg spectral ratio (Toksöz et al, 1979), rise time (Gladwin and Stacey, 1974), wavelet and spectral modelling, (Jannsen et al, 1985), analytical signal (Engelhardt, 1985). Reference to the different methods is given by Tonn (1987).

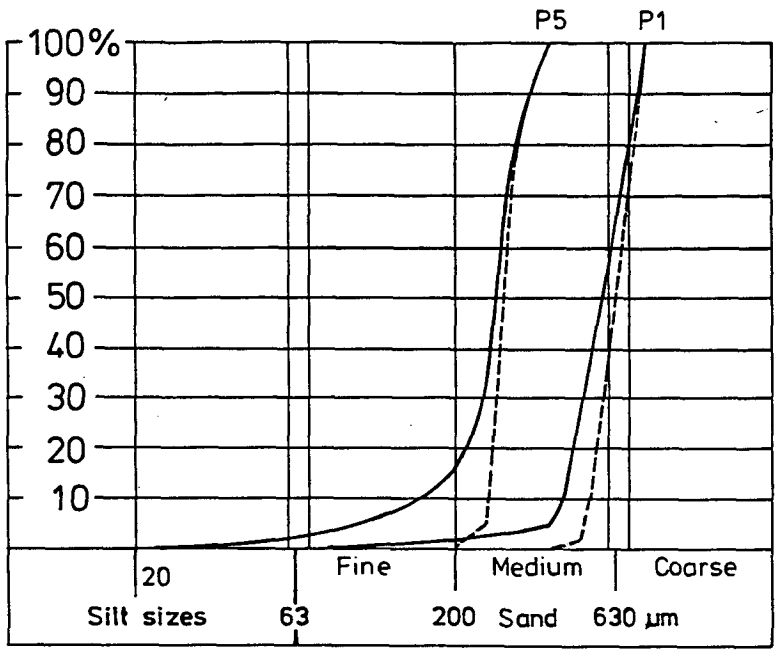

Fig. 3.13: Shift in grain size towards finer fractions after pressing to 20 MPa in fine (P5) and coarse (P1) grains. Broken lines represent original grain sizes, solid curves are measured after pressing.

The spectrum ratio method (Toksöz et al, 1979) determines the quality factor of a sample by comparison with the reference sample having negligible attenuation. With the amplitudes expressed as:

$$A(w,t,x) = A_0 G(x) e^{-\alpha x} e^{i(kx-wt)} \quad , \quad \text{with} \qquad (3.24)$$

x: distance
t: time
w: frequency
k: wave number
G(x): geometrical factor
A_0: amplitude of source signal
α: attenuation coefficient

The ratio of the fourier amplitudes of sample and standard signals, denoted by subscripts 1 and 2 resp., is:

$$A_1/A_2 = G_1/G_2 * e^{-(\alpha_1-\alpha_2)x} \quad \text{or}$$
$$\alpha_1-\alpha_2 = 1/x * [\ln(G_1/G_2)-\ln(A_1/A_2)] \qquad (3.25)$$

taking the same geometry for both. If the geometrical factor (G_1/G_2) is assumed to be constant with frequency, and the attenuation coefficient in the standard $\alpha_2 \approx 0$ or $Q_2 \approx \infty$, the attenuation in the sample is directly obtained from the slope of the amplitude ratios over the frequency.

The rise time method (Gladwin and Stacey, 1974) is an empirical relationship between the rise time τ, defined as the ratio of the maximum slope of a signal to its amplitude, and the attenuation:

$$\tau = \tau_0 + ctQ^{*-1} \qquad \text{with c: constant} \qquad (3.26)$$
τ_0: rise time of source signal
t: travel time

The value of c, given as a constant = 0.45 by the above authors, is found to vary for different sources and receivers (Burkhardt et al, 1986, Muckelmann, 1985).

An estimation of 'c' with another method is required for the correct determination of 'Q' in the samples by this method. Considering the straight line relationship in eqn. 3.26, in plotting the rise time τ against t/Q^* , $1/Q^*$ obtained from another method, gives 'c' as the slope of this line and $'\tau_0'$ as the axis segment. Such a calibration is given in Figs. 3.14 and 3.15.

A comparison of these and other methods is given by Tonn (1987) and Engelhardt (1985). The tests are carried out on synthetic seismograms with different noise levels. All methods are noise dependent, the reliability of 'Q'-determination dimishes with increasing noise levels, and the Rise time method is seen to be more sensitive to noise. In noise

free data the spectrum division method and the analytical signal method yield best results, the Rise time method being less reliable. But the authors admit this as being due to a low sampling rate of the signal and taking 'c' as a constant. Thus in the almost noise free data obtained in the laboratory, the two methods, Rise time and Spectrum division, were used, where the Rise time method was calibrated with the Spectrum division method, for each configuration of the sources and receivers, Figs. 3.14 and 3.15.

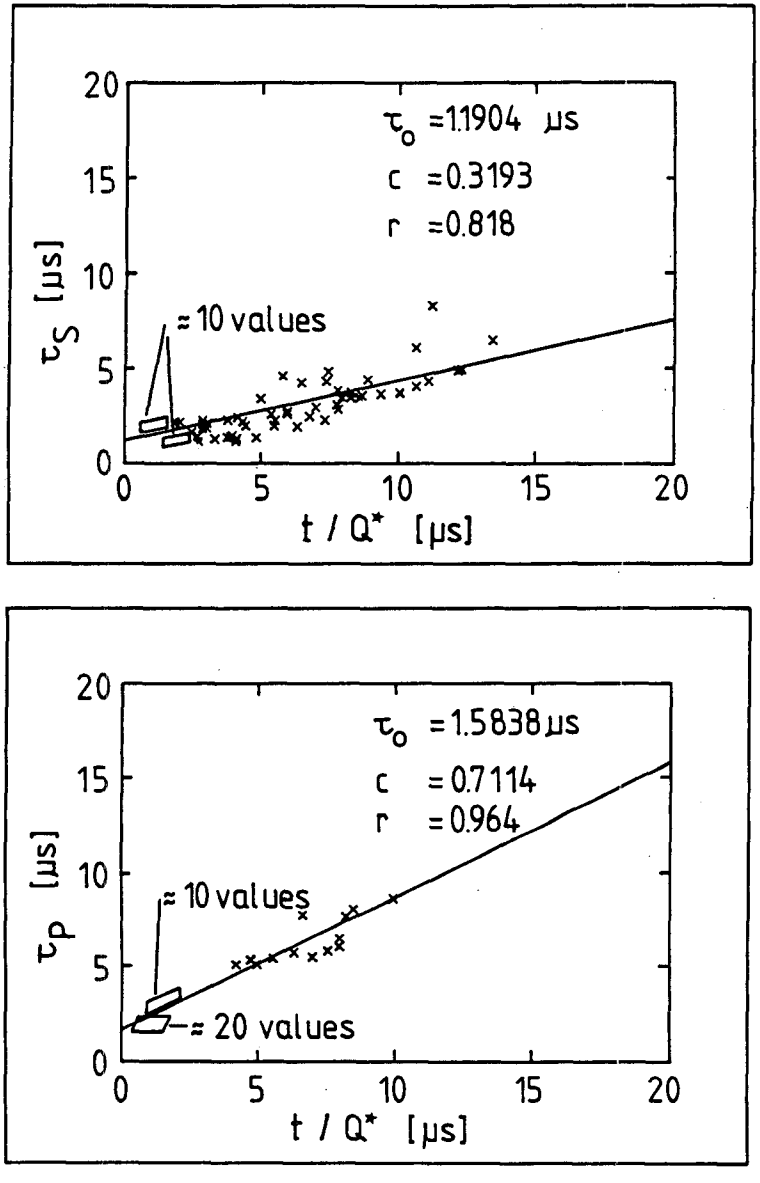

Fig. 3.14: t/Q^* versus rise time τ for P-waves (bottom) and for S-waves (top) for the determination of 'τ_0' and 'c' for samples P1...P6, A1...A4

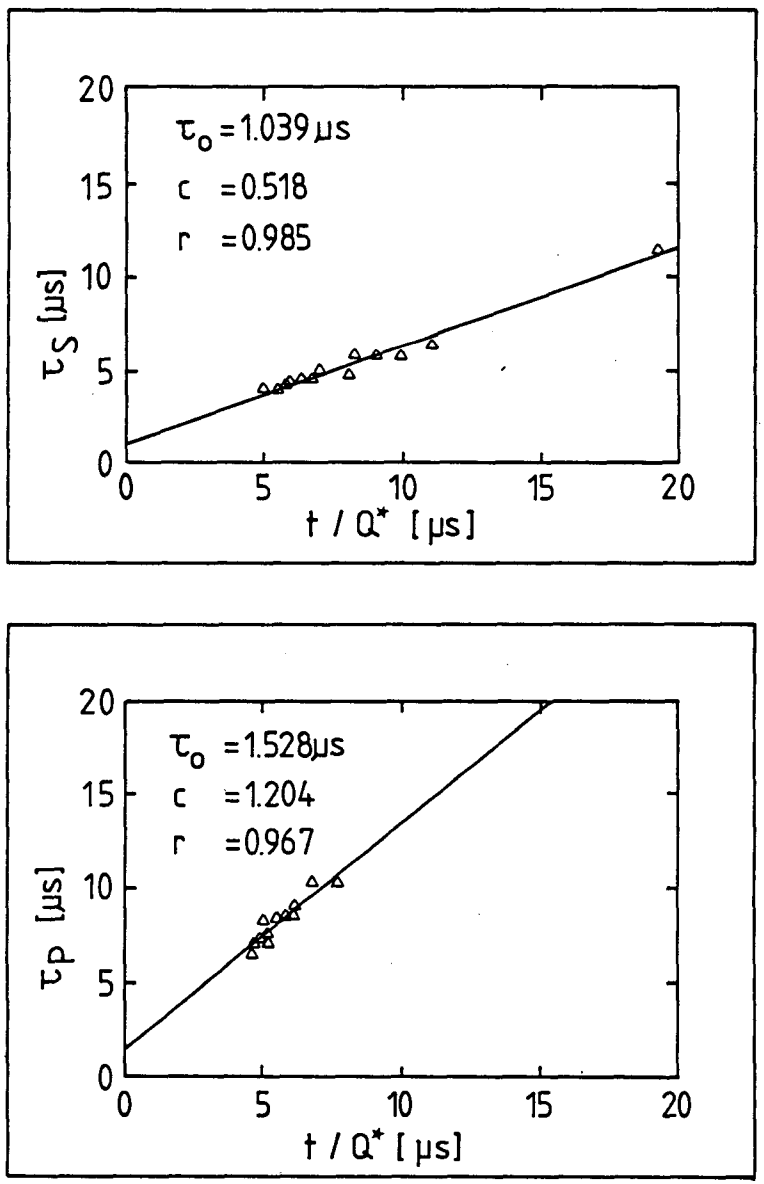

Fig. 3.15: t/Q^* versus rise time τ for P-waves (bottom) and S-waves (top) for the determination of 'τ_0' and 'c' for the sample H200.

4. Results of the Pulse Transmission Experiments

As described in Sec. 3.2, the Pulse Transmission (P.T.) experiments were carried out in two different pressure cycles; one on sands pressed prior to the experiment and second on unpressed sands but with enough time between pressure steps for the sample to settle. In both cycles dry samples (vaccum of -1 bar) and fully water-saturated samples were examined.

In the following, unless specifically mentioned, when saturation is written, it means water saturation. An overview of the total number of experiments performed is given in Table 4.1.

shape	sample	unpressed		pressed	
		dry	saturat.	dry	saturat.
rounded	530 - 760µm P1	xx	xx		xx
	500 - 620µm P2		xx		xx
	300 - 400µm P3		xx		
	270 - 450µm P4		xx		
	255 - 370µm P5		xx		xx
	160 - 270µm P6	xx	xx		xx
angular	310 - 440µm A1	xx		xx	
	200 - 300µm A2		xx		
	52 - 140µm A4	xx		xx	
qz.powd.	9 - 30µm H200	xx		xx	

Table 4.1: Overview of experiments performed

Since the pressed and unpressed samples are physically much different from one another, their results shall be reported separately. The relevance of the geologic experiments and their relation to the seismic quantities shall be discussed in Sec. 4.4. The symbols used in all figures are given in Table 4.2.

Sample	Shape	Median D_{50}	Permeability (Darcy)	Symbol
P1	round	650	58.79	o
P2	round	550	43.26	□
P3	round	440	19.98	*
P4	round	360	21.01	+
P5	round	300	13.56	◊
P6	round	220	8.36	x
A1	angular	360	21.53	⊠
A2	angular	255	10.56	△
A4	angular	91	2.42	▽
H200	powdered	20	0.12	⊗

Table 4.2: Grain shape, median and permeability of the samples

4.1 Unpressed Samples

These samples were not pressed prior to the experiment. The pressure cycle was carried out on two types of samples: saturated and dry.

4.1.1 Fully Saturated Sands

In this series, six rounded and one angular samples of different grain sizes were examined. The grain size analysis of the samples are given in Fig. 3.1. The geotechnical properties have been discussed in Sec. 3.1. The coarser samples have higher permeability, rigidity coefficient and density and lower porosity. The angular samples have lower rigidity coefficient than similar rounded grains. This relationship is also reflected in the seismic properties.
The P-wave velocity V_p in Fig 4.1 (bottom) has higher values in coarser samples than in finer ones and rises monotonously with pressure for all. The angular sample A2 with smaller rigidity coefficient shows lower V_p-values than similar grainsized rounded sample P6.

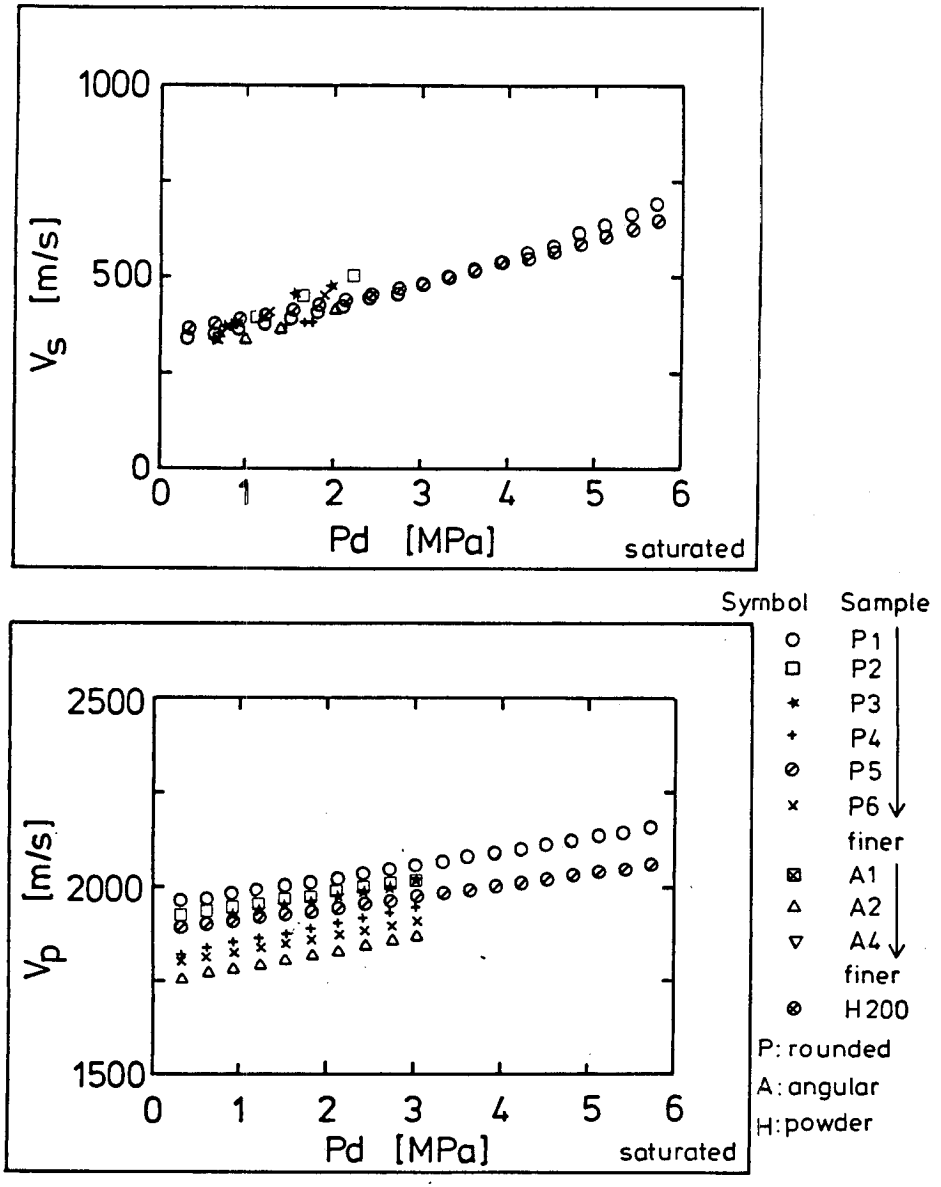

Fig. 4.1: V_p (bottom) and V_s (top) in unpressed fully saturated samples P1...P6 and A2. V_p shows clear grain size dependence, also the angular A2 has least V_p-values. V_s-values for all grain sizes are the same.

In contrast to V_p, the S-wave velocity V_s shows no dependence on grain size and shape (Fig 4.1, top).

The attenuation of P- and S-waves (Q_p^{-1} and Q_s^{-1}) respectively, show strong grain size dependence, with different characteristics however. The coarser grains show higher damping of P-waves than finer sands (Fig. 4.2, bottom). Also, with increasing pressure, an anomalous behaviour of the coarser grains is observed. Here, as pressure increases, Q_p^{-1} seems to increase slightly. Since the samples P2,3,4,6 and A2 were examined first, and so not expecting the anomalous behaviour, the pressure cycle was carried out to 2.5 MPa only. Thus P2 and P3 show only the increase in Q_p^{-1}. The second series was extended to 6 MPa (samples P1 and P5). In the coarser grained P1 again an increase in attenuation is noticed upto a certain limit beyond which it remains more or less constant. This effect is not seen in the finer grained samples P5 or P6, where Q_p^{-1} remains constant or decreases slightly with pressure. The consequences of these results will be discussed in Sec. 5.

Q_s^{-1} decreases with pressure for all samples (Fig. 4.2, top). The coarser grains show higher damping than finer grains, though the gradient of decrease in damping with pressure is higher in coarser than in finer sands.

4.1.2 'Dry' Sands

This was the first series to be measured. The dryness was obtained by oven drying the sample prior to the experiment and a vaccum of nearly one atmospheric unit during the pressure cycle. However, as the results indicate, the moisture gained by the sand in assembling the apparatus could not be extracted by this.

Five samples (two rounded, P1 and P6, two angular, A1 and A4, and one powdered, H200) were measured in this series.

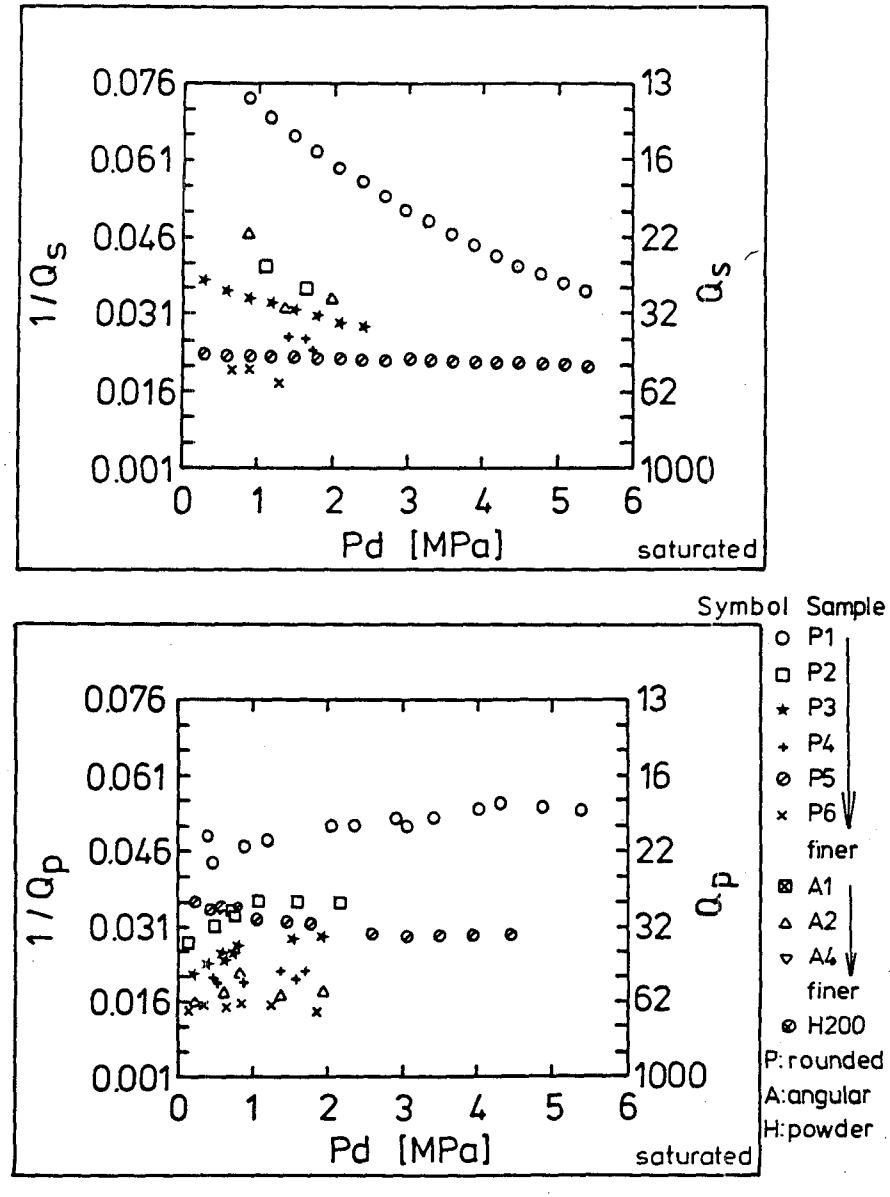

Fig. 4.2: Q_p^{-1} (bottom) and Q_s^{-1} (top) in unpressed fully saturated samples P1...P6, A2. The coarse grains show higher attenuation values. Q_p^{-1} in coarse samples P1...P3 shows slight increase at low pressure, in finer samples P4...P6 the increase is not seen.

Fig. 4.3, bottom, presents the V_p in all samples, P1, P6, A1, A4, and H200. There is a marked dependence on grain size as well as on grain shape. The coarser grained samples P1 and P6 show higher values than A1, A4 and H200.

As in the saturated samples, V_s (Fig. 4.3, top) is same for all samples, except for the quartz powder H200, where it lies lower.

The attenuation in the dry samples is higher than or same as in saturated ones, with the Q_p^{-1} values in Fig. 4.4, bottom, showing similar characteristics as in V_p. The coarse grained P1 and A1 show higher values than fine grained P6 and A4. Also finer and angular grained A4 shows similar values as the comparatively coarser and rounded grained P6. The quartz powder H200 has the highest Q_p^{-1} values.

In Q_s^{-1} the same behaviour is seen (Fig. 4.4, top), the quartz powder H200 having the highest attenuation, followed by coarser grained P1. The angular grained samples do not show much difference in their attenuation values. The attenuation in the finer and angular grained A4 lies much higher than in the finer and rounded grained P6. Also the gradient of Q_s^{-1} decrease with pressure is higher for the coarser sands and for the powdered H200 sample.

4.2 Pressed Samples

Here too, saturated and vaccum dry samples were examined. In general the pressed samples had a very different behaviour from the unpressed ones, with velocities increased and attenuation decreased considerably, mainly due to grinding of the grains at such high pressures, with the quartz powder thus produced settling in the pore voids and strengthening the matrix. This has been illustrated in Fig. 3.13 where the

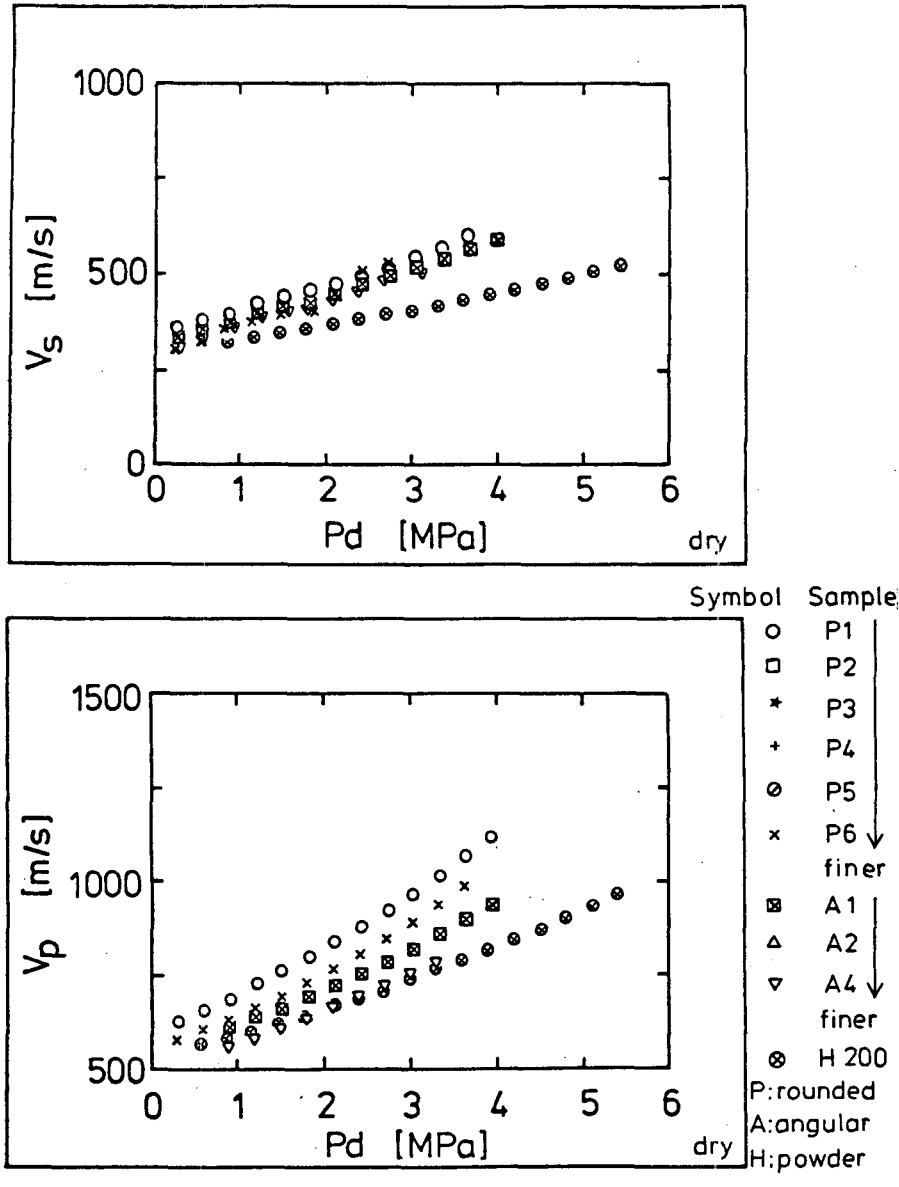

Fig. 4.3: V_p (bottom) and V_s (top) in unpressed dry samples P1, P6, A1, A4 and H200. A grain size dependence observed for V_p is not seen in V_S.

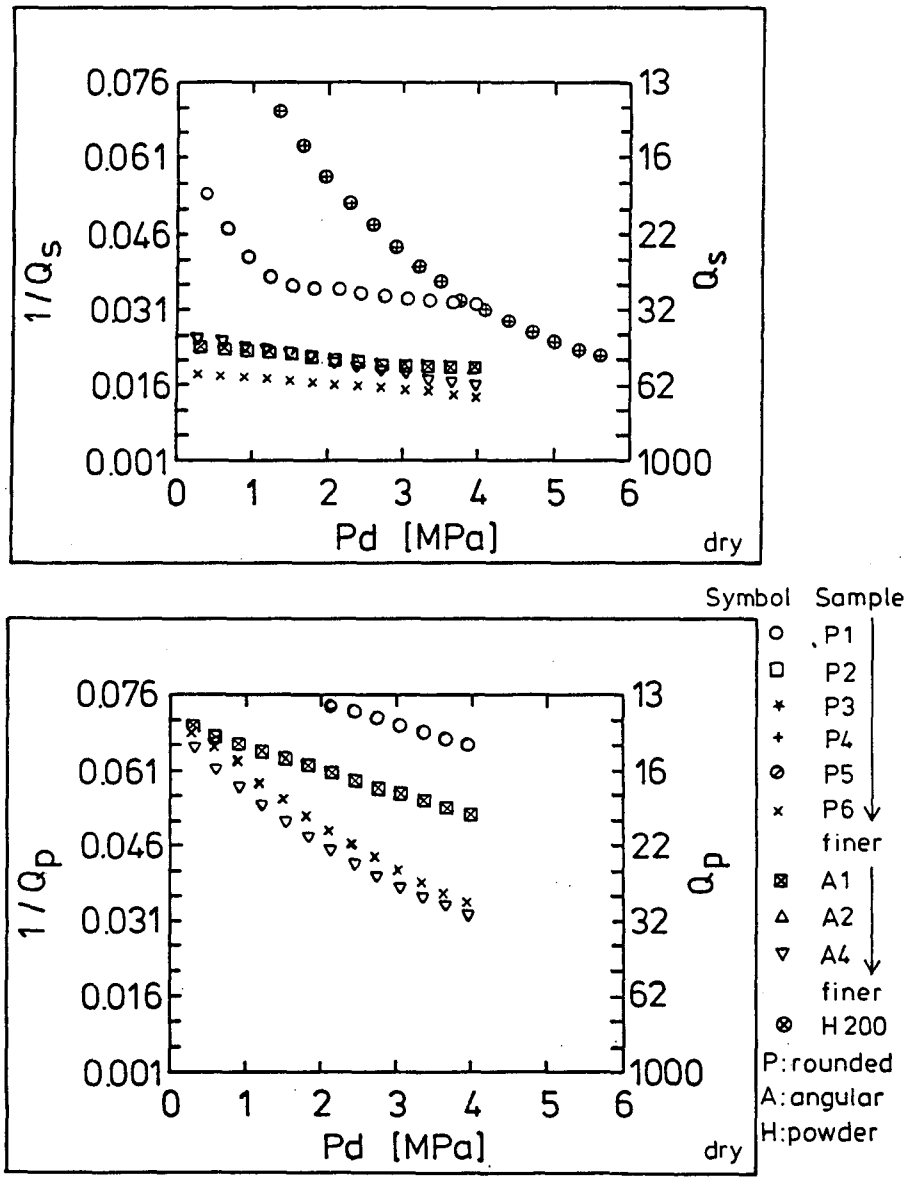

Fig. 4.4: Q_p^{-1} (bottom) and Q_s^{-1} (top) in unpressed dry samples P1, P6, A1, A4 and H200. Both Q_p^{-1} and Q_s^{-1} are higher in the coarser samples.

grain size curves of a sample before and after the application of 20 MPa pressure show crushing of the coarser grains.

4.2.1 Fully Saturated Sands

All samples examined here were rounded with two coarse grained P1 and P2 and two fine grained P5 and P6 sands.

The V_p and V_s show same characteristics as unpressed samples. V_p (Fig. 4.5, bottom) shows a grain size dependence whereas V_s (Fig. 4.5, top) is seemingly unaffected by the grain size.

Q_p^{-1} and Q_s^{-1} (Fig. 4.6, bottom and top) is higher in the coarser P1 and P2 than in finer P5 and P6. Whereas there is slight reduction in Q_p^{-1} with pressure, the Q_s^{-1}-decrease with pressure is more pronounced.

4.2.2 'Dry' Sands

Three samples were examined in this pressure cycle, angular, A1 and A4, and powdered, H200.

The quartz powder H200 has lower V_p than A1, Fig. 4.7, bottom. V_s, Fig. 4.7, top, is same in both A1 and A4 and lower in H200.

Attenuation in H200, Fig. 4.8, Q_s^{-1} top and Q_p^{-1} bottom, is much higher. But it also decreases very rapidly with pressure. Q_p^{-1} in coarser A1 is higher at lower pressures and falls below that of the finer A4 at higher pressures. Q_s^{-1} in A1 however remains higher than in A4.

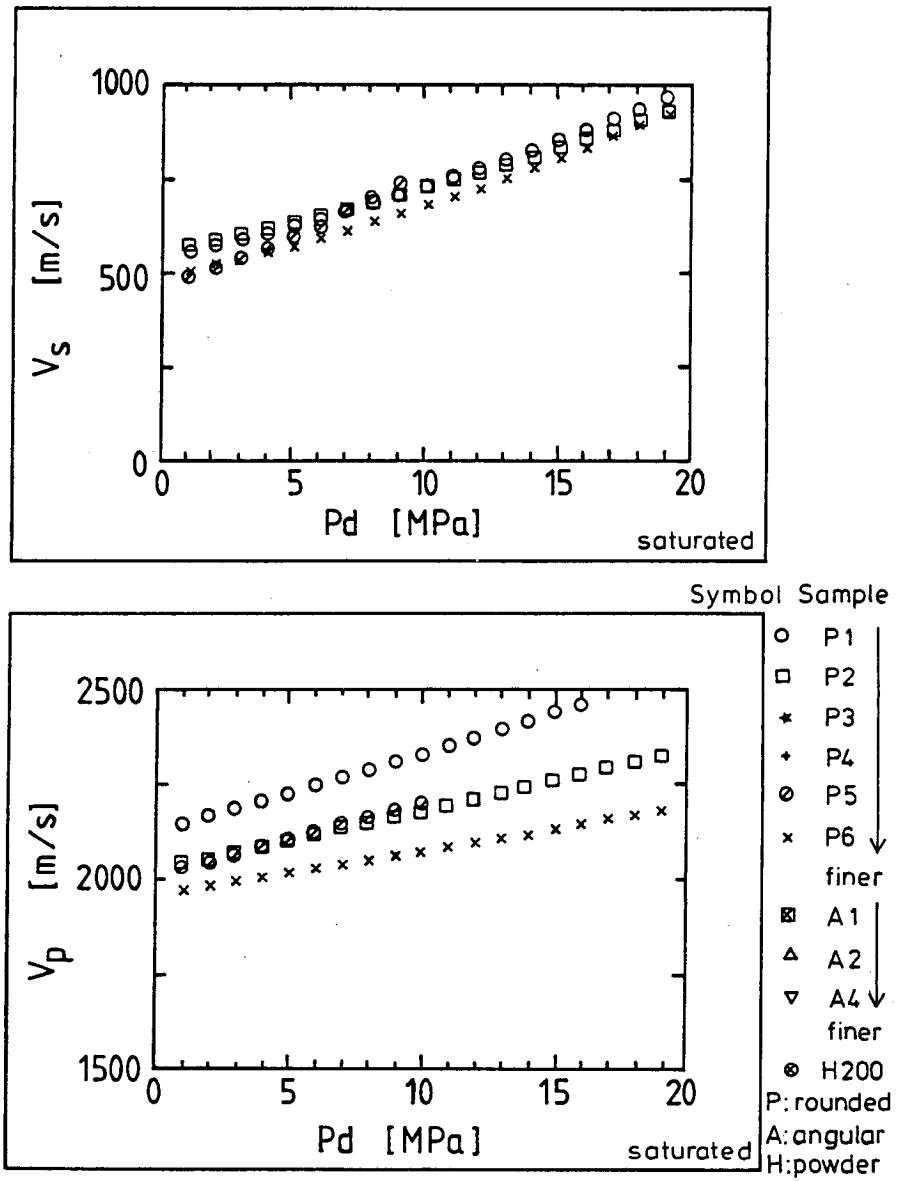

Fig. 4.5: V_p (bottom) and V_s (top) in pressed fully saturated samples P1, P2, P5 and P6. The grain size dependence of V_p is not reflected in V_s.

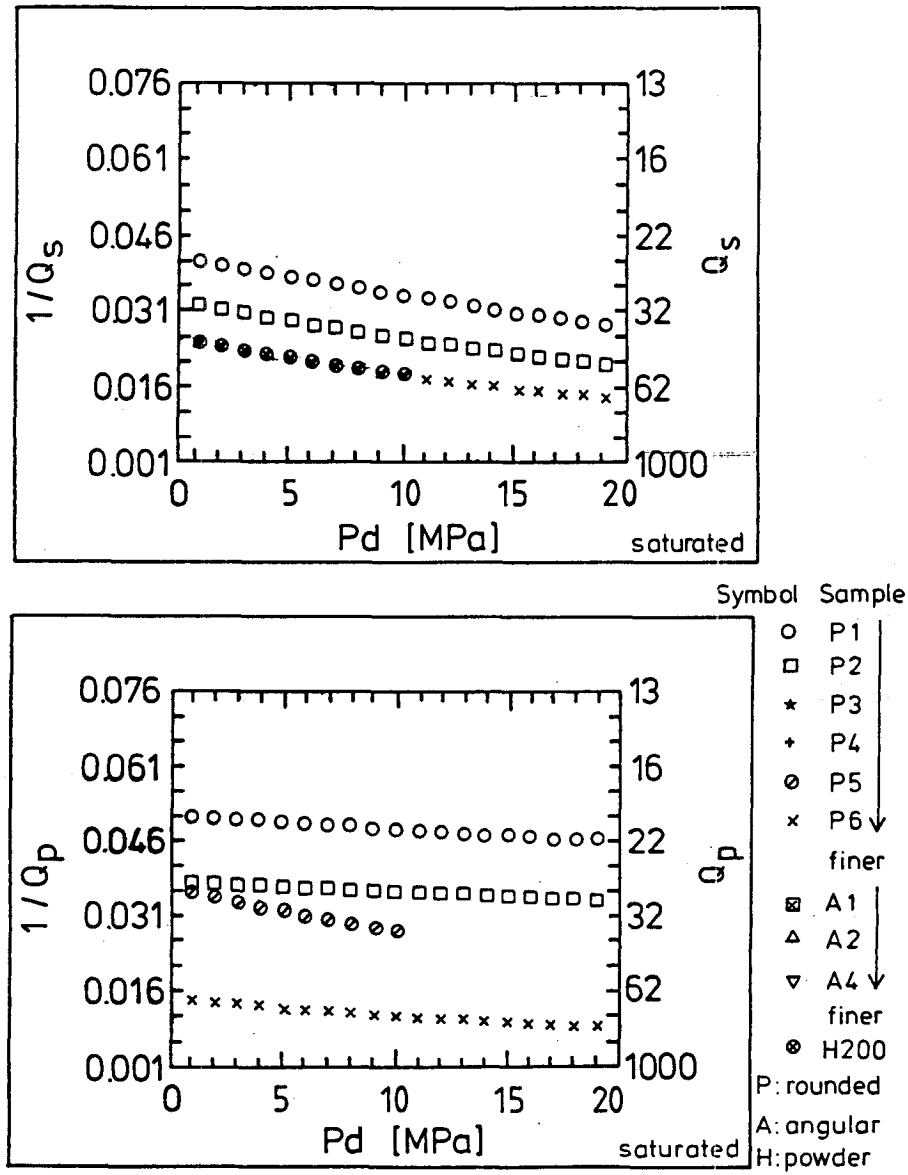

Fig. 4.6: Q_p^{-1} (bottom) and Q_s^{-1} (top) in pressed fully saturated samples P1, P2, P5 and P6. Both Q_p^{-1} and Q_s^{-1} are higher in coarser grains

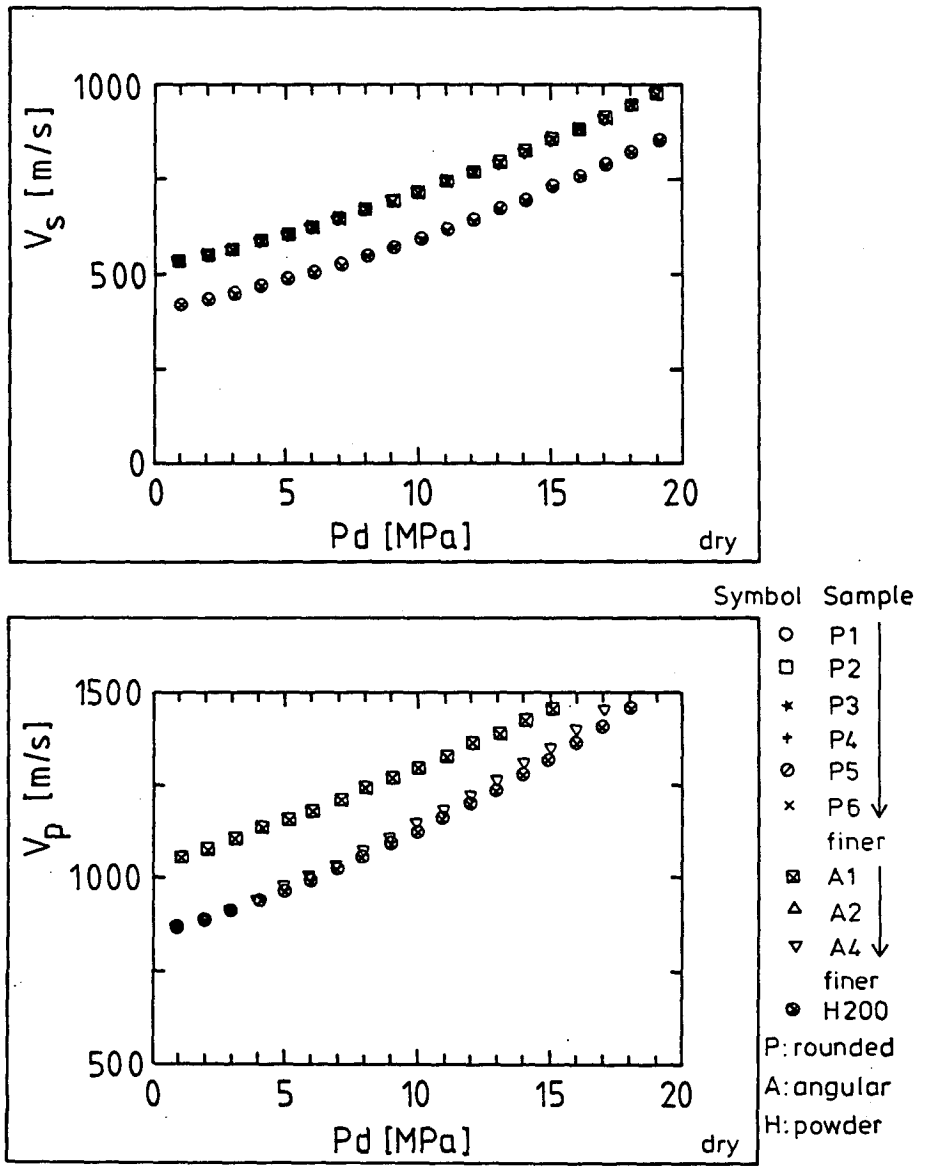

Fig. 4.7: V_p (bottom) and V_s (top) in pressed dry samples A1, A4 and H200. H200 has lower values of V_p and V_s.

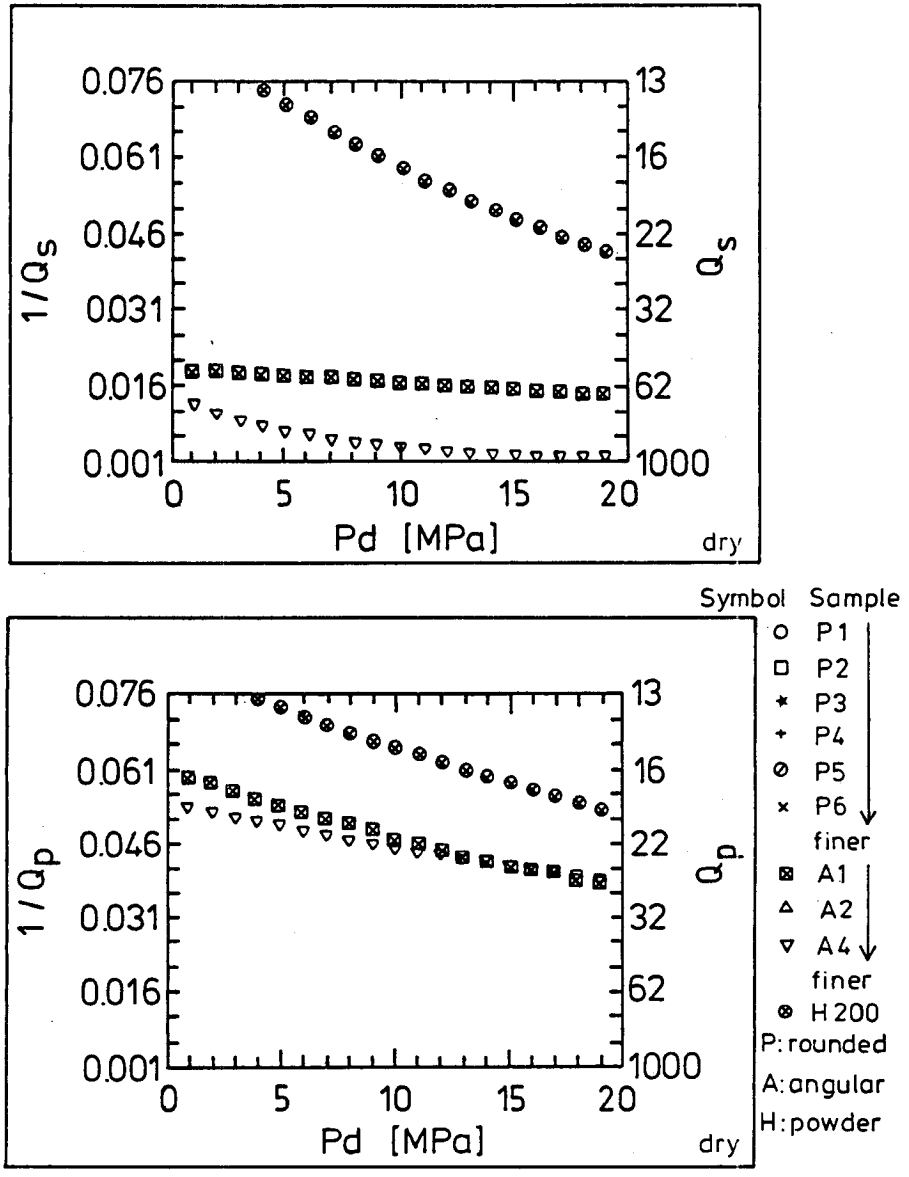

Fig. 4.8: Q_p^{-1} (bottom) and Q_s^{-1} (top) in pressed dry samples. Attenuation is highest in the powdered H200.

4.3 Summary of the Results

Two main differences between the dry and saturated samples were observed:

1.) Generally a higher attenuation was observed in the dry samples.

2.) V_p was lower in dry samples, but V_s remained more or less constant.

The following results can be summarized from the two different types of experiments:

1) V_p is higher in coarser grains than in finer ones.

2) Angular grains have lower V_p values than rounded ones, the quartz powder has lower V_p values.

3) V_s is not influenced by grain size, grain shape and saturant, but it is reduced in the quartz powder.

4) Q_p^{-1} (dry) decreases with grain size and with pressure.

5) Q_p^{-1} (saturated) also decreases with grain size.

6) Q_p^{-1} (dry and saturated) is higher for angular than for rounded grains.

7) In priorly pressed and unpressed fine grained sands Q_p^{-1} decreases with increasing pressure.

8) In priorly pressed saturated coarse grained sands Q_p^{-1} remains constant with pressure.

9) In unpressed coarse grained sands Q_p^{-1} increases slightly with pressure until a certain value.

10) Q_s^{-1} (dry and saturated) decreases with increasing pressure and decreasing grain size.

11) The gradient for decrease in Q_s^{-1} is larger for coarser than for finer sands.

12) Q_s^{-1} (dry and saturated) is higher for angular grains than for rounded ones.

13) The quartz powder shows very low V_p and V_s values and highest Q_p^{-1} and Q_s^{-1} values.

4.4 Interpretation of the Results

The results of the P.T. experiments gave a few unexpected and new results, which could be important to understand the mechanisms of seismic wave propagation in sediments. Also the broad range of grain sizes measured, coupled with physical parameters could be useful in forecasting characteristics of reflectors registered from seismic data and for an interactive in situ study of sediments with respect to physical and seismic properties.
The physical properties, grain size, shape, ϕ, ρ, k_f and E_s interact between each other and the seismic quantities. These effects seen are summed up in Table 4.3 for the physical properties together with seismic quantities.

With these prominent relationships, it should be possible, with information on one set, tc forecast the other. But relating some physical property to a seismic quantity has its shortcomings. Foremost, they tend to overestimate the effects of one property.

increase in	V_p	V_s	Q_p^{-1}	Q_s^{-1}
grain size	increase	unaffected	increase	increase
roundness	increase	unaffected	decrease	decrease
Φ (decrease in ρ)	decrease	unaffected	(decrease)	(decrease)
permeability	increase	increase	increase	increase
E_s	increase	increase (unaff.)	increase	increase
pressure	increase	increase	anomalous	steep decline

Table 4.3: The interaction between physical parameters and P- and S-velocities and attenuations

Raymer et al (1980) have also proposed empirical equations both for unconsolidated ocean sediments and consolidated rocks.

$$\frac{1}{\rho V_p^2} = \frac{\Phi}{\rho_f V_f^2} + \frac{1-\Phi}{\rho_s V_Q^2} \qquad \text{for } \Phi > 45\% \text{ unconsolidated sediments} \qquad (4.2a)$$

$$V_p = (1-\Phi)^2 V_Q + \Phi V_f \qquad \text{for } \Phi < 30\% \text{ consolidated rocks} \qquad (4.2b)$$

V_p: composite P-wave velocity — Φ : porosity
V_Q: P-wave velocity in solid component — ρ_s: solid density
V_f: P-wave velocity in fluid component — ρ_f: fluid density

But for sands, with normal porosity values below 45% the Eqn. 4.2a furnishes lower and Eqn. 4.2b higher values for the measured data.

Moreover, this relationship is not unique. In Fig. 4.9 the density and porosity values at different pressures lie on a straight line for different samples. However, in Fig. 4.10, with 'V_p' plotted against ϕ, although two samples P3 and P4 have same density and porosity, the coarser grained P4 has a higher velocity than finer grained P3. Thus porosity comparisons are not sufficient for 'V_p' prediction or vice versa.

One possible explanation for this could be the velocity dispersion due to Biot's flow in the sample. Since P4 has a higher permeability, the dispersion due to viscous flow, to be explained in Sec. 5, is not as large as in P3. Thus P4 would have higher velocities.

Also, the Odeometer tests (Fig. 3.7) show P4 to have higher rigidity coefficients than P3. This would also play an important role in controlling the matrix properties contributing to the total velocity. The increase in the rigidity coefficient is reflected in the dynamic bulk modulus; but not in the shear modulus which is unaffected by grain size.

In Fig. 4.11 'V_p' is plotted against 'E_s' to detect possible relationships between the two. The plots suggest a linear relationship between the two for small 'E_s'-values. However, at higher 'E_s'-values, corresponding to higher pressures, the curves separate with higher 'V_p' for coarse grained P1 and lower 'V_p' for the angular A2 or rounded P6 at the same 'E_s'-value.

The losses encountered by the seismic waves in a sediment can best be presented in a $(V_p/V_s)^2$ versus (Q_p/Q_s) diagram. This diagram, discussed by Winkler and Nur (1982), Meißner and Theilen (1983) and Muckelmann (1985), helps to differentiate whether the losses taking place in a sediment are in bulk or in shear. The laboratory data for dry and saturated samples are plotted in such a 'loss diagram' in Fig. 4.12. A clear demarcation of the areas occupied by the different samples is

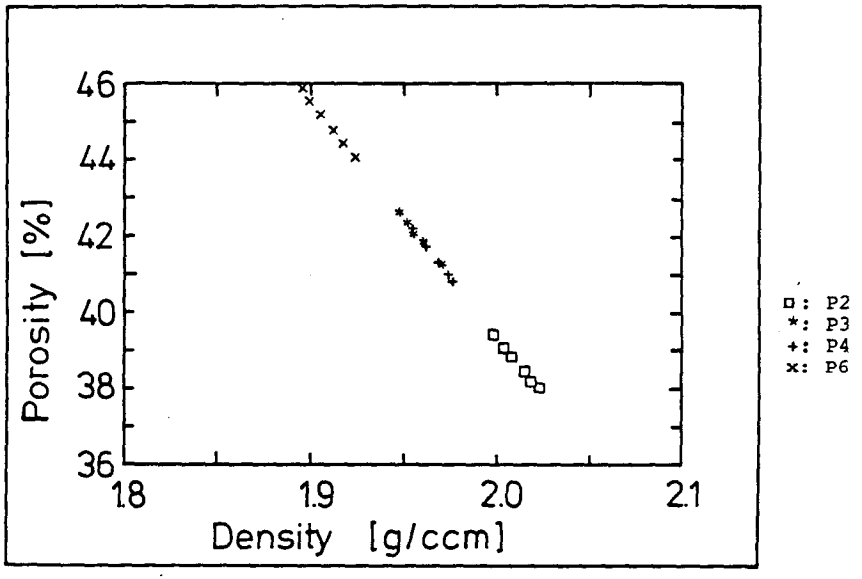

Fig. 4.9: Porosity-density relationship in coarse (P2), medium (P3, P4) and fine grained (P6) saturated samples

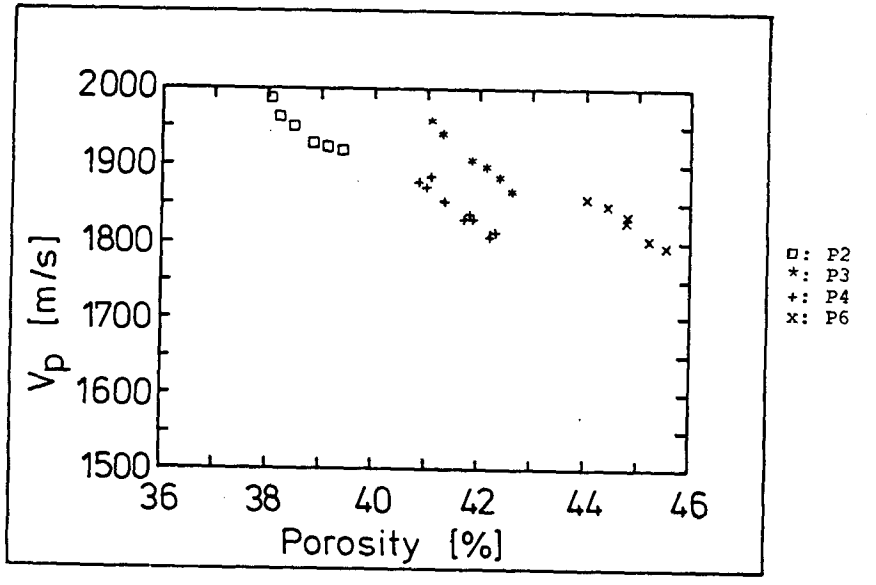

Fig. 4.10: Porosity - V_p relationship in coarse (P2), medium (P3, P4) and fine (P6) - grained saturated samples

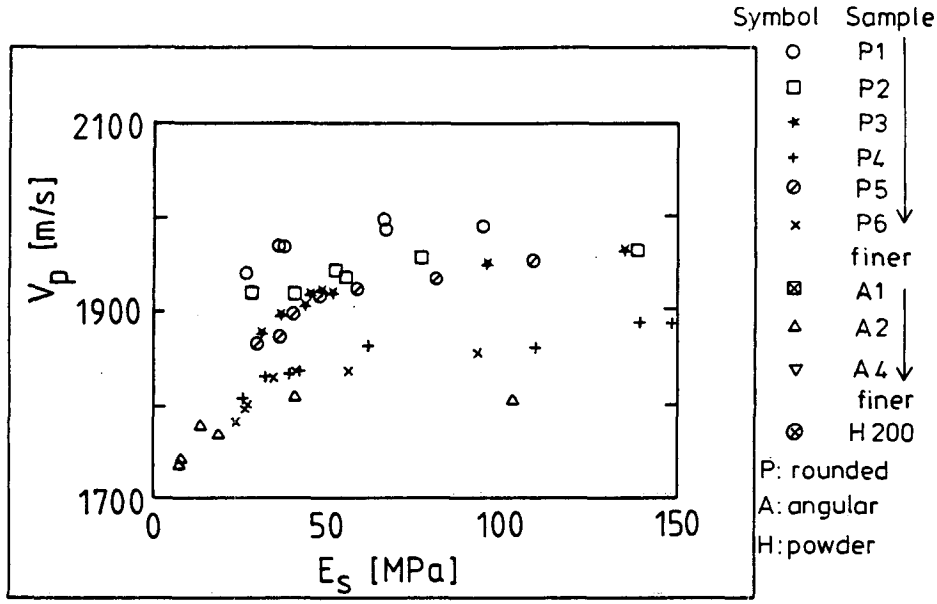

Fig. 4.11: Velocity-rigidity coefficient relationship in the samples P1...P6 and A2. At low E_s a certain relationship between E_s and V_p seems to exist.

observed. The samples can be sorted not only on the basis of their pore filling (water or air), the grain shape also seems to play a major role; the angular grains can be separated from the rounded ones. The $(V_p/V_s)^2$ - relationship is one differentiating factor. In saturated samples it is much larger (10..30), whereas dry samples are marked by low ratios ($\leq$ 10). The different damping of P- and S-waves in dry and saturated samples further separates them. In the dry grains, rounded and angular, $Q_p/Q_s < 1$, the P-waves being damped more than the S-waves. The powdered sample and the saturated samples show high Q_p.

To differentiate between bulk and shear losses, the quotient between Q_p and Q_s can be built. Taking the complex modulus M, the complex velocity is given by:

$$V^2 = (V_r + iV_i)^2 = (M/\rho) = (M_r + iM_i)/\rho \qquad (4.3)$$

This yields

$$M_r = \rho(V_r^2 - V_i^2) \quad \text{and} \quad M_i = 2\rho V_r V_i \qquad (4.4)$$

and from Eq. 4.4

$$V_r^2 = M_i^2/(2\rho V_i^2) \quad \text{and} \quad V_i^2 = M_i^2/(2\rho V_r^2) \qquad (4.5)$$

Substituting Eq. 4.5 in Eq. 4.4, we get

$$V_r^2 = \frac{M_i + [M_r^2 + M_i^2]^{0.5}}{2\rho} \qquad (4.6)$$

$$V_i^2 = \frac{M_i^2}{2\rho\,(M_r + [M_r^2 + M_i^2]^{0.5}} \qquad (4.7)$$

Taking the equation for a damped wave with frequency w :

$$u = u_0 e^{iw(t - x/V)} \quad , \qquad (4.8)$$

with t = time and X = distance, the velocity V and the attenuation coefficient α are (O'Connell and Budiansky, 1978):

$$V = (V_r^2 + V_i^2) / V_r \qquad (4.9)$$

$$\alpha = w V_i / (V_r^2 + V_i^2) \qquad (4.10)$$

$$\text{Now, } Q^{-1} = \frac{2\pi}{1 - e^{2\alpha V/f}}$$

$$\approx \alpha V/f\pi \approx 2\alpha V/w \qquad (4.11)$$

for large values of Q. Thus, substituting Eqs. 4.9 and 4.10, in Eq. 4.11, the following relations for V and Q are derived:

$$Q^{-1} = \frac{2V_i}{V_r} = \frac{2M_i}{M_r^2 + [M_r^2 + M_i^2]^{0.5}} \qquad (4.12)$$

$$V^2 = \frac{2[(M_r^2 + M_i^2) + M_r[M_r^2 + M_i^2]^{0.5}]^2}{\rho[M_r + [M_r^2 + M_i^2]^{0.5}]^3} \qquad (4.13)$$

For small values of M_i, M_i^2 can be neglected, and we derive:

$$V^2 \approx M_r / \rho \quad , \quad Q^{-1} \approx M_i / M_r \quad , \text{ and} \tag{4.14}$$

$$\frac{Q_p}{Q_s} = \frac{k_r + 4/3\ \mu_r}{\rho} \frac{\rho}{\mu_r} \frac{\mu_i}{k_i + 4/3\ \mu_i}$$

$$\approx \frac{V_p^2}{V_s^2} \frac{1}{k_i/\mu_i + 4/3} \tag{4.15}$$

With $M = k+4/3\mu$ for P-waves, and $M = \mu$ for S-waves, demarcation lines can be drawn between losses mainly in shear, $\mu_i > k_i$ and those mainly in bulk, $k_i > \mu_i$. Such lines are drawn in Fig. 4.12 for various k_i to μ_i relationships. This allows an estimation of the main mechanisms from the 'loss diagram'.

The rounded saturated samples are seen to occupy an area characterised by losses mainly in bulk ($k_i \approx 10\ \mu_i$). Increasing pressure further decreases the shear losses. The angular saturated samples possibly show higher shear losses ($k_i \approx 5\mu_i$), but this should be confirmed by more data points. In dry grains the losses are about equal in bulk and shear for both, rounded and angular, grain shapes. Only the powdered H200 shows higher losses in shear, which become about equal to those in bulk with increasing pressure. In this the powdered samples resemble clays, which are characterised by extremely high shear losses, making them almost impervious to shear waves at low pressures.

In anticipation of the discussion in Sec. 5.4, where different candidates stand to choice as additional loss mechanisms, it may be mentioned here once more, that the losses in the saturated rounded samples are mainly in bulk, and shear losses in dry samples are quite high. This is opposite to the observations of solid rocks (Winkler and Nur, 1982) and those of the earth's deep interior (Anderson and Hart, 1978), where the dominating loss factor is μ_i, Q_s^{-1} being always greater than Q_p^{-1}.

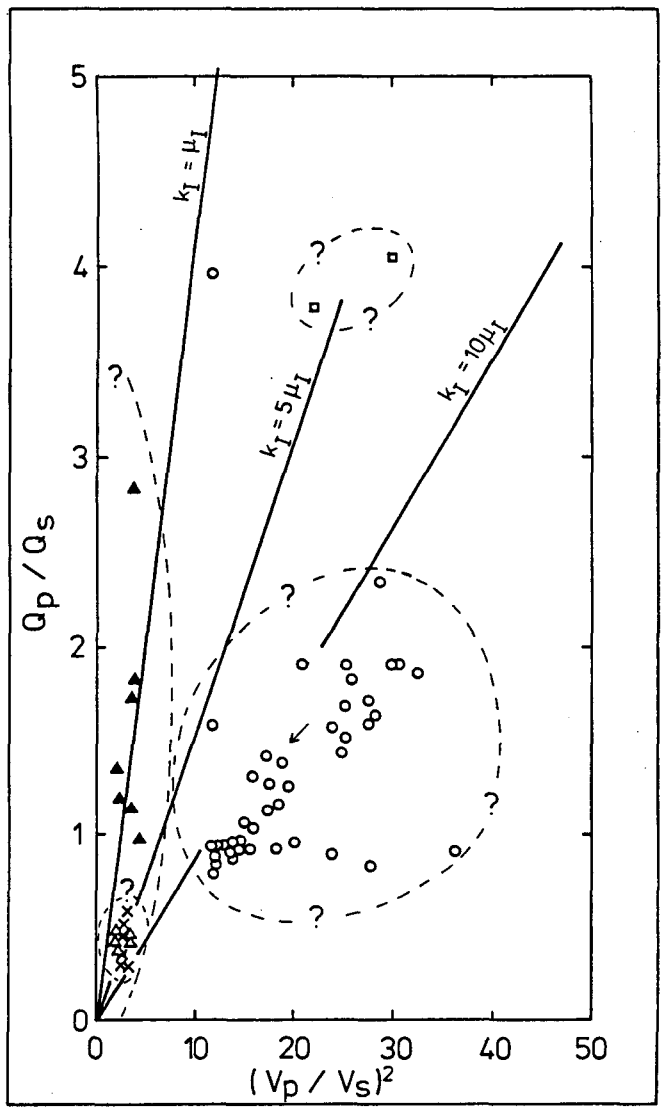

Fig. 4.12: (Q_p/Q_s) versus $(V_p/v_s)^2$ diagram. Arrows give direction of pressure decrease, broken lines delineate possible loss mechanisms for the different sediment types. Solid lines give relationship between the imaginary shear and bulk moduli (μ_i and k_i respectively).

5. Modelling of Seismic Data

The main aim of laboratory experiments is to study the effects of petrophysical parameters on seismic characteristics of the medium through which a seismic wave passes. Necessarily, it has also one objective to invert the whole problem and derive the petrophysical parameters from seismic data. This includes modelling the seismic quantities, V and Q^{-1}, with interaction of petrophysical properties. A trial and error method, but it is useful in outlining the limits of geological parameter variation and also one way of estimating the nature of the layers recorded in V and Q^{-1} changes. Modelling seismic data also gives important clues to the mechanism of wave propagation and damping. Moreover, with knowledge of petrophysical parameters in the vicinity of a borehole, the data can be laterally modelled to detect inhomogeneities.

5.1. General Introduction

There have been efforts in the past to model the seismic velocities in loose sediments and rocks. The simplest of these are empirical relations between the elastic moduli and some physical parameter. These are bound firstly to the limitations under which the relationship was set up. Secondly, as shown in Sec. 4.4, they are not unambiguous, tending to overestimate the contribution of one parameter and neglect the second.

More important is the fact, that they do not make any quantitative statement about the physical processes taking place in the sediment, which remain as much a black box as before, deforming the seismic pulse on its passage through it.

The time-average equation proposed by Wyllie et al (1956) is one such method. However, it is valid only for consolidated rocks and here too, it considers only the high pressure range, where the changes in porosity are supposed to be the main reason behind velocity changes. For smaller pressures and for unconsolidated sediments, it predicts too high velocity values. Another empirical relation is suggested by Raymer et al (1980) for ocean floor sediments. But again, this is applicable only to the high porosities encountered there, and predicts P-wave velocities which are slightly higher than that of water ($\approx$ 1500 m/s). Similarly, Wood (1930) has given V_p relationship for marine sediments and for suspensions. Han et al (1986) also studied the effect of clay on the time-average equation and applied their corrections to it.

A second method would be phenomenological, attempting to describe and quantify the mechanisms taking place in the passage of a seismic wave through a defined medium, and the effects of the petrophysical quantities on it. This method while presuming knowledge about the initial state of the medium studies the changes brought about by the physical parameters and their interactions on a seismic pulse. Obviously, the problem gets more diffuse and complicated with increasing number of interacting parameters taken into consideration.

Attempts made along this line are of two types: one considers interaction and deformation of a single porous medium; the second considers the effects of two more coupled 'elastic' media.

The Contact Radius Model (CRM), discussed in Sec. 5.2, studies the deformation of elastic spheres in contact, ie the interaction between aggregates of one medium. Here the effective moduli are related to the contact area between elastic spheres in contact.

The effects of two (or recently more) coupled elastic media, considered in Sec. 5.3 is based on the ideas put forward by Biot (1956 a,b, 1962 and 1973) in a series of classic papers. It relates the elastic and anelastic properties of a medium to the differential motion between its components.

But, extensive as it is, the Biot model has its eminent shortcomings. The most important derives from the fact, that the frame moduli are not determined by this method. It presumes knowledge about the dry medium to be able to solve for the saturated case. Also, the losses taken into account here are only those resulting from the viscous drag of the pore fluid with respect to the solid frame. The solid-solid friction, transmission defects in the frame, surface tension in both are neglected or given some arbitrary value. The presence of these is considered in Sec. 5.4, where shear losses are indeed observed in the dry samples.

Thus, in modelling the seismic properties of sediment, the Biot solution is essentially the second step, after evaluation of the elastic and anelastic frame parameters. The anelastic mechanisms leading to attenuation of seismic waves, although being subject of discussions in the past years, are not well known and understood. Values measured in nature are not only superimposed by several intrinsic mechanisms but include transmitter and receiver effects also.

However, taking source and receiver effects to be constant with time, a calibration of the system would account for these effects and for the geometric spreading factor. The attenuation in the sediment itself, and we are interested in this, is of two types:
Anelastic attenuation which is characterised by loss of elastic energy as a seismic wave propagates through a medium, the losses being converted to heat.
Elastic attenuation can be mainly thought of as scattering effects, where the elastic energy is conserved.

Both effects manifest themselves in wave amplitude decrease with distance from the source.
In the present work the scattering effects can be neglected since the wavelengths used were larger than the grain sizes: At f = 100 kHz, v = 1500 m/s, the wavelength was of the order of ≈ 15 mm. Compared to this, the maximum grain size of the samples of ≈ 0.65 mm is too small to produce scattering effects.

Mechanisms contributing to anelastic attenuation are many being controlled by various conditions such as temperature, pressure, grain size, grain shape, contact radius etc. Two of these mechanisms are considered to be principle contributors in the present case of dry and saturated sands. The two mechanisms, the solid-solid losses in the dry case and losses due to viscous drag of the fluid described by the Biot theory in the saturated case shall be examined and modelled in Sec. 5.4 to discuss a phenomenological confirmation of their presence in these investigations. The consequences of these modelling trials are debated in Sec. 5.5.

5.2 Contact Radius Modell

At its simplest, this theory considers the deformation of two elastic homogenous, identical spherical particles in contact, shown schematically in Fig. 5.1, where the radius 'b' of the area of contact increases to 'a' upon deformation of the spheres due to a normal force Y acting through their centers.

The classical theory of Hertz considers only perpendicular forces. Duffy and Mindlin (1957) and Deresiewicz (1958) extended it to shear strain arising. The main shortcomings of these models are that they do not consider the original contacts or the different packings of the spheres, tending to underestimate the elastic moduli.
Brandt (1955) modelled a random packing of spherical particles of different radii and calculated the effective

bulk modulus of a porous granular rock. Following these guidelines, Digby (1981) derived expressions for the effective bulk and shear moduli of porous granular rocks. But here, the sample considered was taken to be compacted with initial cementation bonding of the particles.

The Hertz theory considers the particles not to be bonded or connected to each other. Observations of true contacts (Johnson et al, 1971) and seismic qualities of loose sediments without pressure acting on them, shows that this cannot be the case. The particles are indeed bonded/attached to one another, by force of attraction, capillary action, their own weights, to mention a few forces. These bonds are much weaker than cementation bonds, but they should be considered all the same. In the following considerations it shall be shown that they are indeed attached to one another over an initial contact radius which must not necessarily be due to cementation.

Here, first the Contact Radius Model (CRM), as derived by Digby (1981) shall be briefly explained and then considering that similar conditions should also hold true for uncemented grains, the relation for bonded, uncemented grains with initial contact radius shall be derived.

Consider a packing of identical, solid, spherical particles which are elastic, isotropic, homogenous and bonded across small circular regions of same initial contact radius 'b'. Each sphere has same average coordination number K and radius R with shear modulus, Poissons ratio and density of grains denoted by 'μ_Q,' 'ν', and 'ρ_Q' resp. On the action of a purely hydrostatic force Y acting on them, they undergo deformation such that the contact area radius increases to 'a', Fig. 5.1, remaining circular and flat, both a and b << R. Upto this point contact forces are equal and act normal to the contact surfaces.

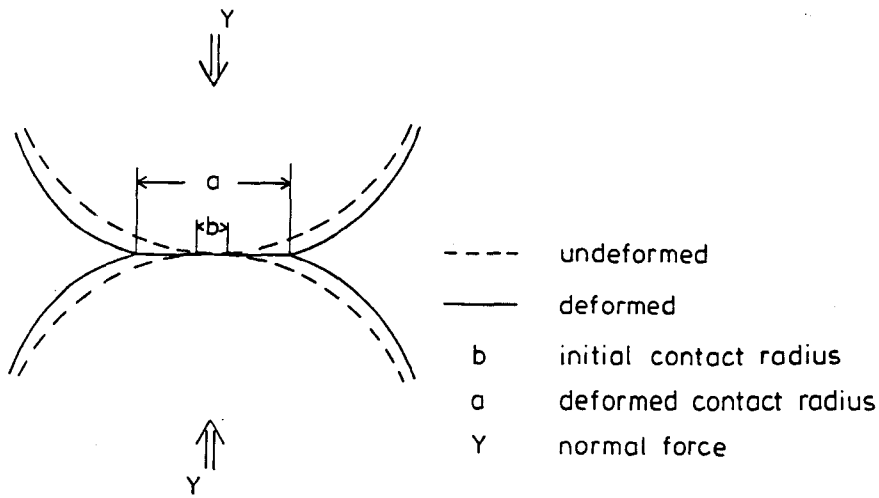

Fig. 5.1: Deformation of two spheres in contact due to a force Y

In Fig. 5.2 the area of a sphere with initial contact radius is approximated by an arc with radius of curvature R_1. There are three different regions; one lies within the initial contact radius area, the second in the vicinity of contact is described by the radius of curvature R_1 and the third by the sphere radius R.

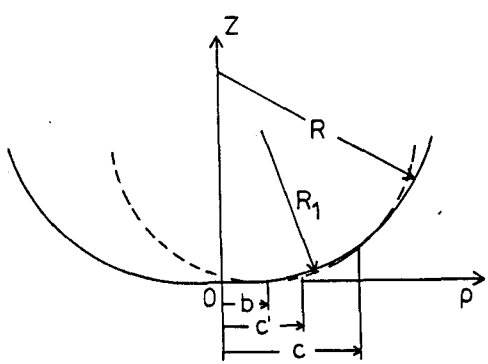

b: initial contact radius

c': intersection point between arc R and adhesion region

c: joining point between arcs R and R_1; $R > R_1$

Fig. 5.2: Cross section of the surface profile of a spherical particle before deformation, approximated by two circular arcs of radii R and R_1, from Digby (1981)

On the basis of this deformation, Digby (1981) derived expressions for the relative approach of the centers of two spheres, 2δ, due to a normal force Y acting through the centers of each sphere. The resultant force acting on an arbitrary area A due to uniform stress increments δp_{ij} is compensated by the resultant contact force on the set of spheres therein. These contact forces are related to the displacement of the bonded spheres.

The normal force Y and the displacement δ due to it are given by Digby as

$$\delta = a \left(a^2 - b^2 \right)^{0.5} / R \qquad (5.1)$$

$$Y = \frac{4\mu_Q}{1-\nu} \left[a\delta - \frac{(a^2-b^2)^{1.5}}{3R} \right] \qquad (5.2)$$

where
- b = initial contact radius
- a = deformed contact radius
- μ_Q = shear modulus of grains
- R_Q = grain size
- Φ = porosity
- ν = poissons ratio

Considering this normal force to be due to hydrostatic pressure P:

$$Y = \frac{4\pi R^2 P}{(1-\Phi)K} \qquad K = \text{coordination number} \qquad (5.3)$$

Now this expression for the force acting on the spheres is only due to the external pressure. But, there are also surface effects acting on the grains, which manifest themselves in an apparent cohesion. This cohesion seen for example in shear tests on sands in Fig. 3.8 could be due to the capillary forces acting between the grains. This observation has also been reported by Johnson et al (1971), who theoretically determined the adhesive forces acting across contact boundaries. They relate the strength of adhesion to surface energy of the elastic bodies through the action of surface forces. It has been observed that contact

areas for smooth rubber (Roberts, 1968) and glass spheres (Kendall, 1969) at small loads are indeed much larger than those predicted by the Hertz-model and at reduction of the load Y to zero, they tend towards some finite value. At zero applied load, the contact area is finite and is given by:

$$a^3 = R^*(6\gamma\pi R)/K_E; \quad K_E = (1-\nu)/\pi E; \tag{5.4}$$

E: dynamic Young's modulus

This is in accordance with the observations of the shear tests, and proves that loose grains are indeed held together over small areas by adhesive forces. Also separation of the spheres does not occur at Y = 0, but at some negative load :

$$Y^* = -3/2\gamma\pi R \tag{5.5}$$

The change in load due to this surface energy (γ) effect is given by Johnson et al (1971) as:

$$Y^* = Y + 3\gamma\pi R + \sqrt{\{6\gamma\pi RY + (3\gamma\pi R)^2\}} \tag{5.6}$$

which is obviously larger than the externally applied load Y. Fig. 5.3 shows results for rubber spheres in dry and lubricated contacts compared with the modified theory and the old Hertz model. The modified theory fits the experimental data, whereas the Hertz model predicts too low contact areas. Also, dry contacts have higher surface energy than those immersed in water. Observations after immersion in a Sodium Dodecyl Sulphate (SDS) solution, which does not wet the rubber, agree with the Hertz model. Same spheres at positive and negative loads are seen in Fig. 5.4. Again it is observed that the contacts do not result as an effect of the externally applied load only; a negative load is required to separate the grains.

Thus, the force acting on the grains was extended as in Eq. 5.6. With this modified force, the deformed contact radius can be explicitly calculated from the cubic equation obtained from Eqs. 5.1 and 5.2.

$$Y^*3R(1-\nu)/4\mu = \{3a^2(a^2-b^2)^{0.5} - (a^2-b^2)^{1.5}\} \tag{5.7}$$

or,

$$4a^6 - 3a^2b^4 - b^6 - F^2 = 0 \quad , \text{where} \tag{5.8}$$

$$F = 3Y^*R(1-\nu)/4\mu_Q \tag{5.9}$$

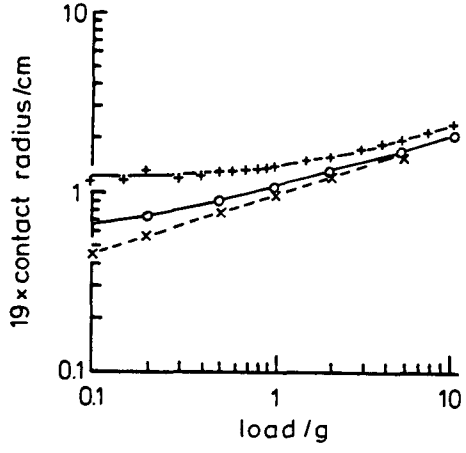

Fig. 5.3: Results for two rubber spheres (R_1=R_2=2.2cm) in dry and lubricated contact. +, Dry contact; O, water contact; x, SDS solution contact; ---, Hertz theory; —— modified theory. SDS solution is a 0.1 molar sodium dodecyl sulphate solution which sets down the surface energy of the contacts which then obey the Hertz theory. From Johnson et al (1971)

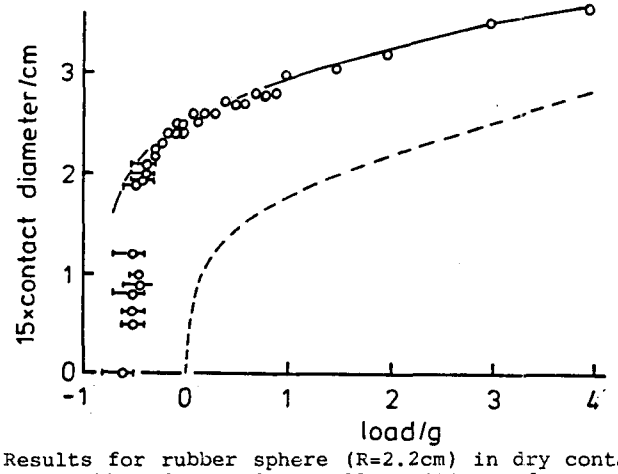

Fig. 5.4: Results for rubber sphere (R=2.2cm) in dry contact with rubber flat under small positive and negative loads. O, Contact results; ---, Hertz theory; ——, modified theory. True contacts are observed to be larger than those predicted by the Hertz theory (dashed lines) and pressure is required to separate them. From Johnson et al (1971)

Calculations carried out for different grain sizes and different initial contact radii (Fig. 5.5 a-d, a finest, d coarsest) show distinctly following results.

- At small pressures, there is an abrupt increase in the contact radius. This increase is much larger for coarser grains (Fig. 5.5d).

- The increase in contact radius tends towards a certain limiting value. Once this is reached, there is almost no change with pressure. This limiting contact radius is arrived at much lower confining pressures for finer grains (Fig. 5.5a).

The significance of this is seen in the similarity between contact radius increase in Fig. 5.5 and Q_s^{-1} decrease with pressure in Fig. 4.2, top. The increase in contact radius (Fig. 5.5d) and decrease in Q_s^{-1} for coarser grains (Fig. 4.2, samples P1 and P2) is much higher at lower pressures. Finer grains do not show much change in contact radius (Fig. 5.5a) and in S-wave attenuation with pressure (Fig. 4.2, samples P5 and P6). If the attenuation of unconsolidated sediments is considered to be due to the loose packing of the grains and relative motion between them, the seismic energy being lost in friction, the attenuation characteristics of different grain sizes could be explained on the basis of their distinct contact radius changes. An increase in pressure leads to an increase in contact radius, a denser packing and with it higher shear strength. The stable packing of the finer grains due to their own weights prevents any predominant relative motion between grains and so attenuation change with pressure is not so pronounced, as opposed to the coarser grains which show considerable displacement and readjustment with pressure.
In Sec. 5.4 the attenuation shall be derived as a function of the contact area of dry spheres. Now taking the stress-strain relations,

$$2\mu^* = \delta p_{3r}/\delta e_{3r} \qquad (5.10)$$

$$\lambda^* = \delta p_{33}/\delta e_{kk} - \delta p_{3r}\delta e_{33}/\delta e_{3r} \qquad (5.11)$$

the normal and tangential stiffnesses, as derived by Mindlin (1949),

$$dT/ds = 4\mu_Q a/(2-\nu)\ , \quad dY/ds = 2\mu_Q a/(1-\nu) \qquad (5.12, 13)$$

instead of

$$dT/ds = 8\mu_Q b/(2-\nu)\ , \quad dY/ds = 4\mu_Q a/(1-\nu) \qquad (5.14, 15)$$

from Digby (1981)

with the tangential stiffness modified to

$$dT/ds = 4\mu_Q b/(2-\nu) \qquad (5.16)$$

since as shown before, even in loose grains there exists an initial contact radius, the force equilibrium equation of Digby (1981) can be rewritten to get explicit expressions for the effective frame moduli:

$$\mu^* = \frac{\mu_Q K(1-\Phi)}{5\pi R}\left[\frac{a}{1-\nu} + \frac{3b}{2-\nu}\right] \qquad (5.17)$$

$$\lambda^* = \frac{\mu_Q K(1-\Phi)}{5\pi R}\left[\frac{a}{2(1-\nu)} - \frac{b}{2-\nu}\right] \qquad (5.18)$$

$$K^* = \frac{\mu_Q K(1-\Phi)}{5\pi R}\left[\frac{5a}{6(1-\nu)}\right] \qquad (5.19)$$

Interestingly, the bulk modulus is independent of the initial contact radius, whereas the shear modulus is much affected by the initial contact radius. These effective frame moduli can be used to model the measured P- and S-wave velocities by varying the initial contact radius b. In Figs. 5.6 and 5.7 the best fit to the measured V_p and V_s are plotted with respect of differential pressure for a fine and a coarse grained sample respectively. The calculations were carried out with Φ- and P_d-values from the P.T. experiments. Other physical parameters used are given in Table 5.1. The good fit between theory and experiment shows the relevance of the theory in understanding the phenomena effective in the sediments. Moreover these effective frame moduli can be used to

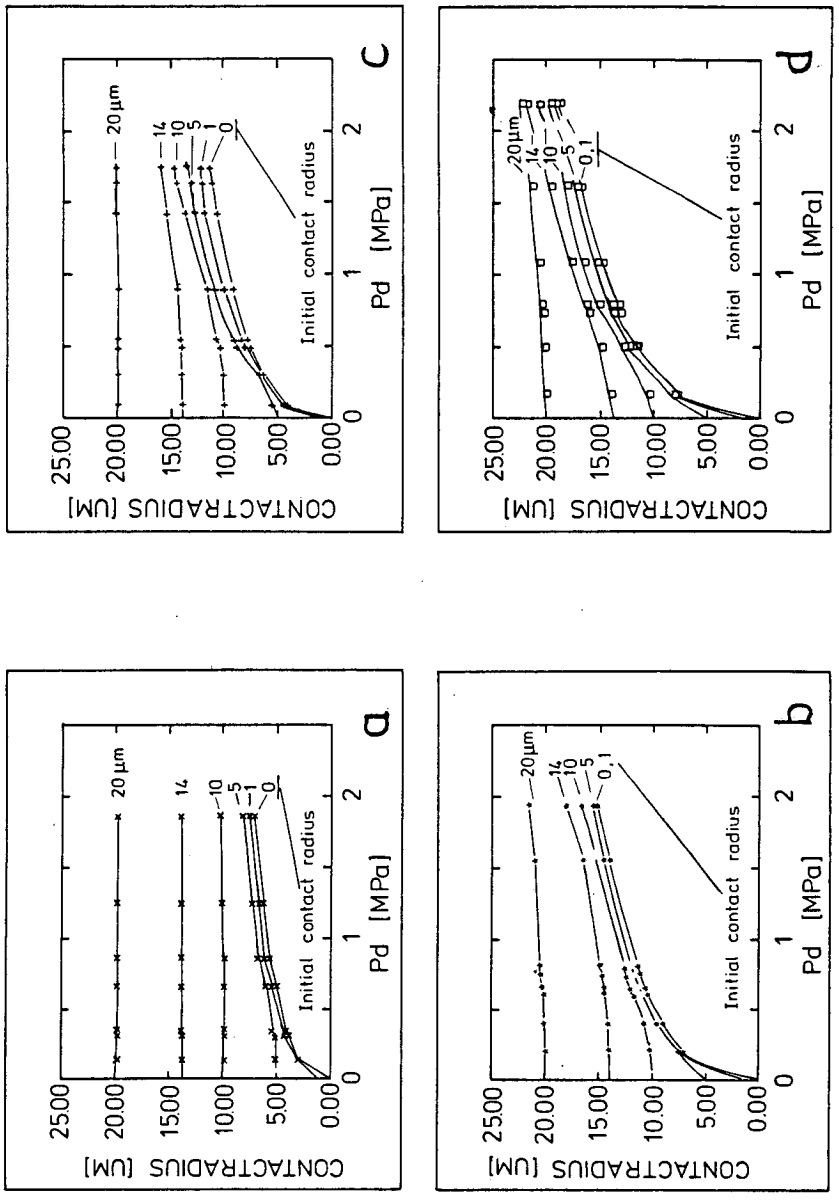

Fig. 5.5: Change in the contact radius with pressure for different grain sizes; a=110µm, b=150µm, c=225µm, d=275µm. The different curves in each figure are calculated with different initial contact radii denoted by numbers on the curves.

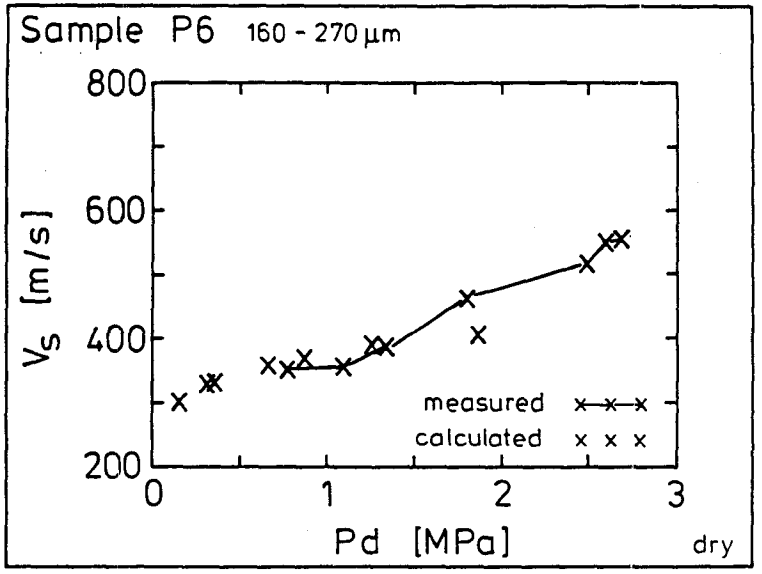

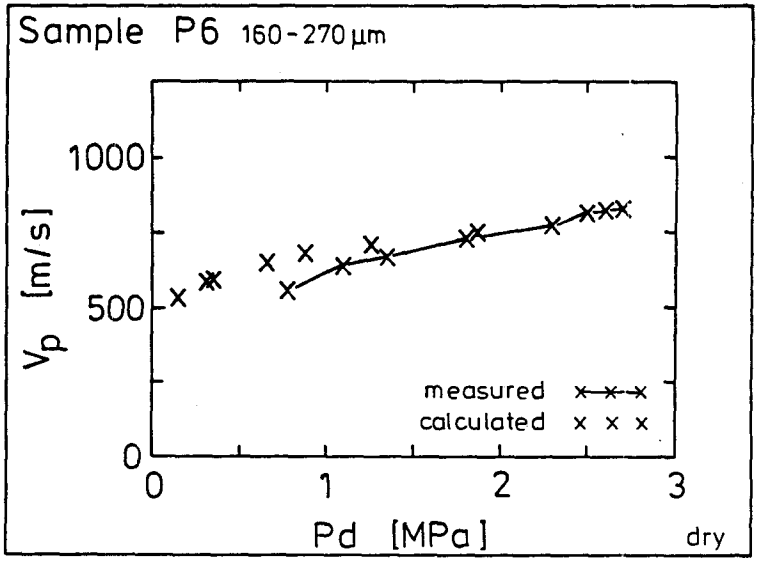

Fig. 5.6: V_p (bottom) and V_s (top) measured and calculated with the CRM for the fine grained sample P6

model the velocities for saturated sediments. Thus, valuable knowledge about the physical parameters recorded in V_p and V_s is gained.

The values obtained for 'b' by trial and error to match the dry velocities are more or less same as those obtained by Eqn. 5.4.

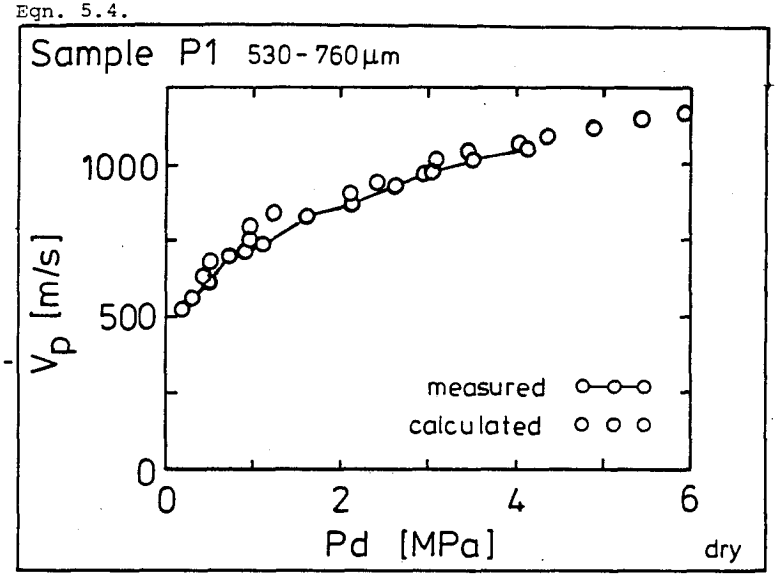

Fig. 5.7: V_p measured and calculated with the CRM for the coarse grained sample P1

5.3 Biot Model

The Biot model describes the propagation of elastic waves in a two phase system, a porous elastic frame and a viscous, compressible pore fluid contained in it.

The stress-strain relations for each component are derived separately. Since, in a coupled porous system, there is differential motion between the two components, forces are built up in the pores due to the drag of the viscous fluid.

In ideal coupling there will be no relative motion between the two, no coupling requires different sets of equations of motion for each phase. The cases encountered in nature lie between these two extremes, with a thin film of the liquid, depending on its wettability, responding in phase with the frame. This differential motion is described by the Darcy Law of flow through a porous medium. Combining the stress-strain relations with the Darcy Law for the fluid flow losses in the pore fluid gives the equations of motion governing the propagation of dilatational and shear waves. These, in their notation of Stoll (1974, 1977, 1979 and 1980) are

$$\nabla^2(He-C\epsilon) = \partial^2(\rho e-\rho_f\epsilon)/\partial t^2 \qquad (5.20)$$

$$\nabla^2(Ce-M\epsilon) = \partial^2(\rho_f e-m\epsilon)/\partial t^2 - \eta/k_f^*\partial\epsilon/\partial t \qquad (5.21)$$

for P-waves, and for S-waves:

$$\mu^*\nabla^2 w = \partial^2(\rho w-\rho_f\theta)/\partial t^2 \qquad (5.22)$$

$$0 = \partial^2(\rho_f w-m\theta)/\partial t^2 - \eta/k_f^*\partial\theta/\partial t \qquad (5.23)$$

where

$$H = \frac{(K_s - K_b)^2}{D - K_b} + K_b + \frac{4}{3}\mu^* \qquad (5.24)$$

$$C = \frac{K_s(K_s - K_b)}{D - K_b} \qquad (5.25)$$

$$M = K_s^2 / (D-K_b) \qquad (5.26)$$

$$D = K_r(1 + \Phi(K_s/K_{f-1})) \qquad (5.27)$$

e = div u — ϵ = Φ div (u-U)

w = curl u — θ = Φ curl (u-U)

U = displacement of pore fluid — u = displacement of frame

ρ_f = density of pore fluid — ∇ = Laplace operator

ρ = composite density — Φ = porosity

η = viscosity of pore fluid — k_f = permeability

m = $\alpha\rho_f/\Phi$ — μ^* = shear modulus

K_s = bulk modulus of grains — K_b = bulk modulus of frame

K_f = bulk modulus of pore fluid

α = structure constant = 3 for a system of uniform pressure with all possible orientations

The parameter m accounts for the shape and orientation of the pore spaces. The breakdown of Poiseuille flow occurs at higher frequencies. The frequency dependent viscous resistance to fluid flow (η/k) is no longer a constant. The critical frequency f_c beyond which Poiseuille flow breaks down is given by Biot as:

$$f_c = m\eta/4d^2\rho_f \qquad (5.28)$$

where d = diameters of the pores

The frequency of measurement would limit the pore diameters to $\approx$ 5 μm only. Thus for the present consideration, the complex frequency dependant viscosity correction factor $F\eta$ suggested by Biot must be applied instead of η.

$$F(k) = \frac{1}{4} * \frac{kT(k)}{1 - \frac{2T(k)}{ik}} \qquad \text{and} \qquad (5.29)$$

$$T(k) = \frac{ber'(k) + ibei'(k)}{ber(k) + ibei(k)} \qquad (5.30)$$

$$k = a(\omega\rho_f/\eta)^{0.5} \qquad (5.31)$$

Here ω: frequency

a: pore size parameter $\approx$ d/7 (Stoll, 1974)

d: grain diameter

ber(k), bei(k), ber'(k), bei'(k): real and imaginary parts of the Kelvin functions (Abramowitz and Stegun, 1972)

Thus the equations of motion change to

$$\nabla^2(He - C\epsilon) = \partial^2(\rho e - \rho_f\epsilon)/\partial t^2 \qquad \text{for P-waves} \qquad (5.32)$$

$$\nabla^2(Ce - M\epsilon) = \partial^2(\rho_f e - m\epsilon)/\partial t^2 - \eta F(k)/k * \partial\epsilon/\partial t \qquad (5.33)$$

and,

$$\mu^*\nabla^2 w = \partial^2(\rho w - \rho_f\theta)/\partial t^2 \qquad (5.34)$$

$$0 = \partial^2(\rho_f w - m\theta)/\partial t^2 - \eta F(k)/k * \partial\theta/\partial t \qquad (5.35)$$

The solutions of these equations, which deliver two kinds of P- and one type of S-wave were now modelled, using the frame parameters as determined from the contact radius model, the attenuation being only on account of the relative motion

between the frame and its pore fluid. Of the two types of P-waves obtained by modelling, attention is devoted to the P-wave of 'first type'. The 'second-type'-P-wave (Biot, 1956 a, b) a sort of diffusion wave is very much damped at the frequency of measurement with $V_p \approx 200...300$ m/s.

Values of physical properties used in the numerical computations are in Table 5.1.

μ_Q	=	36.5	GPa
K_f	=	2.22	GPa
K_Q	=	51.2	GPa
ρ_f	=	997.1	kg/m^3
ρ_Q	=	2650	kg/m^3
K	=	9	
η	=	0.001	kg/ms

Table 5.1

k^*, μ^* from the CRM

w, Φ, k_f from experiments

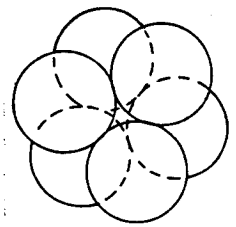

cartoon of grains with a coordination number K = 9

The velocity results thus obtained are given in Fig. 5.8 for grain radius 110 µm, and in Fig. 5.9 for grain radius 275 µm. Whereas attention is directed here to the attenuation results, only a comment that V_s (calculated) more or less matches and V_p (calculated) is less than the measured values, should suffice. They shall be discussed at length later in this chapter. The results obtained for Q_p^{-1} and Q_s^{-1} are plotted versus frequency in Fig. 5.10 for a grain radius of 110 µm and in Fig. 5.11 for grain radius 275 µm. Each line in the plots corresponds to a different differential pressure. The attenuation peaks for both samples are at slightly higher frequencies than those calculated by Meißner and Theilen (1983) for similar samples. But, the position of the attenuation peak being very sensitive to permeability, a slightly higher permeability assumed by them would shift the peak calculated with it to lower frequencies. In coarser grains, Q_p^{-1} at different pressures (Fig. 5.11, bottom) gets closer with higher frequencies, it even increases with

pressure beyond a certain frequency. At the frequency of measurement, indicated by arrow in the figures, it shows an increase in Q_p^{-1} with pressure. This corresponds with the experimental results, where Q_p^{-1} in coarser grains increases with pressure. In finer grains (Fig. 5.10, bottom) the attenuation peak is shifted to higher frequencies. Here too, Q_p^{-1} at different pressures gets closer at higher frequencies, but at the frequency of measurement, also indicated by an arrow, it does not show an increase with pressure. This too agrees with the observation, namely, Q_p^{-1} in finer grains remains more or less constant with pressure.

Two 'side-effects' of the modelling, however, pose discrepancies to the observations. First, Q_p^{-1} in finer grains is higher than in coarser grains at the frequency of measurement. The observation prove to be opposite of this. Second, comparing Q_s^{-1} modelling results with the observations posses another problem. Laboratory experiments show Q_s^{-1} to be higher and the gradient for decrease in Q_s^{-1} to be larger in coarser grains than in finer grains. But the attenuation modelling yields results with similar characteristics as those seen in Q_p^{-1}, with Q_s^{-1} in fine grains (Fig. 5.10, top) showing a small decrease with pressure, and in coarse grains (Fig. 5.11, bottom) an increase with pressure at the frequency of measurement, remember arrow. Also Q_s^{-1} in the finer grained sample is higher than in the coarser one at that frequency.

Thus fluid flow losses are not enough to explain the experimental observations. Certainly, additional losses are occurring in the sediments which should be considered too.

5.4. Friction

Friction at small strains (10^{-5}) as one possible mechanism leading to attenuation of seismic waves has been practically

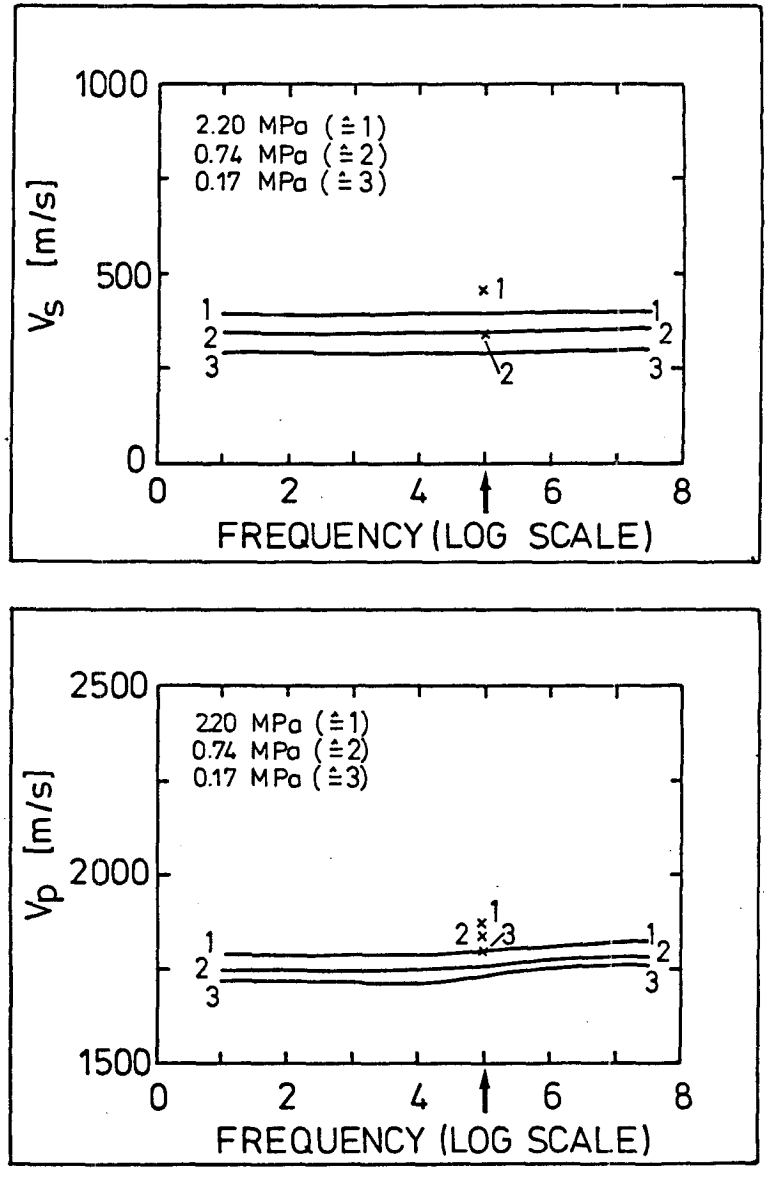

Fig. 5.8: $V_p(\omega)$ (bottom) and $V_s(\omega)$ (top) calculated with the CRM-Biot Model for a grain radius = 110 µm (≙ sample P6) at three different pressure steps. Symbols mark measured values in the corresponding sample P6. Frequency of measurement is indicated by the arrow.

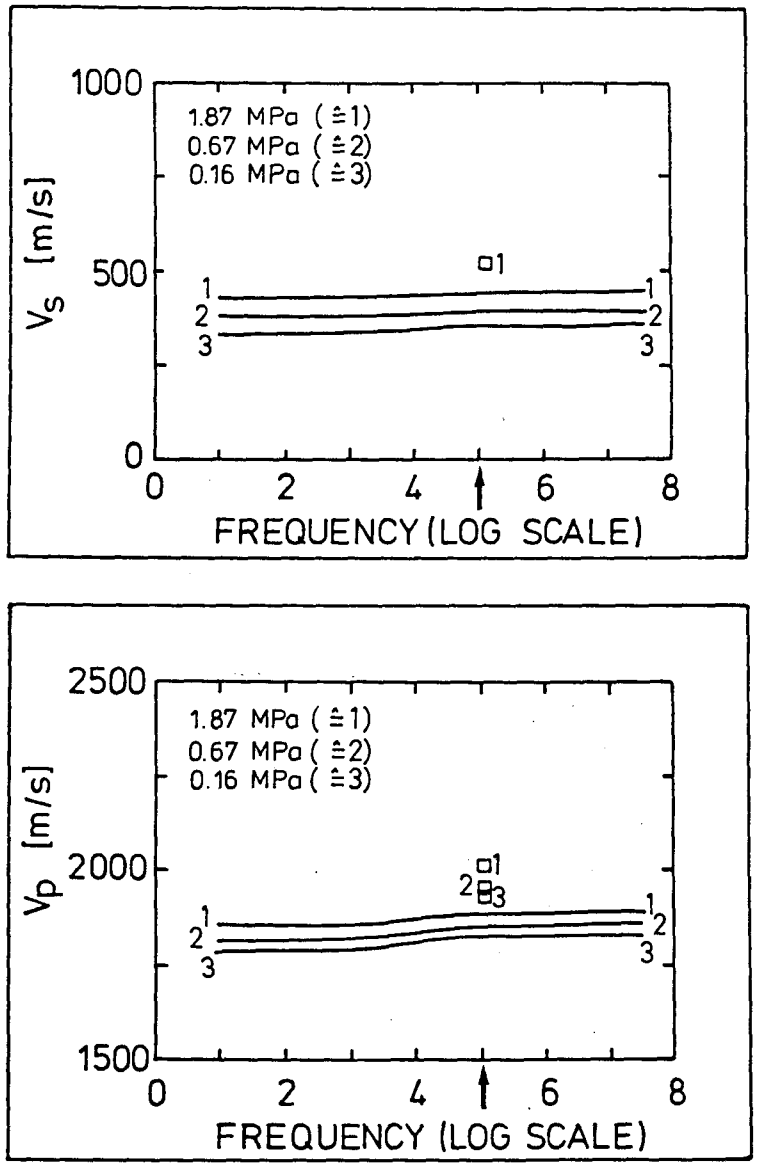

Fig. 5.9: $V_p(w)$ (bottom) and $V_s(w)$ (top) calculated with the CRM-Biot Model for a grain radius = 275 µm (≙ sample P2) at three different pressure steps. Symbols mark measured values in the corresponding sample P2. Frequency of measurement is indicated by the arrow.

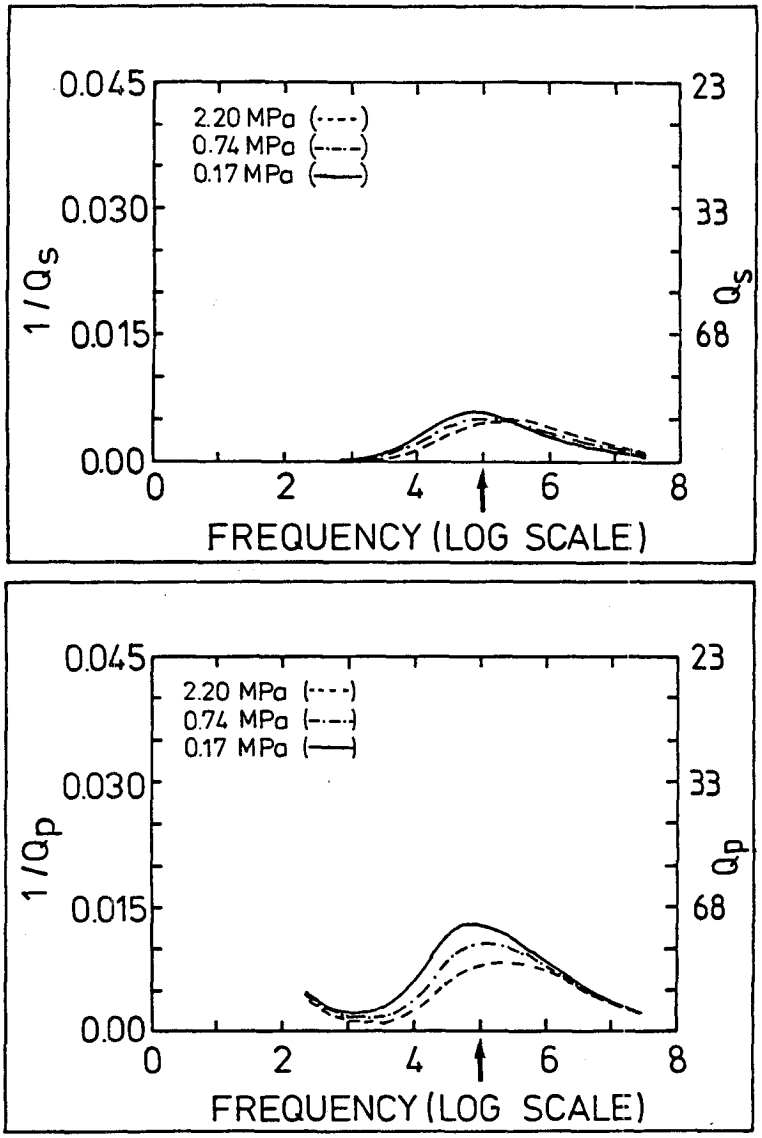

Fig. 5.10: $Q_p^{-1}(w)$ (bottom) and $Q_s^{-1}(w)$ (top) calculated with the CRM-Biot Model for a grain radius = 110 µm (≙ sample P6) at three different pressure steps. At the frequency of measurement, indicated by the arrow, both Q_p^{-1} and Q_s^{-1} show a decrease with pressure.

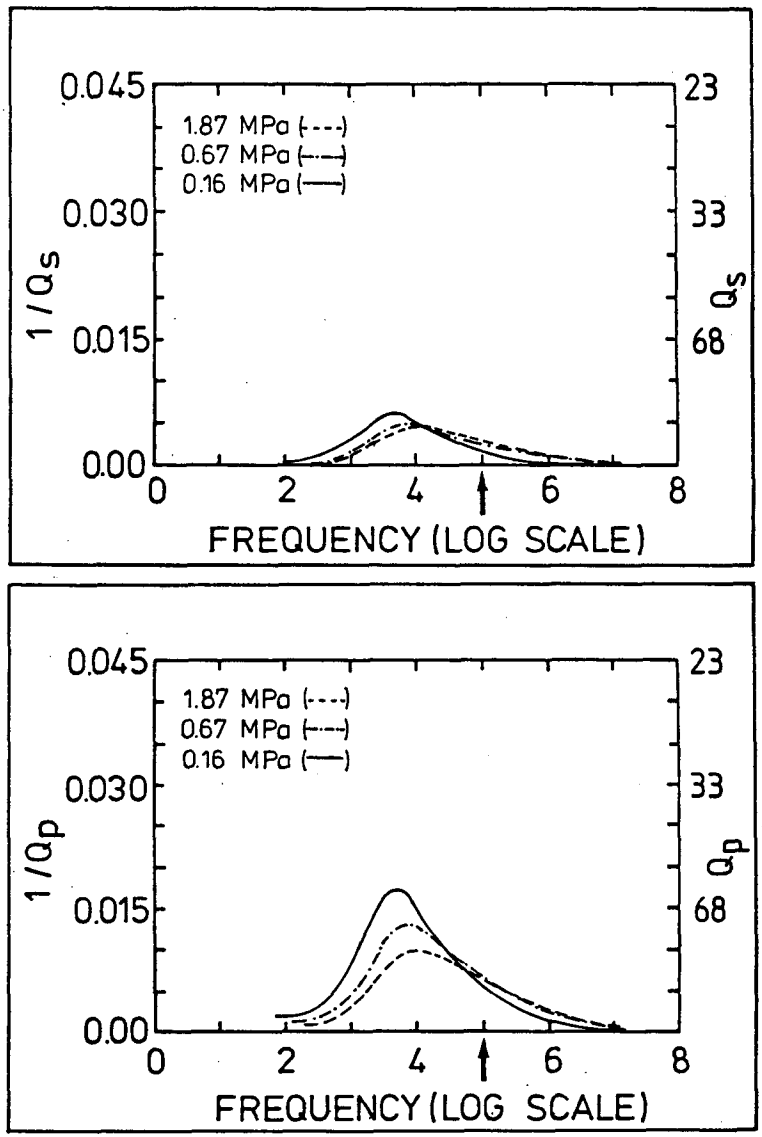

Fig. 5.11: $Q_p^{-1}(w)$ (bottom) and $Q_s^{-1}(w)$ (top) calculated with the CRM-Biot Model for a grain radius = 275 μm (≙ sample P2) at three different pressure steps. At the frequency of measurement, indicated by the arrow, both Q_p^{-1} and Q_s^{-1} show an increase with pressure.

ruled out by various authors (Stewart et al, 1983; Winkler and Nur, 1982). Though this might be true of consolidated rocks as they are effectively held together not only by the frictional force but also by cementation, thus requiring higher shear stresses to cause frictional losses, it must not hold true for an consolidated loose packing of dry sands or sediments. Further, the sands are not really dry but have an absorbed water molecule layer on their boundaries. As works of Johnson et al (1971) have shown, this considerably sets down the total surface energy of the grains (Fig. 5.4), lowering with it the cchesive force active across grain boundaries against any shear traction.

Here, it will be shown to what extent we might expect such effects under the prevailing conditions. At first an approximation will be made to calculate the frictional and shear forces acting on each grain. The work lost at the contacts compared with the total work done will then give the attenuation due to friction.

A hydrostatic pressure P acting on the sample gives rise to a normal force Y acting across the centers of the grains, holding them together. Taking an arbitrary area A:

$$Y = P^*A \tag{5.36}$$

As derived in the Sec. 5.1.2 this force is augmented by surface energy conditions. Y^* is taken from Eq. 5.6 as:

$$Y^* = Y + 6\pi R\gamma + \sqrt{(12\pi R\gamma Y + (6\pi R\gamma)^2)} \tag{5.37}$$

Now this normal force Y acts against any shear force tending to shear the grains across each other.

Relating the effects of this force Y and the shear strain ϵ_s due to the transducers on the same arbitrary area A, the frictional losses due to the latter can be estimated.

Considering an arbitrary unit area A, first the number of contacts in it shall be estimated and, with it, the total area of contact.

If the number of spheres in unit bulk volume is

$$3(1-\Phi)/4\pi R^3, \tag{5.38}$$

then the number of spheres cut by a unit area A at an angle $\geq 2\Theta$ = $3(1-\Phi)(1-\cos\Theta)/4\pi R^2$. (5.39)

The number of contacts per unit solid angle being $K/4\pi$, these in θ, are $K\theta/4\pi$. (5.40)

Thus the total number of contacts $n(\theta)$ in area of spheres cut at an angle $\geq \theta = 3(1-\Phi)(1+\cos\theta)K\theta/2(4\pi R)^2$. (5.41)

Taking the total number of spheres cut between θ and π

$$n(\theta) = \int_0^{\pi} 3(1-\Phi)(1+\cos\theta)K\theta/2(4\pi R)^2 d\theta =$$
$$= 3K(1-\Phi)(0.5\pi^2-2)/2(4\pi R)^2. \quad (5.42)$$

With the area of one contact as πb^2, the total area of contact on area A:

$$A_C = 3Kb^2(1-\Phi)(0.5\pi^2-2)/32\pi R^2. \quad (5.43)$$

The normal force Y^* due to hydrostatic pressure P and surface tension effects acting on this area A_c:

$$Y^* = 3Kb^2(1-\Phi)(0.5\pi^2-2)P/32\pi R^2. \quad (5.44)$$

Related to this normal force, the frictional force F prevailing at each contact area is:

$$F = Y^* * f_0 , \quad (5.45)$$

with f_0 = coefficient of contact friction

This frictional force is juxtaposed to shear forces prevailing at the contacts due to the transducers.

Following the line of Digby (1981), the effect of shear force acting on the total area of contact of the spheres present in the different angles of intersection with the area is:

$$A\delta p = \sum_{\theta} \frac{K\mu^* bRn(\theta)\sin^2\theta}{(2-\nu)} \delta e_{3r}(2-\sin^2\theta) +$$
$$+ \sum_{\theta} \frac{K\mu^* aRn(\theta)\sin^4\theta}{4(1-\nu)} \delta e_{3r} \quad (5.46)$$

If we designate $A\delta p_{3r}$, r=1,2 as the shear force T_s,

$$T_s = \left[\sum_{\theta} \frac{K\mu^* bRn(\theta)\sin^2\theta}{2-\nu} - \sum_{\theta} \frac{K\mu^* bRn(\theta)\sin^4\theta}{2(2-\nu)} + \right.$$

$$\left. + \sum_{\theta} \frac{K\mu^* aRn(\theta)\sin^4\theta}{4(1-\nu)} \right] \delta e_{3r}$$

with $n(\theta)$ as derived earlier,

$$= \left[\frac{K\mu^* bRA_c(1-\Phi)}{(2-\nu)\pi R^2} - \frac{K\mu^* R4A_c(1-\Phi)}{10(2-\nu)\pi R^2} + \frac{K\mu^* aR4A_c(1-\Phi)}{20(1-\nu)\pi R^2} \right] \delta e_{3r} =$$

$$= \frac{K\mu^*(1-\Phi)}{5\pi R^2} \left[\frac{3b}{2-\nu} + \frac{a}{1-\nu} \right] A_c \delta e_{3r} \qquad (5.47)$$

The shear force acting on an arbitrary area A due to the strain δe_{3r} can be given as

$$T_s = \frac{K\mu^*(1-\Phi)}{5\pi R^2} \left[\frac{3b}{2-\nu} + \frac{a}{1-\nu} \right] A_c \delta e_{3r} \qquad (5.48)$$

Putting the two, normal and shear, forces in relation gives the losses at the contacts. Note that T_s must be smaller than F_s, else the grains tend to shear across each other. According to Mindlin and Deresiewicz (1953), frictional energy loss per cycle is in the case of a normal force Y^* (here due to P_d) and an oscillating tangential force T_s which is smaller than the frictional force can be given by

$$\Delta W = (2-\nu)T_s^3 \,/\, 36\mu_Q afN, \qquad (5.49)$$

for one contact area on the annules.

$$\text{The work loss } (\Delta W_t) = \frac{(2-\nu)T_s^3}{36\mu_Q afY^*} * \frac{3K}{4\pi R^3} \tag{5.50}$$

(Stewart et al, 1983).
Summing up for a large volume V_L, the total loss

$$\Delta W = \frac{(2-\nu)T_s^3}{36\mu_Q afY^*} * \frac{3K}{4\pi R^3} * V_L \tag{5.51}$$

Total work W_L done in Volume V_L

$$W_L = 0.5 V_L \mu^{*2} \epsilon^2 \tag{5.52}$$

By definition:

$$Q^{-1} = \Delta W / 2\pi W_L$$

$$= \frac{(2-\nu)T_s^3}{36\mu_Q afY^*} * \frac{3K}{4\pi R^3} * \frac{V_L}{\pi V_L \mu^{*2} \epsilon^2}$$

$$= \frac{(2-\nu)K}{48\mu_Q \pi^2} * \frac{T_s^3}{afY^* \mu^* \epsilon^2 R^3}$$

$$= \frac{(2-\nu)K^4}{6000\pi^4 \mu_Q R^6} * \frac{\mu^* 2(1-\Phi)^3 A^2 \epsilon}{afP} \left[\frac{3b}{(2-\nu)} + \frac{a}{(1-\nu)}\right]^3 \tag{5.53}$$

Thus the shear loss due to friction is very much dependent on the grain size parameters R, b and a.
Taking the maximum shear strain ϵ expected in the present case as $\pm 4.0*10^{-5}$ (Muckelmann, 1985), calculations were carried out for different grain sizes. It should be borne in mind, that this value of the shear strain due to the transducers is, at best, a rough estimate. The actual strain effective in the medium can be much higher or lower depending on the grain arrangement.

In Fig. 5.12 calculations are presented for different grain sizes 315, 275, 225, 175, 150 and 110 [µm]. The results are conspicuous in two senses. First, they show that at strains around $\pm 10^{-5}$ the attenuation due to friction can be considerably large. Secondly, this attenuation is the largest for coarse grain and decreases here very rapidly with pressure. In finer grains the attenuation decreases only slightly with pressure remaining more or less at the same low level.
Thus for finer grained sediments the strain must be reduced to below 10^{-6} and even less for coarse grained samples. This in turn implies that at seismic sources these effects would also be effective.

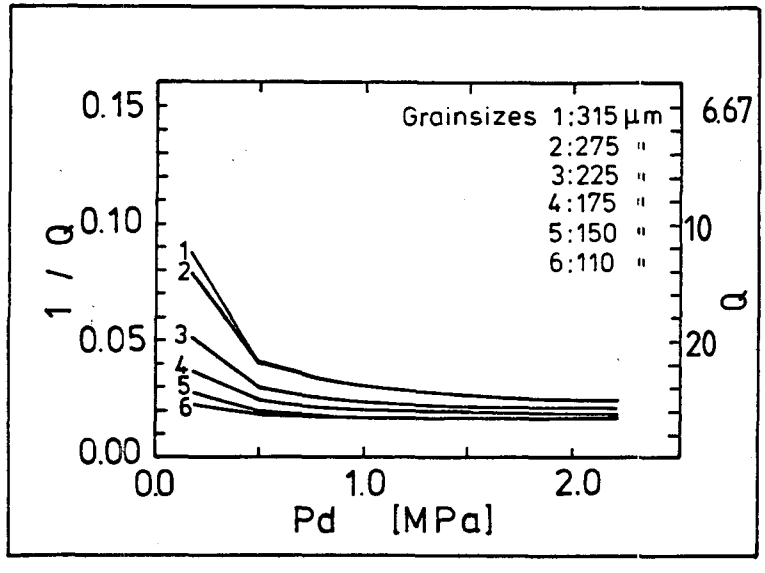

Fig. 5.12: Calculation of losses due to friction for differential grain sizes. The coarser grains have higher values and steeper gradients of decrease with pressure.

5.5 Application of a Combined Model

The methods of modelling seismic properties described above were now applied to different data sets.

First the dry velocity was modelled with the CRM, which delivered the frame moduli. Using these frame moduli the saturated case was modelled with the Biot theory with corrections, if required, for the frictional losses.

5.5.1 On Glass Beads

Primarily, the simplest case was taken; V_p and V_s in dry and saturated glass beads measured at different pressures from Domenico (1977). The measured data is shown in Fig 5.13.

The velocities for the dry samples were modelled with different grain sizes, whereby porosity and initial contact radii were changed arbitrarily. The data used for this modelling is given in Table 5.1. This allowed a first sorting of the possible parameters. Figs. 5.14 and 5.15 illustrate these trials. Despite the ambiguity seen in Fig. 5.14, where different grain sizes R = 100, 200, 400 μm and b = 1, 2, 4 μm resp. give similar results, Fig. 5.15 shows the selection criterion. Those parameters giving results as shown in Fig. 5.15 were left out. Here, both V_p and V_s, calculated with R = 100 μm and b = 5 μm, lie above the measured values.

A tabular form of presentation of the results is given in Fig. 5.16. There are four main horizontal blocks, one for each grain size (here 100, 200, 300 and 400 μm). The columns stand for different initial contact radii and the rows for different porosities; 1 for the lowest and 4 for the highest porosity. The field of parameters which were sorted out in the first instance is crosshatched. A + sign denotes too high

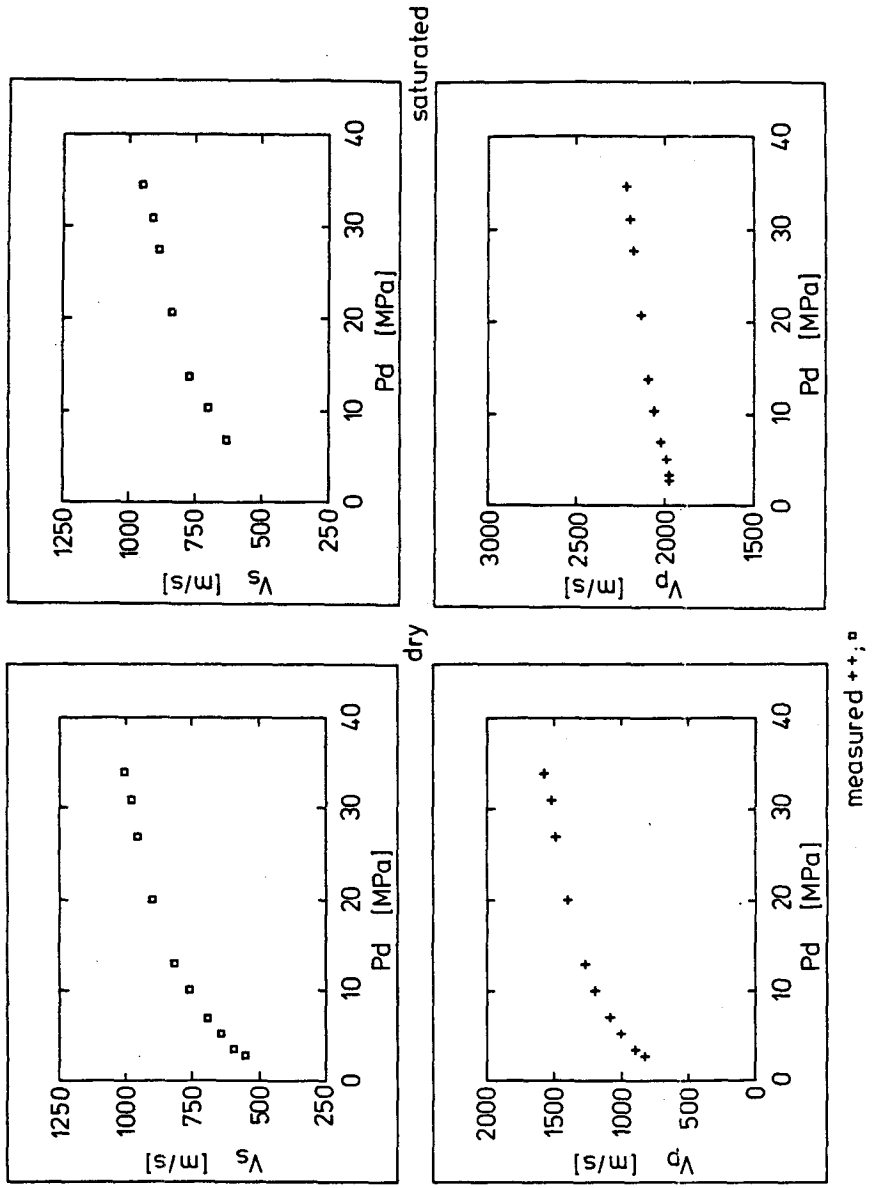

Fig. 5.13: The data used for modelling from Domenico (1977); V_p and V_s in dry and saturated glass beads

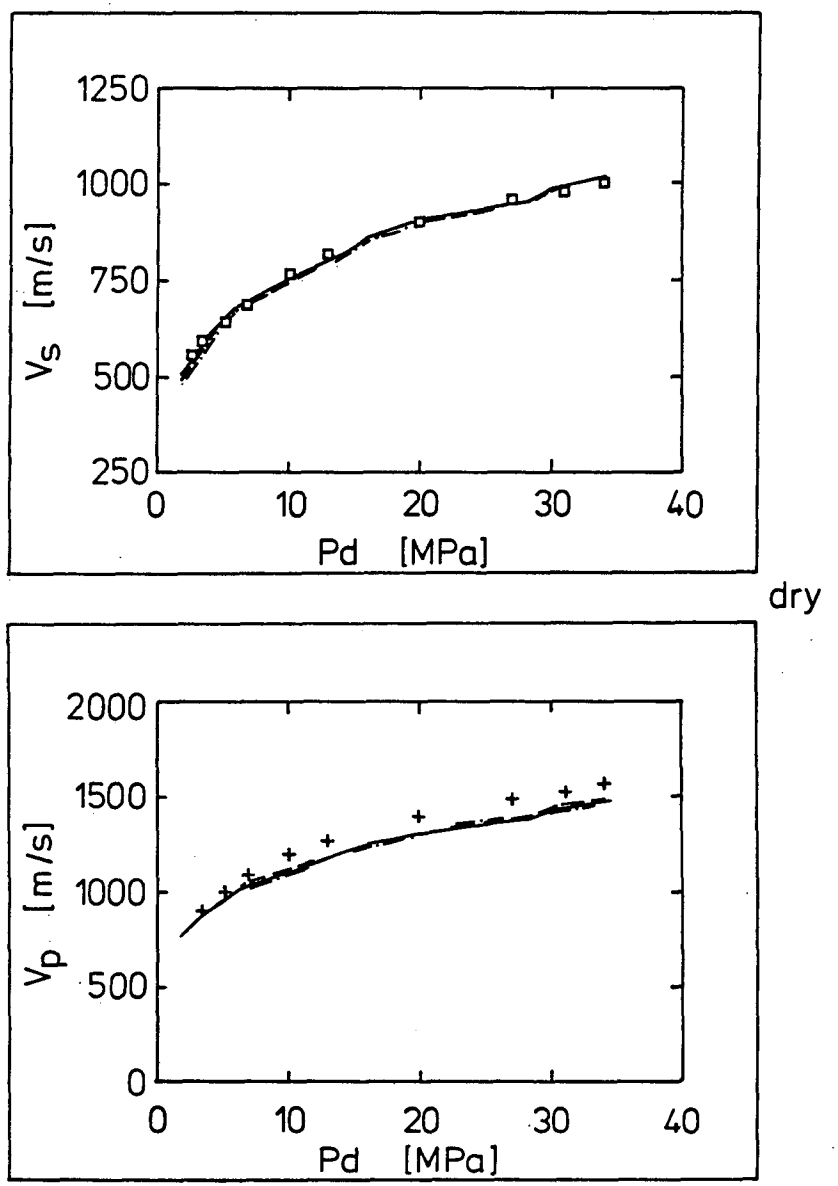

Fig. 5.14: Calculated (with Biot-Model) and measured V_p (bottom) and V_s (top) for different grain sizes

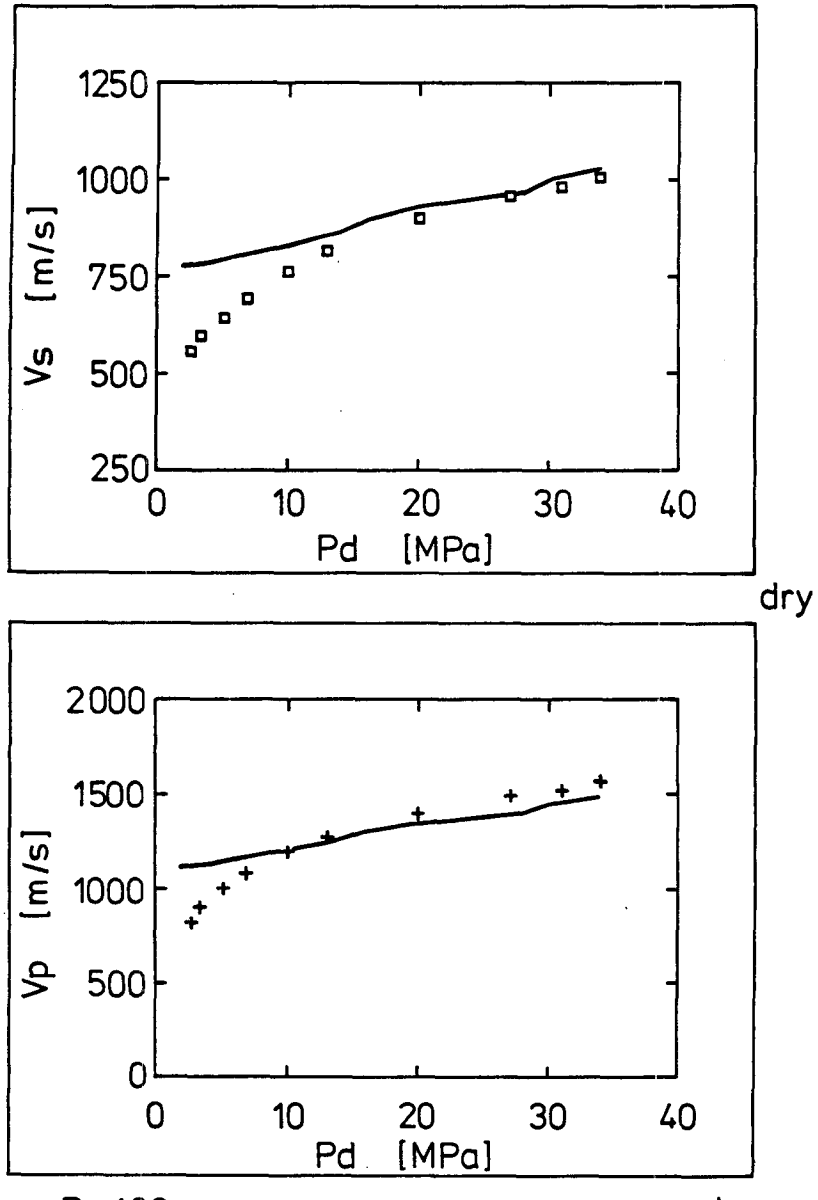

Fig. 5.15: Bad fit of the velocities calculated for R = 100 µm, b = 5 µm with the measured ones

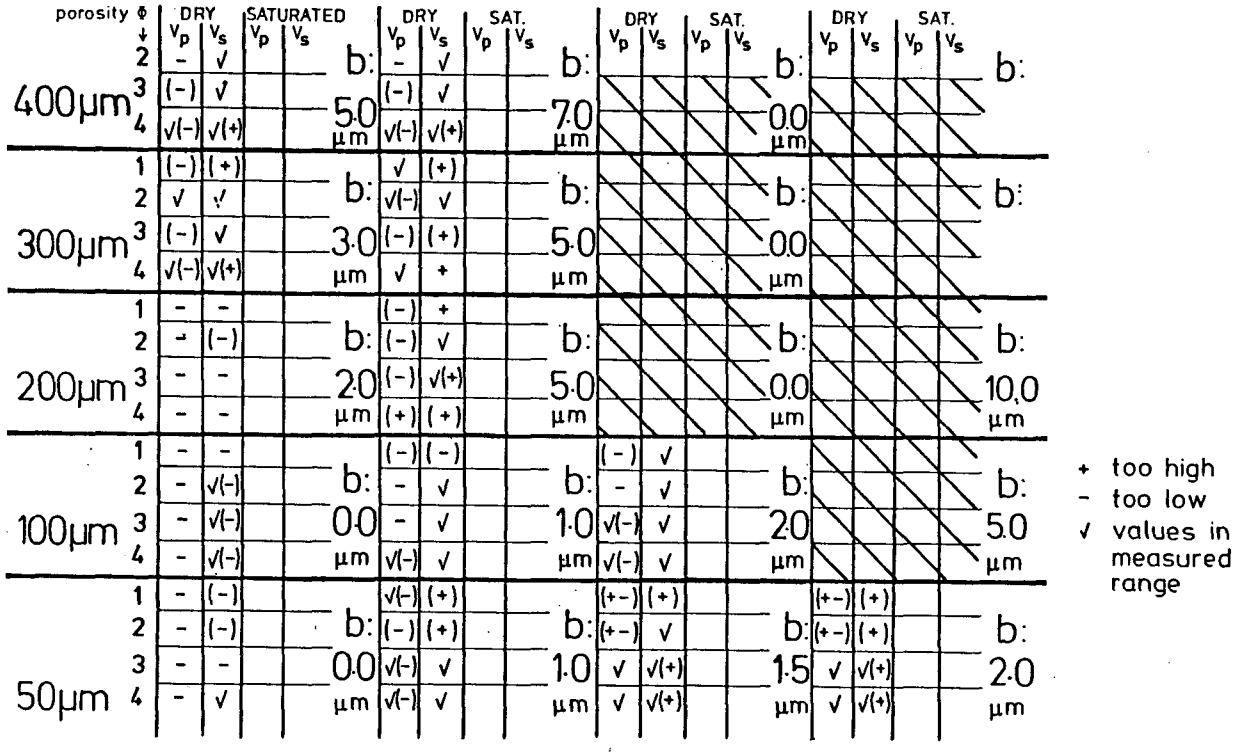

Fig. 5.16: Calculation results for dry samples. V_p and V_s for different grain sizes, initial contact radii and porosities

values, - too low and more or less matching values. Bracketed values are valid for small deviations.

To obtain an idea about the possible ϕ range, the data was first modelled with arbitrary values, constant with pressure, ranging from 0.2 to 0.45. Although the V_p and V_s for the dry case are less sensitive to ϕ changes, the calculations for higher ϕ seem to match the data better than for lower ϕ values in Fig. 5.16.
A further selection of the parameter was made by considering the saturated case. Using the same ϕ values as for the dry case, the V_p and V_s at 'zero'-(V_0) and at 'infinite'-(V_∞) frequencies were calculated. Only those values for which the measured V_p and V_s lie in the total dispersion range were accepted. For example in Fig. 5.17, with R = 400 μm, V_s lies in the dispersion range, but the first values of V_p are too low. Raising the initial parameter would fit the V_p values, however the V_s would be too high. Calculations with constant 'ϕ' in Fig. 5.18 demonstrate that only those values calculated with porosities between 0.3 and 0.45 lie in the range of the measured data. The velocities for $\phi \leq 0.3$ are much higher and for $\phi \geq 0.45$ are much lower than the measured values. Similar results were obtained with other grain sizes, so that the ϕ-range was taken between 0.3 and 0.45.

Now, taking ϕ = f(pressure), the calculations were once again carried out for the dry and the saturated cases.

These results are once more represented in a tabular form (Fig. 5.19), where, as earlier, the main horizontal blocks represent grain sizes, the columns different initial contact radii and the rows the porosity functions; where the smaller numbers stand for lower ϕ-values. With these data, the ambiguity of the dry case seen in Fig. 5.13 was removed; taking R = 400 μm, b = 5 or 7 μm, whereas V_p and V_s for the dry and V_s for the saturated sample fit the measured data reasonably well, the V_p (saturated)-values are lower than the measured ones. Similar results were obtained with grain

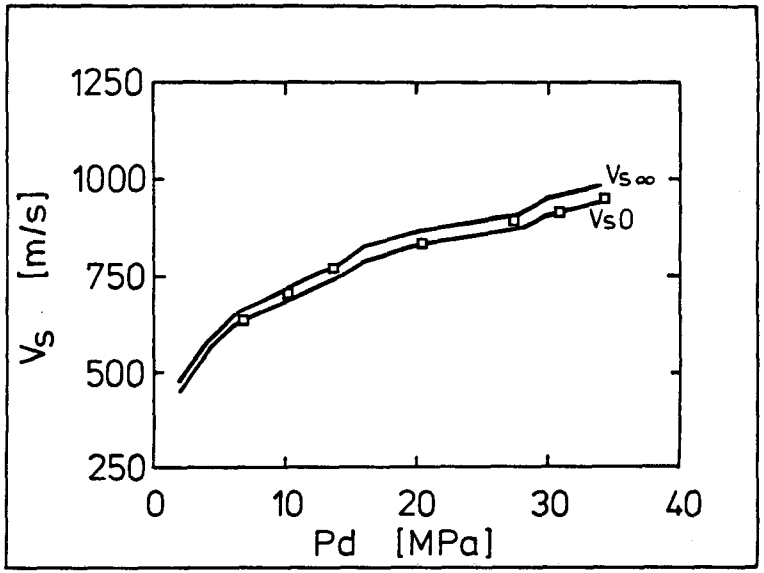

saturated

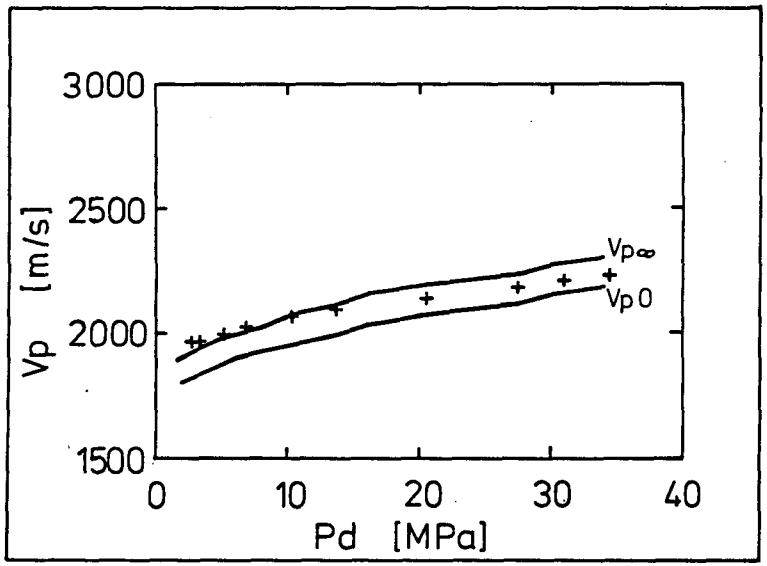

R: 400 µm
b: 5.0 µm

measured ++; ▫▫
calculated ——

Fig. 5.17: Calculation results for R = 400 µm, b = 5 µm: V_s lies in the dispersion range, but first values V_p are too low.

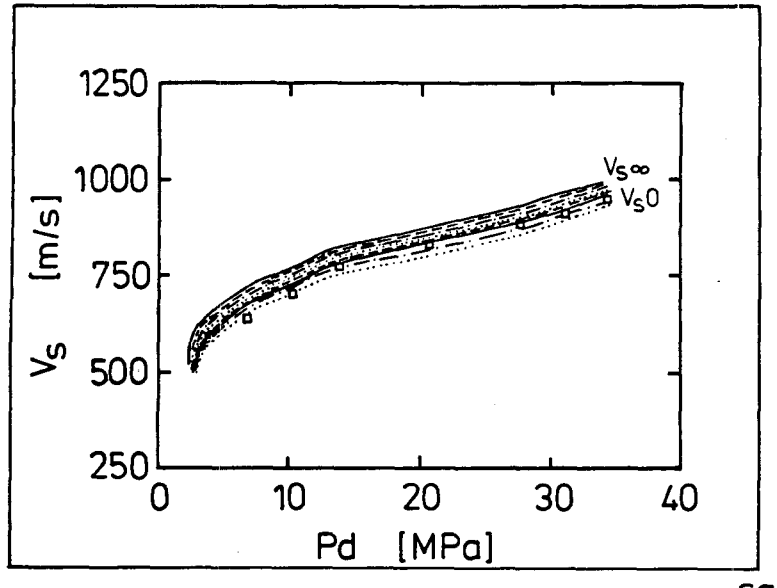

saturated

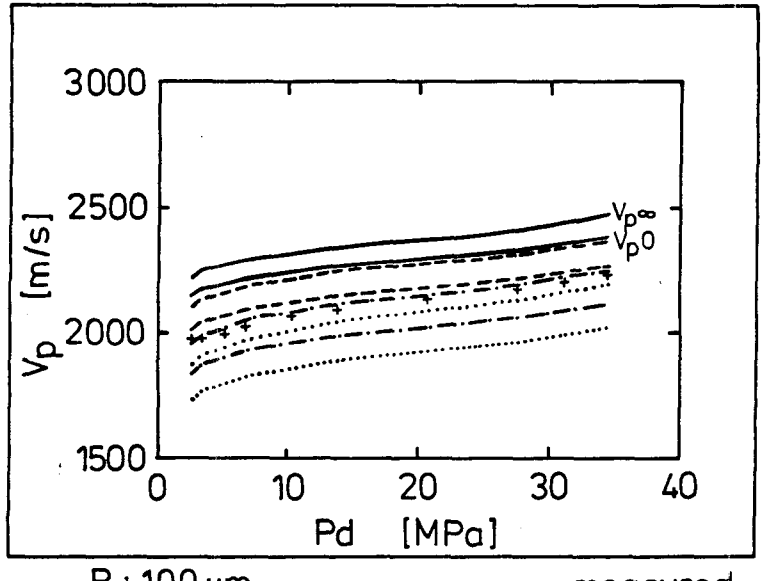

R : 100 µm

b : 2.0 µm

measured ++ ; □ □

calculated 0.20 0.25 0.35 0.45

(with variable porosities)

Fig. 5.18: Calculation results for different porosities. Only values calculated with porosities from, 0.3 to 0.45 lie in the range of measured values.

sizes ≥ 100 μm, the porosity functions 3 and 4 gave better results. The best fit, however, was obtained with R = 50 μm, which is approximately the same as the grain size given for the glass beads (Fig. 5.19, last block). Also the porosities used for the calculations are similar to those reported in the paper, Domenico (1977). Calculations with grain sizes below 50 μm again deviated from the measured values.

Thus it is possible to predict the range of possible physical parameters by modelling the dry and saturated velocity data. Further predictions are possible only if the attenuation is modelled, considering the anelasticity in the dry as well as the saturated case.

5.5.2 On Natural Sand Grains

Next, the seismic response in dry and saturated samples measured in the laboratory was modelled with the Biot theory again. But now the shear modulus of the frame was taken a complex constant, $\bar{\mu} = \mu_r + i\mu_i$, with μ_i describing the attenuation in the frame. This over-simplification should be borne in mind for further considerations.

The results ($Q_p^{-1}(w)$, $Q_s^{-1}(w)$) are presented in the Fig. 5.20 for the grain radius 110 μm and in Fig. 5.21 for grain radius 275 μm, with $Q_p^{-1}(w)$ below and $Q_s^{-1}(w)$ above in both figures. The results are striking in their semblance to the observations. Taking first the coarser grains, depending on the grain configuration (Fig. 5.21, bottom), the Q_p^{-1} is indeed predicted to be more or less constant or even increase with pressure at the frequency of measurement, indicated by an arrow. This correlates with the observations and with the calculations only with the Biot Model (Fig. 5.11, bottom).

But in contrast to the first modelling attempt (Fig. 5.11, top), the shear wave attenuation modelled here (Fig. 5.21,

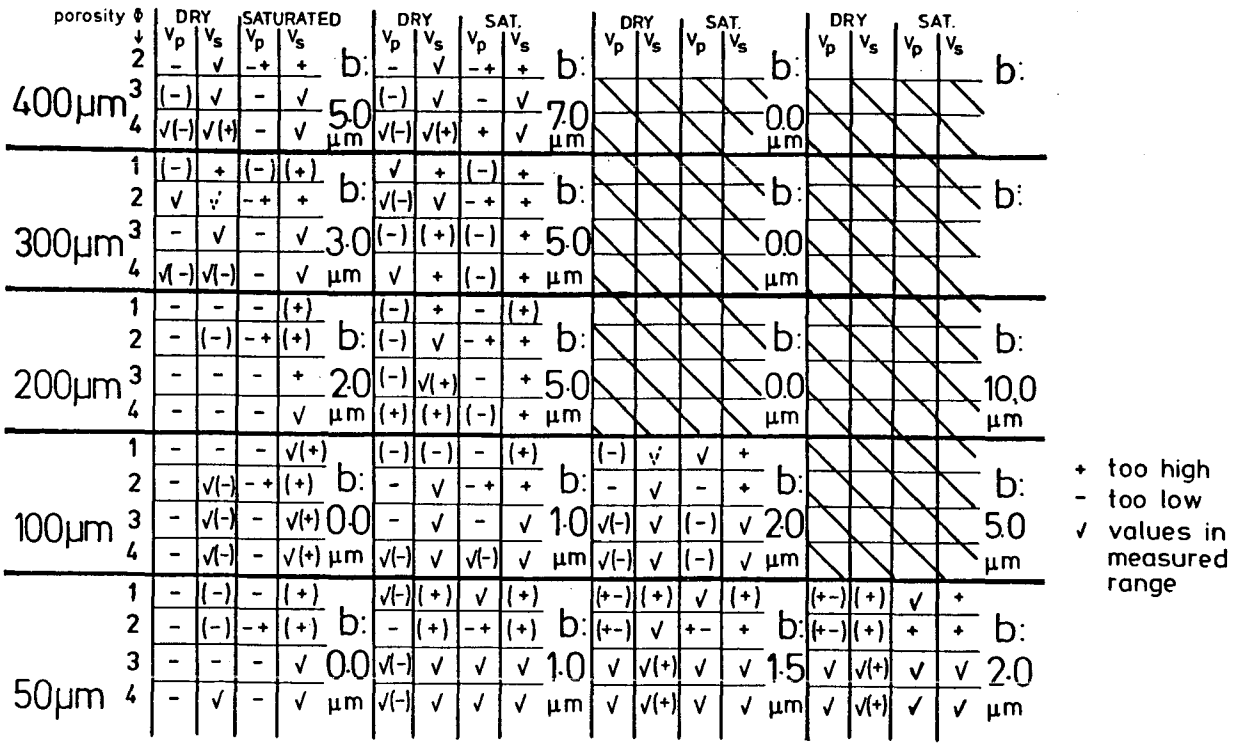

Fig. 5.19: Calculation results for dry and saturated samples. V_p and V_s for different grain sizes, initial contact radii and porosities

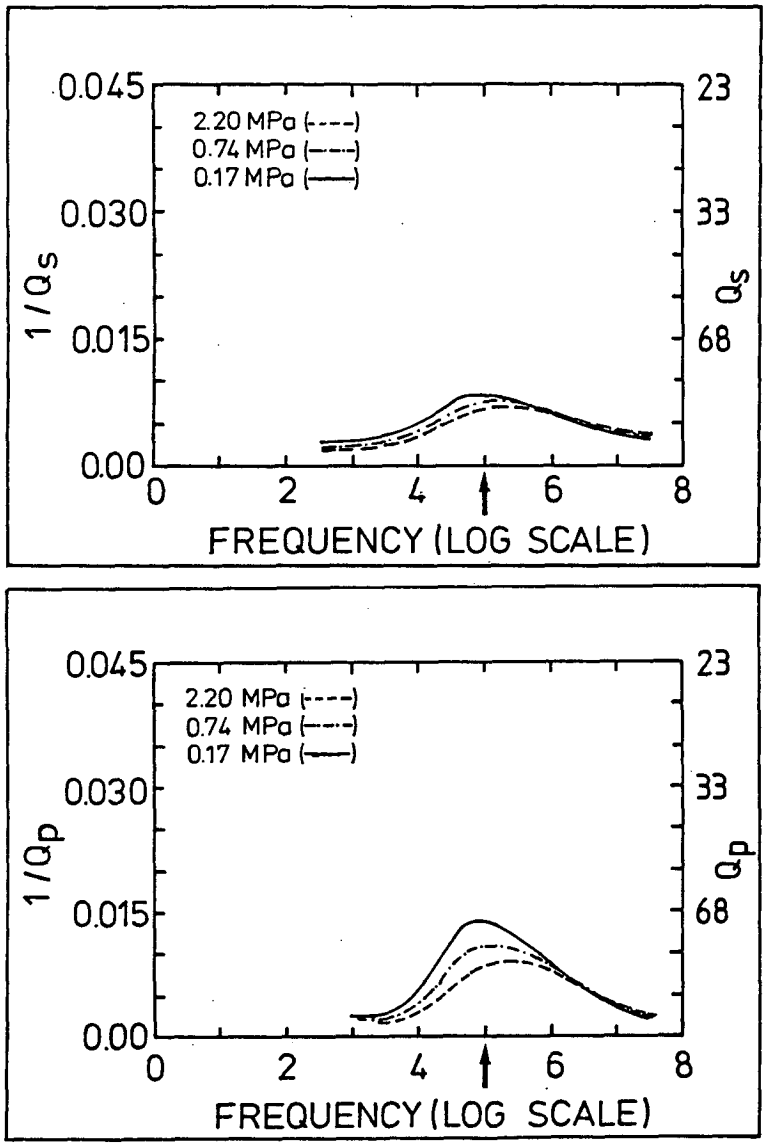

Fig. 5.20: $Q_p^{-1}(\omega)$ (bottom) and $Q_s^{-1}(\omega)$ (top) calculated with the combined CRM-Biot-Friction-Model for a grain radius = 110 µm (≙ sample P6) at three different pressure steps. At the frequency of measurement, indicated by the arrow, both Q_p^{-1} and Q_s^{-1} show a decrease with pressure.

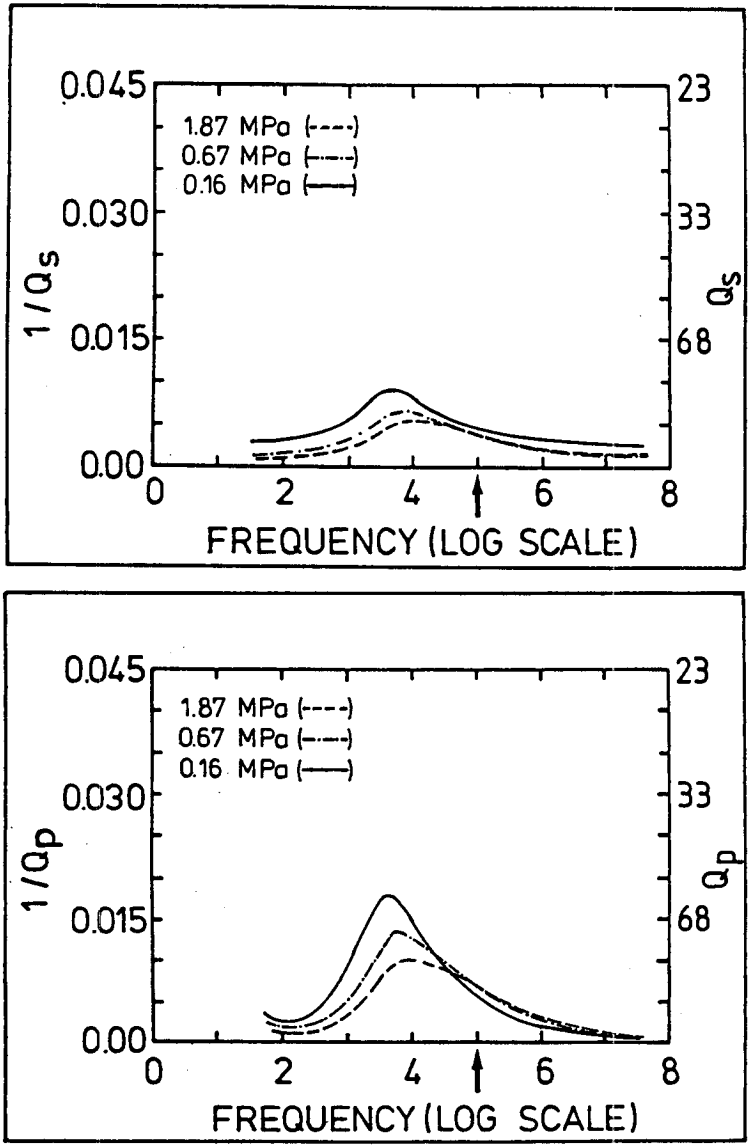

Fig. 5.21: $Q_p^{-1}(w)$ (bottom) and $Q_s^{-1}(w)$ (top) calculated with the combined CRM-Biot-Friction-Model for a grain radius = 275 µm (≙ sample P2) at three different pressure steps. At the frequency of measurement, indicated by the arrow, Q_p^{-1} shows slight increase and Q_s^{-1} a decrease with pressure.

top) also coheres with the observation. As opposed to the attenuation predicted only on the basis of viscous flow losses, here the Q_s^{-1} does indeed reduce with pressure at the frequency of measurement. The finer grains (110 μm radius, Fig. 5.20) show a shift in the attenuation peak towards higher frequencies. With different pressure steps, the changes therein are not so pronounced though. (Both Q_s^{-1} and Q_p^{-1}, Fig. 5.20, top and bottom resp., show a decrease at the frequency of measurement, again arrow.) This too would agree with the observations.

Thus the phenomological behavior of the seismic wave attenuation is satisfactorily described by these two mechanisms of solid-solid friction and viscous flow of the fluid. But considering the range that Q^{-1} can take in the measurements, the predicted Q^{-1} values are too low. This is also reflected in the velocities calculated for the saturated case.

In Fig. 5.22, 5.23 the calculated P- and S-wave velocities in saturated 110 μm and 275 μm grain radius samples, resp. are shown, taking here too $\bar{\mu} = \mu_r + i\mu_i$. V_s (calculated) lie in the range of the measured values, but owing to the limited no. of measurements and the uncertainty in determining the arrival times of the S-waves, V_s is not considered reliable for this check. (Fig. 5.22, top, for the finer grained sample and Fig. 5.23, top, for the coarser one). V_p, accurately determinable, is calculated lower than the measured velocities. (Fig. 5.22, bottom, for the finer grained sample and Fig. 5.23, bottom, for the coarser one). In each case the frequency of measurement is indicated by an arrow. From the velocity dispersion curves, it is obvious that the frequency of the present measurements lies in the high frequency range of the Biot equations. The two dispersions, one predicted by the Biot equations dU_B and the measured one dU_m, can be calculated as follows:

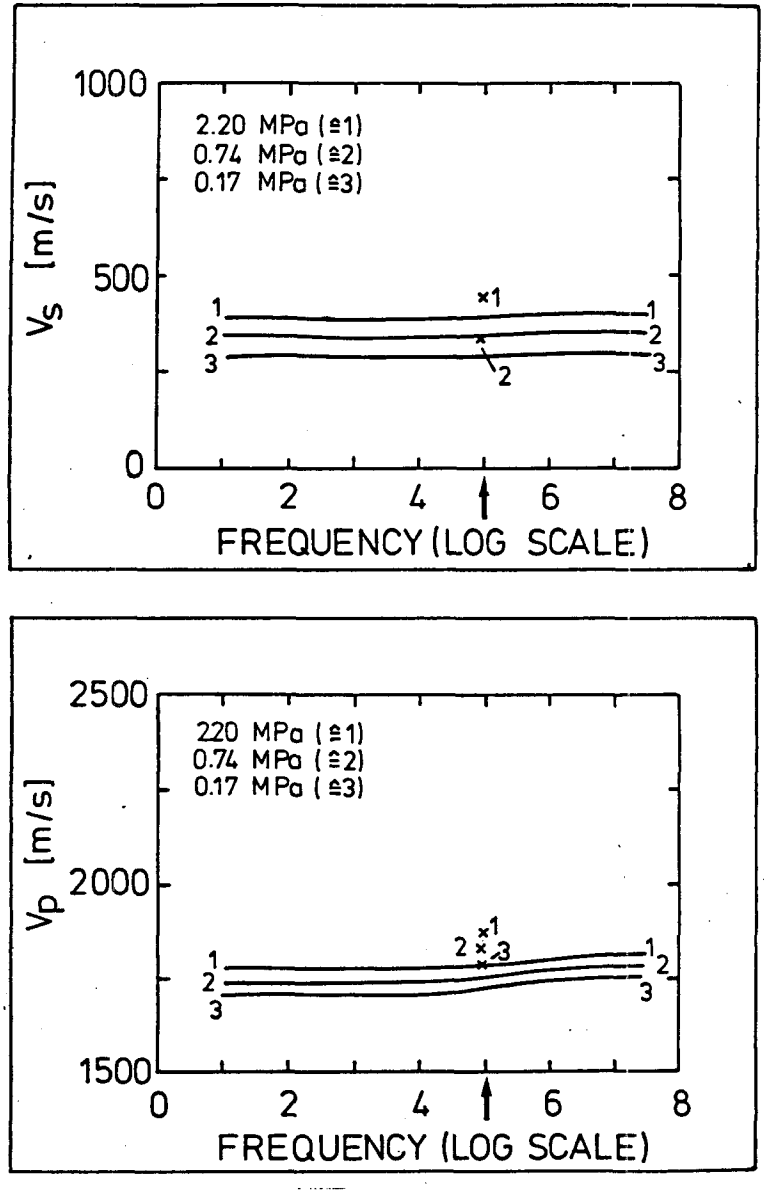

Fig. 5.22: $V_p(w)$ (bottom) and $V_s(w)$ (top) calculated with the combined CRM-Biot-Friction-Model for a grain radius = 110 µm (≙ sample P6) at three different pressure steps. Symbols mark measured values in the corresponding sample P6. Frequency of measurement is indicated by the arrow.

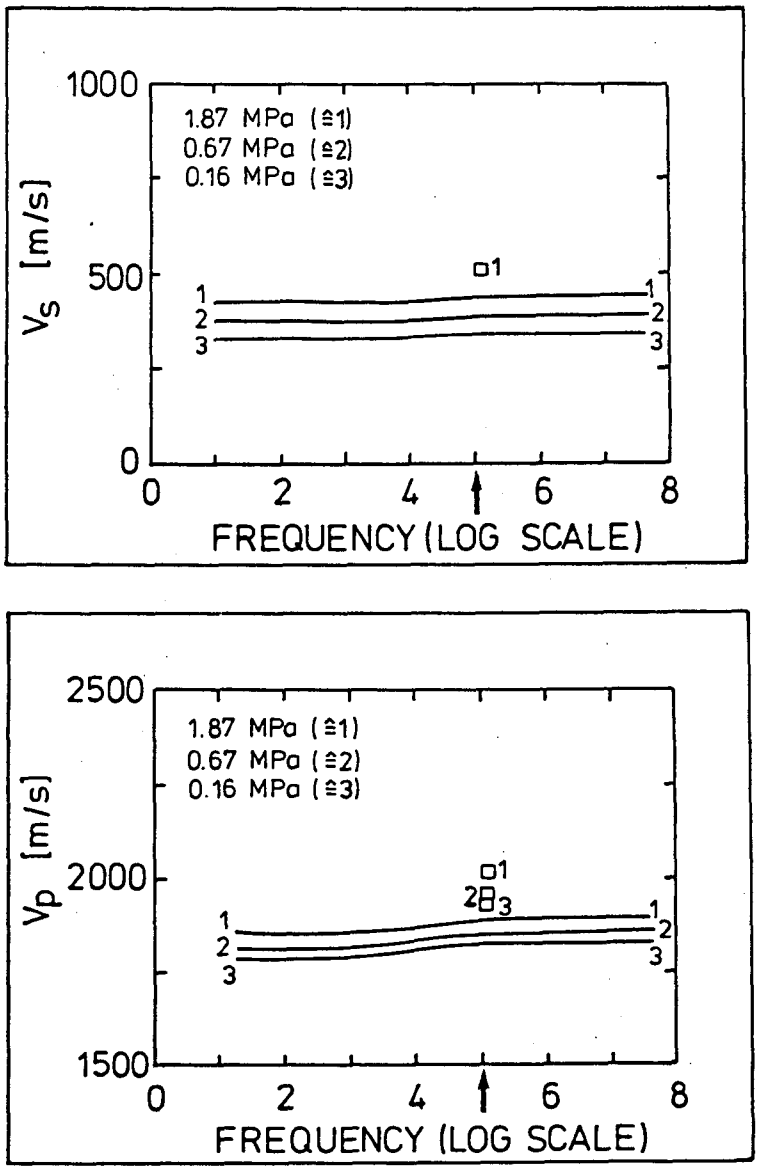

Fig. 5.23: $V_p(w)$ (bottom) and $V_s(w)$ (top) calculated with the combined CRM-Biot-Friction-Model for a grain radius = 275 µm (≙ sample P2) at three different pressure steps. Symbols mark measured values in the corresponding sample P2. Frequency of measurement is indicated by the arrow.

$$dU_m\ [\%] = \Delta V_m / V_0 * 100 \qquad (5.54)$$

$$dU_B\ [\%] = \Delta V_B / V_0 * 100 \qquad (5.55)$$

dU_m : dispersion in percent wrt measured V_p, V_s

dU_B : dispersion in percent wrt Biot theory for V_p, V_s

ΔV_m, ΔV_B : $V_{measured}$ (V_{Biot}) - V_0

V_{meas} : measured V_p, V_s

V_{Biot} : V_p, V_s from Biot eqns. at the frequency of measurement

V_0 : 'zero frequency' velocity from Biot eqns.

Both dU_m and dU_B are plotted together for V_p in Fig. 5.24 (bottom) and for V_s in Fig. 5.24 (top). In both cases the Biot-predicted dispersion lies below that actually measured. In the case of S-waves, there is strong decrease in dispersion with pressure. The Biot dispersion is lower by about 5...10%. This observation is more effectively seen in V_p-dispersion (Fig. 5.24, bottom). The discrepancy between measured and calculated dispersion is to the order of 5% or more.

This discrepancy between measured velocity dispersion and Biot-predicted one in consolidated rocks has been reported by Winkler (1983, 1985, 1986) and Murphy (1984a) as well. The dispersions measured by Winkler (1985) are given in Fig. 5.25 in a slightly different form. A measure of dU_m and dU_B in these figures would be the difference between the two Biot limits (dashed lines) for dU_B and between the lower Biot limit and saturated U_p (solid lines) for dU_m. Obviously, here too, the measured dispersions are higher than those predicted by the Biot theory. Winkler (1985) relates this effect to the pore pressure buildup in the sample, differentiating between only dragging of the pore fluid along with the solid frame at low frequency and the additional local flow losses at higher frequency. At low frequency there is enough time for flow to take place, equilibriating the pore pressure, the sample is in relaxed state here. At high frequency (above $\approx$ 1 kHz, Winkler, 1986) the pore pressure cannot equilibrate during one half cycle of the acoustic wave. Murphy (1984a)

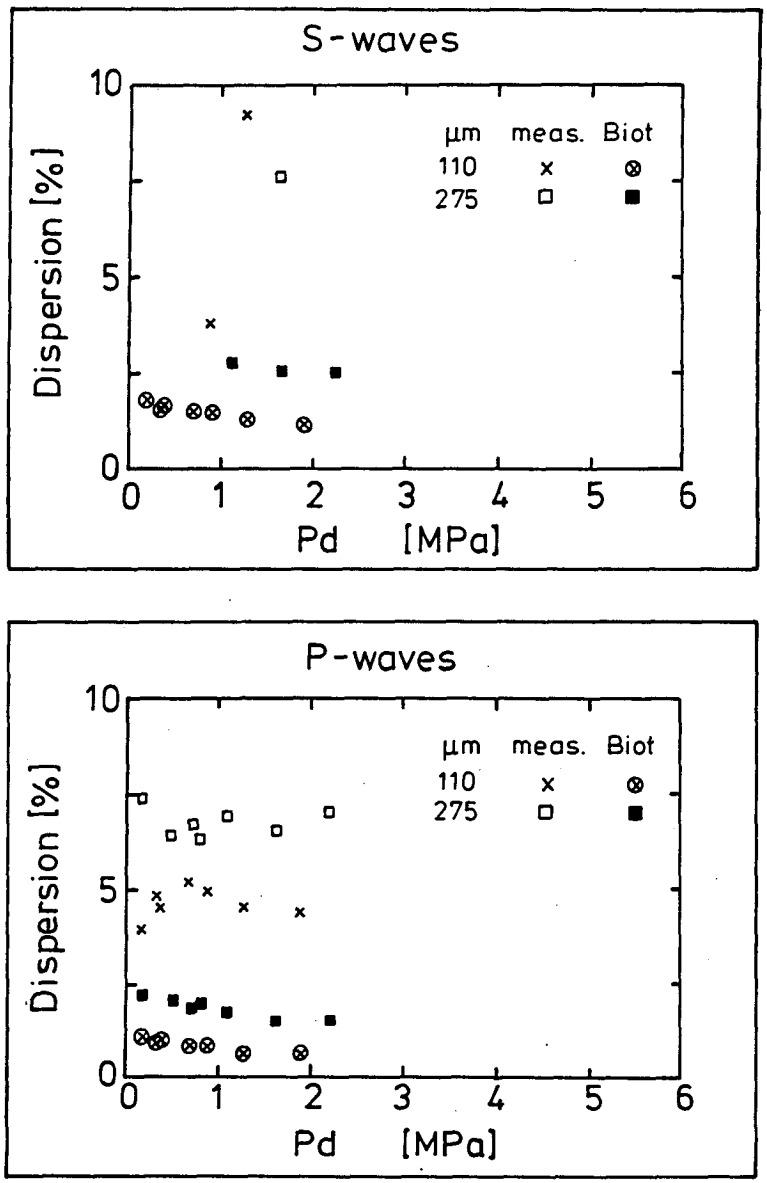

Fig. 5.24: Comparison of Biot and measured dispersion in P- (bottom) and S-waves (top) in the 110 µm and 275 µm sample. Dispersion on account of the Biot theory is much less than the measured one.

postulates, that the dispersion could be due to the different compressibilities of the pore space. The contact between two grains being extremely irregular (Murphy et al, 1986), these interstices in the contact area are also filled with the pore fluid. In comparison to the pore space, generally imagined as circular or nearly circular, these contact areas are more compressible. This in turn would mean that under the effect of an oscillating acoustic loading, the grains respond accordingly, with the pore fluid in the interstices of the contact areas being pressed out of the gaps and sucked back in again. Thus energy is lost by this viscous shearing. But this local squirt flow mechanism has to be rejected, because the main losses in the saturated case, as seen in Sec. 4.4 and in Fig. 4.12, are in bulk and not in shear.

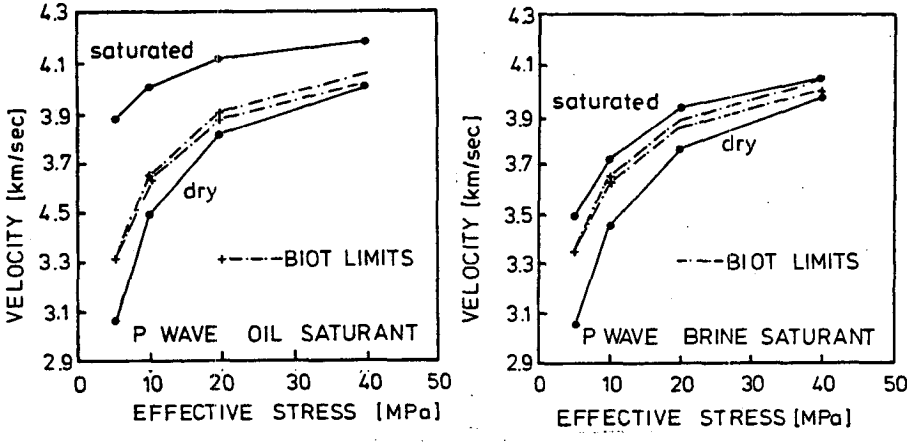

Fig. 5.25: Compressional phase velocity as function of effective stress in Berea sandstone. Data are shown for dry and saturated samples (oil-saturated: left; brine-saturated: right) at 400 kHz. Biot low- and high-frequency limits are shown on dashed lines. V_p measured (solid lines) are higher than those predicted by the Biot theory (dashed lines in both oil- and brine-saturated Berea sandstones at different pressures). From Winkler (1985)

An alternative explanation could be the frequency dependence of the 'dry' frame parameters. The shear modulus of the frame used in these calculations is taken as a complex constant, independent of the frequency. If it were frequency dependent, an additional peak in the attenuation behavior and an increased dispersion would be present. Frequency dependent losses in the frame could be in bulk as well, which is not considered here.

The losses related to an increased dispersion would consequently be consistent with the observed attenuation. From the conditions of a causal relationship, dispersion is coexistent with attenuation. Not bothering about the mechanisms underlying their dispersion/attenuation, the Kramer-Kronig equations (Ben-Menahem and Singh, 1981) relate the two qualities. Nowick and Berry (1972) relate a large dispersion to either large attenuation over a small frequency band or small attenuation over large frequency band. The equations of Liu et al (1976) for individual relaxations approximated by the Standard Linear Solid gives, in the notation of Winkler (1985), the attenuation as a function of dispersion, frequency and distribution width.

$$\frac{1}{Q} = \frac{2\Delta V}{V_0 \ln(\tau_1/\tau_2)} \tan^{-1}\left[\frac{\omega(\tau_1-\tau_2)}{1+\omega^2\tau_1\tau_2)}\right] \qquad (5.56)$$

with one relaxation peak only this becomes

$$\frac{1}{Q} \approx \frac{2\Delta V}{V_0} * \frac{\omega\tau}{1+\omega^2\tau^2} \qquad (5.57)$$

$\tau_{1,2} = 1/\omega_{1,2}$
$\omega_{1,2}$ = distribution width
ω = frequency
$\Delta V = V_{meas} - V_0$ = velocity dispersion
V_0 = velocity at zero frequency from Biot-equations
V_{meas} = measured velocity

		1/Q for P-waves			1/Q for S-waves		
	press [MPa]	one peak	distr. of peaks	meas.	one peak	distr. of peaks	meas.
P2	0.17	.0737	.0108	.0258	———	———	———
	0.50	.0639	.0093	.0298	———	———	———
	0.80	.0630	.0092	.0320	———	———	———
	0.74	.0667	.0098	.0323	———	———	———
	1.09	.0690	.0101	.0343	-.0113	-.0017	.0388
	1.62	.0654	.0096	.0345	.0762	.0112	.0346
	2.20	.0702	.0103	.0345	.1650	.0241	.0330
P6	0.16	.0394	.0058	.0123	———	———	———
	0.32	.0481	.0070	.0131	———	———	———
	0.36	.0453	.0066	.0134	———	———	———
	0.67	.0519	.0076	.0129	-.0168	.0025	.0187
	0.87	.0496	.0073	.0138	.0378	.0055	.0189
	1.26	.0456	.0067	.0135	.0923	.0135	.0162
	1.87	.0439	.0064	.0120	.1458	.0213	.0117

Table 5.2: Q^{-1}-values from dispersion of the velocities

Table 5.2 presents the values calculated by these equations for the two grain sizes 110 µm and 275 µm at different pressures for one relaxation peak and for a continuous distribution of relaxation peaks over six decades of frequency, as suggested by Winkler (1985). Also given there are the measured values.

Compared with the measured values, the calculated attenuation is higher for one relaxation peak and lower for a continuous distribution of relaxation peaks. Two reasons could be responsible for this. One, that the distribution width is erroneous and/or second, and this is just as plausible, the relationship between attenuation and dispersion is not linear and the Kramer-Kronig relationship does not hold true. This would be the case if frequency dependent friction was indeed a driving force behind the attenuation.

Assuming that the pore pressure buildup in the sample can be approximated by a decrease in the compressibility of the pore

fluid, the samples were modelled again via the steps explained above, but with increasing bulk modulus of the pore fluid. A value of 2.51 GPa as opposed to the normal value of 2.22 GPa was needed to attain velocities as measured in the experiments. V_p in the 275 μm sample lies at the unrelaxed velocity and V_p of the 110 μm sample is lower than the high frequency velocity. These calculations are shown in Fig. 5.26 for the two samples at different pressure steps. The velocities calculated at the frequency of measurement match very well the measured velocities also marked in the above diagram. These assumptions are strengthened further considering pore pressure buildups in a porous medium. Studying the pore pressure buildup coefficient B in porous rocks,

$$B = (dP_f/dP_c)|_{dm_f} \quad , \tag{5.58}$$

p_f = fluid pressure
p_c = confining pressure
m_f = mass of fluid per unit bulk volume

Green and Wang (1986) report the pore pressure prevailing at depths up to ≈ 3 km to be near the lithostatic pressures. An additionally imposed seismic loading is borne by the pore pressure also and its effect is to reduce the differential pressure, which would be reflected in seismic signature.

5.5.3 Consequences

The combined CRM-Biot-Friction theory describes the behavior of a fully saturated porous medium under the effect of an oscillating acoustic wave excitation phenomenologically. The driving mechanism in this theory is a dragging of the pore fluid along with the frame and a solid-solid friction between the grains.

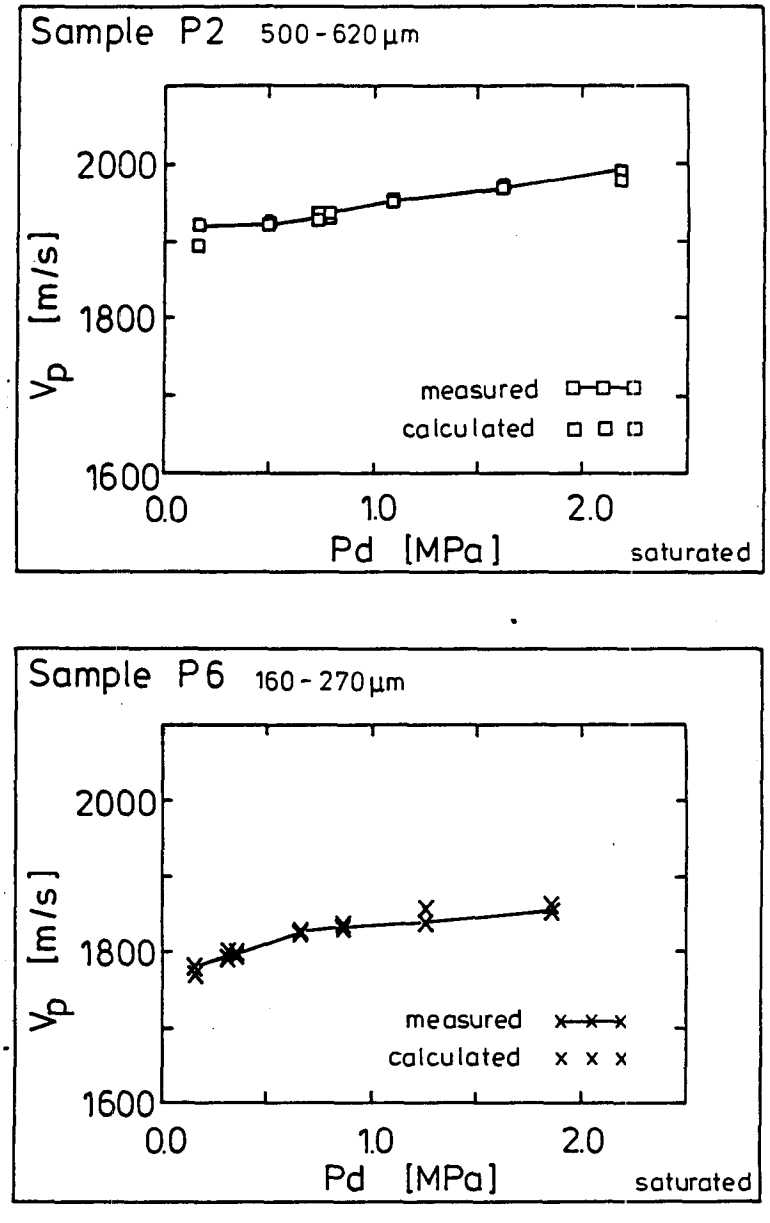

Fig. 5.26: V_p calculated with k_f = 2.51 GPa compared with measured values for a coarse grained (top) and a fine grained sample (bottom)

For P-waves it poses some shortcomings. Both, the velocity and the attenuation predicted are less than those measured. The range of the quality factor Q_p for the experiment lies between 10 and 40. But the predicted values between 60 and 200 are somewhat out of this range. This is despite the frictional losses being accounted for. If the higher velocities measured is due to pore pressure buildup, it would lead to a higher bulk modulus of the pore fluid. The calculation show that the bulk modulus of 2.51 GPa suffices to match the measured velocities. The bulk modulus of ordinary water at 0.1 MPa, 25°C is 2.188 GPa and at 100 MPa, 25°C is 2.87 GPa (Handbook of Physical Constants, 1974). Consequently a bulk modulus of 2.51 GPa would correspond to a pressure of ca. 50 MPa in the pore fluid on the passage of a compressional wave.

This can be named a naive method of solving the problem, but it defies detraction, if we critically examine both the information it delivers and where it is ineffective.

Of course, it does overlook the fact that there are losses associated with this pore pressure buildup. The local flow attempting to equilibrate it results in strain relaxation. The time delayed response of the strain to the stress results in a loss of energy. This vital factor which must be accounted for could be reflected in the additional losses measured but not explained by the Biot Model.

But on the other hand, this sort of treatment would approximate the pore pressure buildup in a specimen. Depending on the fluid bulk modulus required to approximate the velocity, its pressure response would describe the pore pressure. The implication of this can be seen from the following:

1.) In seismically active regions continuous measurements of V_p would be useful in giving indications about the pressure relations in the underground. Comparing V_p measurements over a sufficiently long period of time with some reference value

taken in the same place, with the same configuration would give the changes taking place in the underground layers in terms of the elastic (and anelastic) parameters used to model. The reference measurement is modelled by the Biot theory following the steps described earlier and some arbitrary value is derived for the fluid bulk modulus. Now all subsequent values needed for modelling the measured data are compared to this. Any deviation gives a hint to the pore pressure buildup and would be a valuable method of forecasting the mechanisms going on below. If this method of assessing pore pressure buildups prooves successfully it could be an additional parameter in earthquake predictions.

2.) Despite the neglection of Q^{-1} due to this effect, the grain characteristics with respect to grain size, initial contact radius or compaction and porosity as seen in Sec. 5.5.1, 5.5.2 can be predicted. Though the valuable and elusive fluid bulk modulus is missing, all the same, certain presumptions can be made on the physical characteristics of the measured quantities. These predictions are additionally supported by the shear wave characteristics which are independent of these pore fluid characteristics.

3.) In oil or water prospection, this would also give an additional method of evaluating the reservoir properties. Kümpel and Lohr (1985) have reported a method of studying in situ permeability from non-dilational soil deformation caused by ground water pumping by studying pore pressures registered in tilt measurements recorded in a sensitive borehole tiltmeter. A simultaneous P-wave registration would be interesting to verify the present hypothesis.

These additional local flow effects are not observed in glass beads, where the velocities and, through them, some grain characteristics are predictable solely on the basis of the Biot theory.

Winkler (1983) reports that this additional local flow effect seen in contacts of naturally occurring grains is not observed in fused glass beads. He suggests the reason behind this to be the sintered, and hence stiffer, contacts between the beads also seen reflected by the lack of any pressure dependant effects. These sintered contacts successfully prevent local flow mechanisms.

The present work shows that whereas a hindered local flow could be postulated for glass beads, this must not necessarily be due to the sintered contacts. This is inferred from the good matching by the Biot theory of loose glass beads which have no sintered contacts. Consequently there must be an oppositional mechanism underlying this. Here some ideas are presented with the reservation, that these might prove to be outlandish on a closer examination.

- The contacts of glass beads are very smooth, much smoother than what naturally occurring grains could get (Fig 5.27). The evidence for a rougher surface, and with it more hooking up of adjacent grains and a stiffer frame is reflected in the higher velocities measured in natural sands. This smoothness prevents local fluid flow, the entire contact being covered by one film of pore fluid.

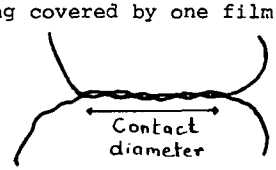

Fig. 5.27: Cartoon of contacts in natural grains

- The mineralogical configuration could also play an important rule. Glass beads and quartz grains have the same chemical composition. But whereas the sand grains are crystalline, consisting of discrete SiO_2 tetrahedra, the glass beads are amorphous. Chemically, solids characterized by absence of an order structure ie those lacking in a regular arrangement of atoms are termed as amorphous bodies. They are classed with isotropic substances (Betekhtin, 1970). The amorphous nature could possibly react much

differently to a seismic scintillation than crystallographic bonds in the quartz grains. This could be tested by comparing measurements on natural glasses with chemically equivalent crystalline solids and modelling both.

- The amorphous nature of the glass beads could be responsible for another effect. The increased surface energy could be due to their amorphous nature. This surface energy is instrumental in binding the pore fluid closely to its surface. The pore fluid film on the glass beads is much thicker than in quartz grains limiting the amount of pore fluid available for being squeezed in and out of the pores during high frequency seismic loading. Thus there is a hinderance to the local flow attenuation accentuating the Biot explained losses in glass beads as compared to the crystalline quartz grains.

6. Conclusions

As fundamentally significant conclusions given in this thesis, there is a unique relationship between some physical and seismic parameters. This can be summarised as follows:

- Rigidity coefficient and P-wave velocity correlate at low pressures. This correlation decreases with increasing pressures.
- Coarseness of grains enhances the velocity and the attenuation of P-waves and that of the S-waves, but the S-wave velocity is unaffected by grain size.
- Angularity of grains causes a decrease in velocity, attenuation and rigidity coefficient.
- Dry grains show high shear losses, whereas saturated grains have predominant bulk losses of seismic energy.

Additionally, from observation of V and Q^{-1} change with pressure, the nature of an underground layer can be determined:

- A coarse grained layer exists, if Q_s^{-1} decreases sharply and Q_p^{-1} is more or less constant with an increase in pressure.
- A fine grained layer is present, if both Q_p^{-1} and Q_s^{-1} decrease moderately with pressure.

The different approximations made to model the dry and saturated case allow some statements about the attenuation mechanisms. Most important knowledge gained here is that the frame moduli can be calculated by the Contact Radius Model (CRM). These frame moduli, given assumed values until now, can be used in modelling the saturated case. There is not one but several mechanisms effective in attenuation of the seismic waves. Solid-solid friction also causes a loss of seismic energy. The friction calculated remains amplitude

dependent, but the limit beyond which it is effective is considerably lower in loose sands than previously assessed (Winkler and Nur, 1982). Thus this mechanism gains importance in modelling unconsolidated sediments at strains $\geq 10^{-6}$, in coarser grains $\geq 10^{-7}$. This implies that care has to be taken in planning seismic surveys, such that these non-linear processes are not encountered with. They may be important near to a seismic source.
The friction is taken as frequency independent, which is an over-simplification. Attenuation mechanisms are observed to be frequency dependent, different mechanisms being effective at different frequencies (Burkhardt et al, 1986).

The Biot-predicted fluid flow losses are most effective at high frequencies (Stoll, 1977), the position of the attenuation peak being dependent on the permeability and viscosity (Meißner and Theilen, 1983). In the present thesis the presence of such losses is modelled. The losses, strongly frequency dependent with peaks in the high frequency range, need to be augmented by additional losses to explain the laboratory observations.
Squirt flow attenuation mechanisms are not effective here, since they cause mainly shear losses (Murphy et al, 1986). The 'loss diagram', Fig. 4.12, shows mainly bulk losses in saturated sands. Additionally, while they are important at seismic frequencies, this might not be so at higher frequencies.
In saturated sands, losses due to pore pressure buildup might also occur. These arise due to the phase lag in response of the pore fluid to the stress buildups. At low frequencies, the pore pressure can equilibrate. At high frequencies however, equilibration is inhibited, leading to losses due to the time delayed strain response and a stiffer frame with higher velocities. In this, additional information about pore pressures can be derived by assuming it to be variable and then modelling the velocities correctly.
The comparison of the measured velocity with the low frequency velocity calculated with the Biot theory allows an

estimation of the discrepancies between the velocities at the different frequency ranges, bearing in mind, that a confirmation of the Biot theory with low frequency experiments is stil debated. The present observations show a difference of almost 5% between the velocities in the two frequency ranges, which decreases with pressure. A similar observation is reported by Winkler (1986) in different sandstones. Here, the velocities measured at ultrasonic frequency are about 10 to 15% higher than the low frequency velocity of the Biot theory. This difference decreases with pressure, and seems to be dependent on porosity; a lower porosity rock shows greater deviation from the low frequency velocity than rocks with higher porosities. A comparison between velocities measured at ultrasonic and seismic frequencies must take this effect into account.

As with every attenuation research, it answers some questions and poses many others:
The significance of an additional frequency-dependant bulk modulus and frequency-dependant shear modulus should be studied. Further investigations should deal with the effects of contact softening on the velocity, dispersion and attenuation in dry and saturated sands. This phenomenon, described by Johnson et al (1971), considers only the static case. Its behavior in a dynamic situation should show interesting results.

Further considerations could possibly go to test the pore pressure buildup losses in the high frequency range (above ca. 100 Hz). Seeing these limits, it would be of interest for the seismic frequency also and be important for the inversion of seismic data with a view of gathering information on physical properties. Also, lateral interpolation of correlations between seismic and physical properties in the vicinity of a bore hole would be more reliable.

7. References

Abramowitz, M., Stegun, I. (1972):
Handbook of Mathematical Functions.
Dover Printing, 8th ed., New York

Anderson, D. L., Hart, R. S. (1978): Q of the earth
J. Geophy. Res., vol. 83, B13, pp. 5869-5882

Attewell, P. B., Ramana, Y. V. (1966): Wave attenuation
and internal friction as functions of frequency in
rocks. Geophysics, vol. 31, 6, pp. 1049-1056

Ben-Menahem, A., Singh, S. J. (1981): Seiscmic Waves and
Sources. Springer Verlag, New York

Bentz, A., Martini, H.-J. (1969): Lehrbuch der angewandten
Geologie, Bd. II, Ferdinand Enke Verlag, Stuttgart

Betekhtin, A. (1970): A Course of Mineralogy.
Peace Publishers, Moscow

Biot, M. A. (1973): Nonlinear and semilinear rheology of
porous solids. J. Geophy. Res., vol. 78, pp. 4924-4937

Biot, M. A. (1962): Generalised theory of acoustic
propagation in porous dissipative media.
J. Acoust. Soc. Amer., vol. 34, pp. 1254-1264

Biot, M. A. (1956a): Theory of propagation of elastic waves
in fluid saturated porous solids. I: Low frequency range
J. Acoust. Soc. Amer., vol. 28, pp. 168-178

Biot, M. A. (1956b): Theory of propagation of elastic waves in fluid saturated porous solids.
II: High frequency range
J. Acoust. Soc. Amer., vol. 28, pp. 179-191

Brandt, D. (1984): Durchschallungen verschiedener Quarzsandfraktionen im Ultraschallbereich bei variablen Drucken und Porensättigungen. Diplomarbeit (unpublished), Inst. für Geophysik, Univ. Kiel

Brandt, H. (1955):
A study of the speed of sound in porous granular media.
J. Appl. Mechanics, Trans. ASME, vol. 22, pp. 479-486

Brennan, B. J., Stacey, F. D. (1977): Frequency dependance of elasticity of rocks - test of seismic velocity dispersion. Nature, vol. 286, 21, pp. 220-222

Burkhardt, H., Pfaffenholz, J., Schütt, R. (1986):
Measurements of Q on natural rock samples in different frequency ranges. In: DGMK Project 254, Absorption of Seismic Waves, final Report, pp 203-238

Dain, J. (1962): Q, loaded and unloaded.
In: Encyclopaedic Dictionary of Physics, 5,
J. Thewlis, ed., p. 730, Pergamon, London

Deresiewicz, H. (1958): Stress-strain relations for a simple model of a granular medium.
J. Appl. Mech., Trans. ASME, vol. 25, pp. 402-406

Digby, P. J. (1981): The effective elastic moduli of porous granular rocks. J. Appl. Mech., ASME, vol. 48

Domenico, S. N. (1977): Elastic properties of unconsolidated porous sand reservoirs.
Geophysics, vol. 42, 7, pp. 1339-1368

Duffy, J., Mindlin, R. D. (1957): Stress-strain relations and vibrations of a granular medium. J. Appl. Mech., ASME, vol. 24, pp. 585-593

Engelhard, L., in cooperation with Doan, D., Dohr, G., Drews, P., Groß, Th., Neupert, F., Sattleger, J., Schönfeld, U. (1986): Determination of the attenuation of seismic waves from actual field data, as well as considerations to fundamental questions from model and laboratory measurements. In: DGMK Project 254, Absorption of seismic waves, final report, pp. 83-118

Engelhardt, W. von (1960): Porenraum der Sedimente. Springer Verlag, Berlin

Futterman, W. J. (1962): Dispersive body waves. J. Geophy. Res., vol. 67, pp. 5279-5291

Gassmann, F. (1951): Über die Elastizität poröser Medien. Vierteljahresschrift der Naturforschenden Gesellschaft, Zürich, Bd. 96

Geertsma, J., Smit, D. C. (1961): Some aspects of elastic wave propagation. Geophysics, vol. 26, pp. 169-181

Gladwin, M. T., Stacey, F. D. (1974): Anelastic degradation of acoustic pulses in rocks. Phys. Earth Planet. Int., vol. 8, pp. 332-336

Goodman, L. E., Brown, C. B. (1962): Energy dissipation in contact friction: constant normal and tangential loading. J. App. Mech., ASME, vol. 29, pp. 17-22

Gordon, R. B., Davis, L. A. (1968): Velocity and attenuation of seismic waves in imperfectly elastic rocks. J. Geophy. Res., vol. 73, pp. 3917-3935

Green, D. H., Wang, H. F. (1986): Fluid pressure response to undrained compression in saturated sedimentary rock. Geophysics, vol. 51, 4, pp. 948-956

Hamilton, E. L. (1972): Compressional-wave attenuation in marine sediments. Geophysics, vol. 37, pp. 620-646

Han, De-hua, Nur, A., Morgan, D. (1986): Effects of porosity and clay content on wave velocities in sandstones. Geophysics, vol. 51, 11, pp. 2093-2107

Handbook of Physical Constants (1974): 55th Edition, ed. R. C. Weast, CRC Press, Inc., Ohio

Hosten, B., Deschamps, M. (1984): Étude de la transmission ultrasonore en faisceau borné d'une interface plane á l'aide du spectre angulaire d'ondes planes. Publ. du Lab. Mec. Phys., UA 867, CNRS, Univ. Baurdeaux I. In: Acoustics of porous media, Bourbié, T., Coursy, O., Zinszner, B. (1987), Éditions Technip, Paris

Hovem, H. M., Ingram, G. D. (1979): Viscous attenuation of sound in saturated sand. J. Acoust. Soc. Amer., vol. 66, pp. 1807-1812

Huszak, M. (1986): Durchschallungsmessungen mit Kompressions- und Scherwellen zur Untersuchung der Dämpfungseigenschaften von wasser- und ölgesättigten Sanden. Diplomarbeit (unpublished), Inst. f. Geophysik, Univ. Kiel

Jackson, I. (1986): The laboratory study of seismic wave attenuation. In: Hobbs, B. E., Heard, H. C. (ed.): Mineral and rock deformation; laboratory studies. American Geophysical Union, Geophysical Monographs, vol. 36, pp. 11-23

Jannsen, D., Voss, J., Theilen, F. (1985):
Comparison of methods to determine Q in shallow marine sediments from vertical reflection seismograms.
Geophys. Pros., vol. 23, pp.479-497

Jedicke, F. (1984): Ein Experiment zur Bestimmung der spezifischen Absorption von Sanden im niederfrequenten Bereich. Diplomarbeit (unpublished), Inst. f. Geophysik, Univ. Kiel, p. 151

Johnson, K. L., Kendall, K., Roberts, A. D. (1971):
Surface energy and the contact of elastic solids.
Proc. Roy. Soc. London, vol. A 324, pp. 301-313

Kendall, K. (1969): Ph.D. thesis. In: Johnson et al (1971)

Knopoff, L., McDonald, G. J. F. (1958):
Attenuation of small amplitude stress waves in solids.
Rev. Modern Phys., vol. 30, pp. 1178-1192

Kümpel, H.-J., Lohr, G. (1985): In-situ permeability from non-dilational soil deformation caused by groundwater pumping - a case study.
Journal of Geophysics, vol. 57, pp. 184-190

Liu, Hsi-ping, Anderson, D. L., Kanamari, H. (1976):
Velocity dispersion due to anelasticity implications for seismology and mantle composition.
Geophy. J. of RAS, vol. 47, pp. 41-48

Mavko, G. M. (1979): Frictional attenuation:
An inherent amplitude dependence.
J. Geophy. Res., vol. 84, pp. 4769-4775

McCann, C., McCann, D. M. (1985): A theory of compressional wave attenuation in non cohesive sediments.
Geophysics, vol. 50, 8, pp. 1311-1317

McKavanagh, B., Stacey, F. D. (1974):
Mechanical hysteresis in rocks at low strain amplitudes and seismic freqencies.
Phys. Earth Planet. Int., vol. 8, pp. 228-250

Meißner, R., Theilen, F. (1983): Attenuation of seismic waves in sediments. In: Proceedings of the 11th World Petroleum Congress, 2, John Wiley, London

Mindlin, R. D. (1949): Compliance of elastic bodies in contact. J. Appl. Mech., ASME, vol. 16, pp. 259-268

Mindlin, R. D., Deresiewicz, H. (1953): Elastic spheres in contact under varying oblique forces.
J. Appl. Mech., Trans. ASME, vol. 20, pp. 327-344

Muckelmann, R. (1985): Theoretische und experimentelle Untersuchungen von P- und S-Wellen in Sanden unter besonderer Berücksichtigung ihrer Dämpfungseigenschaften. Dissertation, Univ. Kiel

Murphy, W. F. (1984a): Seismic to ultrasonic velocity drift: Intrinsic absorption and dispersion in crystalline rock. Geophy. Res. Lett., vol. 11, pp. 1239-2142

Murphy, W. F. (1984b): Acoustic measures of partial gas saturation in tight sandstones.
J. Geophy. Res., vol. 89, pp. 11549-11559

Murphy, W. F. (1982): Effects of partial water saturation on attenuation in Massilon sandstone and Vycor porous glass. J. Acoust. Soc. Amer., vol. 71, pp. 1458-1468

Murphy, W. F., Winkler, K. W., Kleinberg, R. L. (1986): Acoustic relaxation in sedimental rocks: Dependance on grain contacts and fluid saturation.
Geophysics, vol. 51, 3, pp. 757-766

Murphy, W. F., Winkler, K. W., Kleinberg, R.L. (1984a): Frame modulus reduction. The effect of adsorption on grain contacts. Geophys. Res. Lett., vol. 11, 9, pp. 805-808

Murphy, W. F., Winkler, K. W., Kleinberg, R. L. (1984b): Centimeter Scale heterogenetics and minastratification in sedimental rocks.
Geophys. Res. Lett., vol. 11, 8, pp. 697-700

Murphy, W. F., Winkler, K. W., Kleinberg, R. L. (1984c): Contact microphysics and viscous relaxation in sandstones. AIP-Proc 107, Physics and Chemistry of Porous Media, Johnson and Sen. (eds)

Nowick, A. S., Berry, B. S. (1972): Anelastic Relaxation in Crystalline Solids, Academic Press, New York

O'Connell, R. J., Budiansky, B. (1978): Measures of attenuation in dissipative media.
Geophy. Res. Lett., vol. 5, pp. 5-8

O'Connell, R. J., Budiansky, B. (1977): Viscoelastic properties of fluid-saturated cracked solids.
J. Geophy. Res., vol. 82, pp. 5719-5735

O'Connell, R. J., Budiansky, B. (1974): Seismic velocities in dry and cracked solids.
J. Geophy. Res., vol. 79, pp. 5412-5426

Pekdeger, A., Schulz, H. D. (1975): Ein Methodenvergleich zur Laborbestimmung des k_f-Wertes von Sanden. Meyniana, vol. 27, pp. 35-40

Peselnick, L., Outerbridge, W. F. (1960): Internal friction in shear and shear modulus of Solenhofen Limestone over a frequency range of 10^7 cycles per second. J. Geophy. Res., vol. 66, pp. 581-588

Prinz, H. (1982): Abriß der Ingenieurgeologie,
Ferdinand Enke Verlag, Stuttgart

Raymer, D. S., Hunt, E. R., Gardner, J. S. (1980):
An improved sonic transit time-to-porosity transform,
presented at Soc. Prof. Well Log Anal.,
21st Annual Meeting, paper P

Roberts, A. D. (1968): Ph.D. thesis. In: Johnson et al (1971)

Seeburger, D. A., Nur, A. (1984): A pore space model for
rock permeability and bulk modulus.
J. Geophy. Res., vol. 89, pp. 527-536

Shumway, G. (1960a): Sound speed and absorption
studies of marine sediments by a resonance method.
Part I. Geophysics, vol. 25, pp. 451-467

Shumway, G. (1960,b): Sound speed and absorption
studies of marine sediments by a resonance method.
Part II. Geophysics, vol. 25, pp. 659-682

Shumway, G. (1956): A resonant chamber method for sound
velocity and attenuation measurements in sand.
Geophysics, vol. 21, pp. 305-319

Sowers, G. F. (1979):
Introductory Soil Mechanics and Foundations.
Collier MacMillan International Edition, London

Spencer, J. W. (1981): Stress relaxations at low frequencies
in fluid saturated rocks: Attenuation and modulus
dispersion. J. Geophy. Res., vol. 86, 3, pp. 1803-1812

Stewart, R. R., Toksöz, M. N., Timur, A. (1983): Strain
dependant attenuation observations and a proposed
mechanism. J. Geophy. Res., vol. 88, pp. 546-554

Stoll, R. D. (1980): Theoretical aspects of sound transmission in sediments.
J. Acoust. Soc. Amer., vol. 68, pp. 1341-1350

Stoll, R. D. (1979): Experimental studies of attenuation in sediments. J. Acoust. Soc. Amer., vol. 66, pp. 1152-1160

Stoll, R. D. (1977): Acoustic waves in ocean sediments.
Geophysics, vol. 42, pp. 715-725

Stoll, R. D. (1974): Acoustic waves in saturated sediments.
in: Physics of Sound in Marine Sediments.
L. Hampton ed., Plenum Pressm, N. Y.

Stoll, R. D., Bryan, G. M. (1970):
Wave attenuation in saturated sediments.
J. Acoust. Soc. Amer., vol. 47, pp. 1440-1447

Tarif, P. (1986): Mesure de'latténuation par propagation d'ultrasons: application á l'étude de l'anisotropie, thesis, université Paris VII. In: Acoustics of porous media, Bourbié, T., Coursy, O., Zinszner, B. (1987), éditions Technip, Paris

Tittmann, B. R. (1978): Internal friction measurements and their implications in seismic Q structure modells of the earth's crust. In: The Earth's Crust, AGU Monograph, Ser. 20, J. Heacock (ed.), pp. 197-213

Toksöz, M. N., Johnston, D. H., Timur, A. (1979): Attenuation of seismic waves in dry and saturated rocks: Laboratory measurements. Geophysics, vol. 44, pp. 681-690

Tonn, R. (1987): Comparison of seven methods for the computation of Q. Proc. IUGG Assembly, Vancouver

Unsöld, G. (1983): Der Transportbeginn rolligen Sohlmaterials in gleichförmigen turbulenten Strömungen: eine kritische Überprüfung der Shields-Funktion und ihre experimentelle Erweiterung auf feinstkörnige nichtbindige Sedimente. Diss., Math.-Naturwiss. Fak., Kiel

Walton, K. (1977): Elastic wave propagation in model sediments. Geophy. J. RAS, vol. 48, pp. 461-478

Winkler, K. W. (1986): Estimates of velocity dispersion between seismic and ultrasonic frequencies. Geophysics, vol. 51, 1, pp. 183-189

Winkler, K. W. (1985): Dispersion analysis of velocity and attenuation in Berea sandstone. J. Geophy. Res., vol. 90, B8, pp. 6793-6800

Winkler, K. W. (1983): Contact stiffness in granular porous materials. Comparison between theory and experiments. Geophy. Res. Lett., vol. 10, pp. 1073-1076

Winkler, K. W. (1983): Frequency dependent ultrasonic properties of high-porosity sandstones. J. Geophy. Res., vol. 88, pp. 9493-9499

Winkler, K. W., Nur, A. (1982): Seismic attenuation: effects of pore fluid and frictional sliding. Geophysics, vol. 47, pp. 1-15

Winkler, K. W., Nur, A. (1979): Pore fluids and seismic attenuation in rocks. Geophy. Res. Lett., vol. 6, pp. 1-4

Winkler, K. W., Plona, T. J. (1983): Technique for measuring ultrasonic velocity and attenuation spectra in rocks under pressure. J. Geophy. Res., vol. 87, pp. 10776-10780

Winkler, K. W., Nur, A., Gladwin, M. (1979):
Friction and seismic attenuation in rocks.
Nature, vol. 277, pp. 528-531

Wood, A. B. (1930): A Textbook of Sound.
In: J. Schön (1983): Petrophysik,
Ferdinand Enke Verlag, Stuttgart

Wyllie, M. R. J., Gregory, A. R., Gardner, L. W. (1956):
Elastic wave velocities in heterogeneous and porous
media. Geophysics, vol. 21, 1, pp. 41-70

Zschau, J. (1985): Q^{-1}, was ist das?
Internal paper, Inst. f. Geophysik, unpublished

Acknowledgements

This work is completed under the supervision of Prof. Dr. R. Meißner. My profound thanks to him for the guidance, the freedom to develop ideas and the discussions to keep the ideas realistic.
For very fruitful discussions and the help to see beyond small barriers, I am indebted to Prof. Dr. J. Zschau.
My sincere thanks are due to Dr. F. Theilen for supervision and stimulating interest taken in this work.
For the introduction to 'Q' with all its pitfalls and for a critical reading of the manuscript, I am much obliged to Dr. R. Muckelmann and to Mr. M. Huszak for an introduction to the apparatus.
My acknowledgements also go to Mr. R. Becker and Mr. G. Dombrowski for transforming confuse ideas into solid frames.
Of course this thesis would not be readable, were it not for the expertise of Ms. G. Reim, Ms. R. Bittner and Mr. G. Fuchs.